UNIVERSITY OF OTTAWA

MASTER OF SCIENCE THESIS

Metasurface Platforms for Linear and Nonlinear Optical Applications

Author:
Mohammadreza MOHAMMADPOUR

Supervisor:
Prof. Ksenia DOLGALEVA

A thesis submitted in partial fulfillment of the requirements for the Master of Science in Physics

Department of Physics
Faculty of Science
University of Ottawa

© Mohammadreza Mohammadpour, Ottawa, Canada, 2026

Declaration of Authorship

I, Mohammadreza MOHAMMADPOUR, declare that this thesis, titled "Metasurface Platforms for Linear and Nonlinear Optical Applications", and the work presented in it are my own. I confirm that except where specific reference is made to the work of others, the contents of this dissertation are original and have not been submitted in whole or in part for consideration for any other degree or qualification in this, or any other university. This dissertation is my own work and contains nothing which is the outcome of work done in collaboration with others, except as specified in the text and Acknowledgements.

Mohammadreza Mohammadpour
November, 2026
Ottawa, Canada

UNIVERSITY OF OTTAWA

Abstract

Department of Physics
Faculty of Science

Master of Science

Metasurface Platforms for Linear and Nonlinear Optical Applications

Mohammadreza MOHAMMADPOUR

The ability to manipulate light at deeply subwavelength scales is central to the development of the next generation of photonic technologies. Optical metasurfaces provide a versatile means of achieving such control through engineered light–matter interactions. In this thesis, we investigate the modeling, design, and experimental characterization of metamaterials and metasurfaces for applications including spectral filtering, microscopy, and wavelength conversion. The physical mechanisms governing the interaction of light with individual particles and their collective arrangements are examined through an analytical treatment of electromagnetic scattering by a dielectric sphere and an investigation of the interactions between subwavelength elements. These insights are then applied to realize optical functionalities that are difficult to achieve with conventional devices by using thin arrays of engineered particles.

The investigated platforms include highly transmissive terahertz band-pass filters with sharp spectral edges and geometrically tunable spectral responses, as well as nonlinear optical microscopy platforms for resolving subwavelength features. The relationship between nanoantenna geometry, symmetry, and second-order hyperpolarizability is also investigated, demonstrating how second-harmonic-generation spectroscopy can provide information about the orientation and geometrical properties of nanoscale structures. In

addition, resonant metasurface platforms supporting localized and collective modes, including localized surface-plasmon resonances and surface-lattice resonances, are designed to enhance and control nonlinear optical emission.

Overall, this thesis demonstrates the potential of engineered metasurfaces as compact and efficient platforms for controlling linear and nonlinear optical processes across the terahertz, infrared, and visible spectral ranges, with potential applications in medicine, astronomy, and sensing.

Acknowledgement

I am grateful to everyone who supported me throughout my master's studies and helped shape this thesis. First of all, I would like to express my sincere gratitude to my supervisor, Prof. Ksenia Dolgaleva, for giving me the opportunity to pursue my master's degree under her guidance and supervision. I am deeply thankful for her invaluable technical discussions, constant encouragement, and collaborative spirit. The funding opportunities she identified and supported were indispensable in advancing my research and played a crucial role in making this work possible.

I also extend my sincere thanks to our former PhD student, Dr. Sina Aghili, for his generous support and guidance across several projects, particularly in metasurface modelling and design. I am also deeply grateful to Dr. Lais Fujii dos Santos and Dr. Athulya Thulaseedharan for their valuable work in fabricating the metasurfaces.

I would also like to thank Prof. André Staudte and his team at the National Research Council Canada for their technical support and guidance in building and aligning the nonlinear experimental setup. I am also grateful to Prof. Lora Ramunno for her support and advice on the theoretical modelling of metasurfaces and for the insightful discussions throughout our collaboration.

Finally, my heartfelt thanks go to my mother and the rest of my family—my grandmother, uncles, aunts, and cousins—for their warmth, encouragement, and endless support, which meant more to me than words can express.

Contents

Declaration of Authorship ii

Abstract iii

Acknowledgement v

List of Abbreviations xviii

1 Introduction 1
- 1.1 Background . . . 1
- 1.2 Metasurfaces . . . 7
- 1.3 Meta-atom . . . 8
  - 1.3.1 Plasmonic meta-atom . . . 11
  - 1.3.2 Dielectric meta-atom . . . 13
  - 1.3.3 III–V semiconductors . . . 16
- 1.4 Theoretical Description of Light Scattering by Nanoantennas . 18
- 1.5 Collective effects in metasurfaces . . . 20
- 1.6 Nonlinear Optics . . . 22
  - 1.6.1 Second-Harmonic Generation . . . 22
  - 1.6.2 Sum- and Difference-Frequency Generation . . . 24
  - 1.6.3 Third-Order Nonlinear Processes . . . 26
  - 1.6.4 Cascaded Nonlinearities . . . 27
- 1.7 Nonlinear Metasurfaces . . . 28
- 1.8 THz and infrared meta-filters . . . 31
- 1.9 Thesis Structure . . . 33

2 Theoretical Foundations of Metasurfaces and metamaterials 35

2.1 Mie theory . . . 36
2.1.1 Super-radiating and non-radiating states . . . 42
2.2 Multipole decomposition . . . 43
2.3 Coupled Meta-atoms . . . 46
2.3.1 Coupled dipole approximation . . . 46
2.3.2 Surface lattice resonance . . . 47
2.3.3 Fano resonance . . . 50
2.4 Nonlinear Multipoles . . . 52
2.5 Nonlinear metasurfaces . . . 54
2.5.1 Hydrodynamic Model . . . 57
2.5.2 Nonlinear Scattering Theory . . . 59
2.6 THz and infrared meta-filters . . . 62
2.6.1 Babinet's Principle . . . 62
2.6.2 multilayer complementary metasurfaces . . . 63
2.7 Computational Methods . . . 69
2.8 Conclusion . . . 71

3 THz spectral meta-filter 72
3.1 Introduction . . . 72
3.2 Methodology . . . 73
3.2.1 Computational methods . . . 75
3.3 Results . . . 78
3.4 Conclusion . . . 89

4 Orientation-Resolved SHG Imaging: The Role of Near-Field Interactions 90
4.1 Introduction . . . 91
4.2 Methodology . . . 92
4.3 Design . . . 94
4.4 Fabrication . . . 103
4.5 Experimental Setup . . . 104
4.5.1 Linear Measurement Setup . . . 104
4.5.2 Nonlinear Microscopy Setup . . . 105
4.5.3 Experimental conditions . . . 106
4.5.4 Experimental repeatability and sample variation . . . 106
4.5.5 Data processing . . . 107

4.6 Results 108
4.7 Conclusions 117

5 Bi-Layered Stack Plasmonic Metasurface for High-Resolution Near-Field SHG Microscopy Applications **119**
5.1 Introduction 119
5.2 Methodology 122
5.3 Design and Results 122
5.3.1 Lateral misalignment between the layers 133
5.3.2 Second-harmonic current density in the V-shaped nanoantenna 133
5.4 Conclusion 134

6 Probing Geometry-Dependent Hyperpolarizability of Plasmonic Nanoparticles via SHG Spectroscopy **135**
6.1 Methodology 137
6.1.1 Hyperpolarizability Calculation 137
6.1.2 Computational Methods 139
6.2 Design and results 140
6.3 Experimental setup 145
6.4 Conclusion 146

7 Conclusion **148**

Bibliography **153**

List of Figures

1.1 (a) Schematic and (b) SEM image of a three-dimensional metamaterial composed of alternating Ag and MgF_2 layers. From Ref. [41]. 7
1.2 Schematic of a metasurface composed of a periodic array of L-shaped gold nanoantennas on a silica substrate. From Ref. [42]. 8
1.3 SEM images of common meta-atom geometries, including nanodisks, nanorods, V-shaped antennas, split-ring resonators, and fishnet structures. From Ref. [44]. 9
1.4 (a) Real and (b) imaginary parts of gold permittivity. (c) The real and (d) imaginary parts of polarizability for gold nanoparticles with three different radii. (e) The SCS and (f) the ACS of gold nanoparticles [48]. 12
1.5 Manifestations of all-dielectric nanophotonics: (a) magnetic-dipole field distribution, (b) experimental optical magnetic response, (c) unidirectional scattering from a dielectric nanoparticle, and (d) light manipulation using a highly transparent Huygens metasurface. From Ref. [50]. 16
1.6 (a) Energy-level representation of second-harmonic generation (SHG). From Ref. [70]. 24
1.7 (a) Energy-level diagram illustrating a sum-frequency generation (SFG) and (b) difference-frequency generation (DFG). From Ref. [70]. 25
1.8 Two possible mixing processes can occur when three input waves interact in a medium characterized by a $\chi^{(3)}$ susceptibility. From Ref. [70] 27

2.1 Source-free scattered field normalized to the incident amplitude for different l values and polarizations. From Ref. [101]. . 42
2.2 Normalized scattering cross section and the respective contributions of the TM and TE fields for $l = 1, 2$ in panels (a)–(f), for silver particles with radii of 300 nm and 25 nm embedded in SiO_2. From Ref. [101]. 43
2.3 Total scattering efficiency (blue line, logarithmic scale) versus permittivity (lossless) for size parameter $x = 0.75$ ($x = k_0 r = 2\pi r/\lambda$). The dashed and dash-dot lines show the absolute values of the first three electric (a_1, a_2, a_3) and magnetic (b_1, b_2, b_3) multipole coefficients, respectively. The insets display the corresponding surface charge (electric multipoles) and surface current (magnetic multipoles) distributions. From Ref. [102]. . . . 45
2.4 (a) Calculated transmission spectrum of a single gold sphere with a radius of 80 nm in an air environment. (b) Transmission response of a one-dimensional periodic chain formed by 1000 identical gold spheres, where the particles are separated by a period of 620 nm. From Ref. [73]. 48
2.5 Extinction spectra obtained from simulations for silver nanoparticles with a diameter of 100 nm arranged in (a) a linear chain of 400 particles and (b) a hexagonally packed two-dimensional array containing 400 particles. The effect of varying the interparticle spacing is examined by presenting spectra for several array periods. In the 1D configuration, the incident polarization and propagation direction are both transverse to the chain axis. In the 2D array, illumination occurs normal to the array surface, with the electric field polarized parallel to the nanoparticle plane. From Ref. [79]. 49
2.6 Schematic representation of two coupled damped oscillators, with a driving force f_1 applied to the first oscillator. From Ref. [104]. 50
2.7 Fano parameter versus phase shift and the Fano response function. From Ref. [104]. 52
2.8 Lorentz–reciprocity theory application for SHG from a resonant plasmonic meta-atom. 60

2.9 Complementary structures illustrating Babinet's principle. . . 63
2.10 (a) 3D schematic of the simulated structure. (b) Transmittance (black) and reflectance (red) spectra shown on the left axis, and the absorptance spectrum shown on the right axis, for the metafilter with optimized geometrical parameters: $p_x = p_y = 77\ \mu$m, $h = 25\ \mu$m, $r = 30\ \mu$m, and $dr = 10\ \mu$m. From Ref. [99]. 65
2.11 (a) Relative impedance of the structure compared with the transmission spectrum. (b) Configurations of the original and the effective structure, in which the Si–air ring layer is replaced by a homogeneous dielectric slab. (c) Transmission spectra obtained from the numerical simulation and calculated using Eq. (2.4). (d) Magnitudes and phases of the reflection coefficients at the interfaces between the first and second regions and between the second and third regions. From Ref. [99]. . . 67
2.12 (a) Unit-cell configuration of the proposed filter. (b) Transmittance spectra of the corresponding structure for different cylinder radii, with the optimized geometrical parameters $w_1 = w_2 = 2.4R_p$, $h_1 = 10\ \mu$m, $h_2 = 0.2\ \mu$m, $h_3 = 8\ \mu$m, and $h_4 = 0.2\ \mu$m. From Ref. [97]. 68
2.13 (a) Unit-cell configuration of the proposed filter. (b) Transmittance spectra of the corresponding structure for different cylinder radii, with the optimized geometrical parameters $w_1 = w_2 = 4.8R_p$, $h_1 = 10\ \mu$m, $h_2 = 0.2\ \mu$m, $h_3 = 8\ \mu$m, and $h_4 = 0.2\ \mu$m. 69

3.1 Three-dimensional schematic of the proposed meta-filter, showing its constituent layers and main geometrical parameters: cross-arm length L, width w, resonator thickness h, and array periodicity p. 73
3.2 Three-dimensional CAD view of the simulated metafilter configuration, showing the layer arrangement and the positions of the incident source and transmission monitor. 78

3.3 (a)-(c) Transmission spectra and corresponding unit-cell configurations of metasurfaces consisting of (a) a Si bar oriented along the y-direction, (b) a Si bar oriented along the x-direction, and (c) a Si cross. In all three configurations, the resonators are placed on a Si substrate and have a thickness of 4.6 μm. 80
3.4 (a)-(c) Transmission spectra and corresponding unit-cell configurations of metasurfaces consisting of (a) a Si bar oriented along the x-direction, (b) a Si bar oriented along the y-direction, and (c) a Si cross. In all three configurations, the Si resonators are placed on a Si substrate, have a thickness of 4.6 μm, and are covered with a 200 nm-thick Au layer. 82
3.5 (a)-(c) Transmission spectra and corresponding unit-cell configurations of metasurfaces consisting of a Si substrate, a 200 nm-thick Au layer patterned with complementary apertures, and 4.6 μm-thick Si resonators positioned within the apertures and directly on the substrate. The Si resonators consist of (a) a bar oriented along the x-direction, (b) a bar oriented along the y-direction, and (c) a cross. 84
3.6 Transmission spectra of the configuration shown in Figure 3.1 for different cross lengths. The incident wave is x-polarized and propagates along the -z direction, illuminating the structure from the top. The fixed geometrical parameters are $p_x = p_y = 10.5$ μm and $w = 3$ μm, with $h = 4.6$ μm. 86
3.7 Transmission spectra as a function of wavelength for filters designed around central wavelengths of (a) 80 μm and (b) 30 μm. The incident wave is x-polarized, propagates along the $-z$ direction, and illuminates the structure from the top. The optimized geometrical parameters are (a) $p_x = p_y = 16.8$ μm, $l = 13.2$ μm, $h = 7$ μm, and $w = 4.5$ μm; and (b) $p_x = p_y = 7.1$ μm, $l = 5.1$ μm, $h = 3$ μm, and $w = 2$ μm. 87
3.8 Transmission spectra of the optimized structure for different incident polarization angles. 88

4.1 (a) Unit cell geometry of the metasurface design composed of a single asymmetric V-shaped nanoparticle. (b) Overall metasurface configuration. The Au nanoparticle is 25 nm thick, with a 3 nm-thick chromium adhesion layer between the Au and the silica substrate. 95
4.2 (a) Simulated transmission spectra of the metasurface and corresponding hotspot images (at a wavelength of 1100 nm), for a unit cell containing a V-shaped particle under x-, y-, and 45° polarizations. (b) Corresponding results for an L-shaped particle. (c) Corresponding results for a particle with a $-60°$ orientation. 96
4.3 Simulated nonlinear transmitted power per unit cell of the metasurface with a unit cell consisting of a V-shaped particle (2 μm periodicity) as a function of pump wavelength. under x-, y-, and 45°-polarized excitation. 97
4.4 Simulated nonlinear conversion efficiency of the metasurface with a unit cell consisting of a V-shaped particle (2 μm periodicity) as a function of pump wavelength under x-, y-, and 45°-polarized excitation. 98
4.5 Simulated geometry and field distributions. (a) Geometry and particle arrangement within the unit cell. (b) and (d) Normalized linear near-field intensity distributions evaluated 50 nm above the particle surface at the pump wavelength (1100 nm) under x- and y-polarized illumination, respectively. (c) and (e) Corresponding nonlinear near-field intensity distributions at the second-harmonic wavelength (550 nm) under x- and y-polarized excitation, respectively. 99

4.6 Simulated geometries and near-field distributions. (a), (d), and (g) show the geometries and particle arrangements within the unit cell. (b), (e), and (h) show the normalized linear near-field intensity distributions, evaluated 50 nm above the particle surface at the pump wavelength (1100 nm), for the unit cells with the middle particle oriented at -60°, L-shaped, and V-shaped, respectively, under y-polarized illumination. (c), (f), and (i) show the corresponding nonlinear near-field intensity distributions for the same unit cells. 101
4.7 SEM images of fabricated L-shaped gold nanoparticles with different orientations. 104
4.8 (a) Schematic of the linear experimental setup used to measure the transmission spectrum. (b) Focused light on the fabricated sample at the fundamental wavelength. 104
4.9 The imaging setup for the SHG microscopy. 105
4.10 (a) Simulated transmission spectra under x- and y-polarized excitation for the sample with a middle particle oriented at $-60°$. (b) Corresponding simulated far-field transmitted second-harmonic (SHG) power for both polarizations. (c) Corresponding simulated nonlinear conversion efficiency for both polarizations. 109
4.11 (a) and (b) Experimental transmission spectra for x- and y-polarized excitations, respectively. (c) and (d) near-field SHG image acquired experimentally at 515 nm wavelength under x- and y-polarized excitation, respectively. 110
4.12 (a) Geometry of the simulated structure. (b) and (d) show the corresponding simulated linear intensity distributions at a height of 50 nm above the surface for x- and y-polarized excitation, respectively. (c) and (e) show the corresponding simulated nonlinear intensity distributions for x- and y-polarized excitation, respectively. 113

4.13 (a) Geometry of the simulated structure. (b) and (d) show the corresponding simulated linear intensity distributions at a height of 50 nm above the surface for x- and y-polarized excitation, respectively. (c) and (e) show the corresponding simulated nonlinear intensity distributions for x- and y-polarized excitation, respectively. 114
4.14 (a) and (b) show the fabricated sample with a spacing of 1 μm. (c) and (d) show the corresponding experimentally measured SHG images at the wavelength of 515 nm under x- and y-polarized excitation, respectively. 116

5.1 Particle configuration with dimensions $l_1 = 125$ nm, $l_2 = 115$ nm, $h = 30$ nm, and $w = 60$ nm, with an opening angle of 75°, together with the corresponding SCS and near-field profiles at the resonant wavelengths under (a) x- and (b) y-polarized illumination. 124
5.2 (a) Metasurface configuration. (b) Transmission spectrum together with the corresponding near-field distribution at the pump wavelength. (c) Forward-emitted nonlinear intensity together with the corresponding near-field distribution at the SHG wavelength. 126
5.3 (a) Metasurface configuration. (b) Transmission spectrum together with the corresponding near-field distribution at the pump wavelength of 1050 nm. (c) Forward-emitted nonlinear intensity together with the corresponding near-field distribution at the SHG wavelength of 525 nm. 128
5.4 (a) Metasurface and unit-cell configurations, with nanobar dimensions of $l = 150$ nm, $h_1 = 30$ nm, and $w_1 = 60$ nm. (b) Corresponding scattering cross section (SCS) and near-field distribution at the resonant wavelength under x-polarized illumination. (c) Transmission spectrum and corresponding near-field distributions in the x-y and x-z planes at the pump wavelength of 1050 nm. 130

5.5 (a) Metasurface configuration. (b) Transmission spectra for $d = 200$ nm and 300 nm, together with the near-field distribution at the pump wavelength of 1100 nm for $d = 200$ nm. (c) Forward-emitted SHG intensity for $d = 200$ nm and 300 nm, together with the corresponding nonlinear near-field distribution at the SHG wavelength of 525 nm for $d = 200$ nm. 132
5.6 Different components of the current-density distribution across the V-shaped nanoantenna. 133

6.1 (a)–(d) Particle geometries, simulated scattering cross-section (SCS) spectra decomposed into different multipolar contributions, and normalized near-field intensity distributions. The L-shaped particle in (a) is shown under y-polarized excitation, while the T-, cross-, and gammadion-shaped particles in (b)-(d) are shown under x-polarized excitation. The L-, T-, and cross-shaped particles in (a)-(c) have dimensions $l_1 = 150$ nm and $l_2 = 180$ nm. The gammadion-shaped particle in (d) has dimensions $l_1 = 180$ nm, $l_2 = 210$ nm, and $l_3 = 150$ nm. The height h and width w are fixed for all geometries at 25 nm and 80 nm, respectively. The same colour scale is used for all particles. 141
6.2 (a)-(d) Simulated transmission spectra and the corresponding normalized linear near-field intensity distributions 50 nm above the surface at a wavelength of 800 nm for the L-shaped, T-shaped, cross-shaped, and gammadion-shaped particles, respectively. The same colour scale is used for all particles. . . . 142
6.3 (a)-(d) Simulated nonlinear conversion efficiency spectra and the corresponding normalized nonlinear near-field intensity distributions 50 nm above the surface at a wavelength of 400 nm for the L-shaped, T-shaped, cross-shaped, and gammadion-shaped particles, respectively. The same colour scale is used for all particles. 143
6.4 Simulated hyperpolarizability spectra as a function of wavelength for the L-shaped, T-shaped, cross-shaped, and gammadion-shaped particles. 144

6.5 Nonlinear optical setup for measuring the photon count at the SHG wavelength. 146

List of Abbreviations

LSPRs	Localized Surface Plasmon Resonances
SLR	Surface Lattice Resonance
SCS	Scattering Cross Section
ACS	Absorption Cross Section
ED	Electric Dipole
MD	Magnetic Dipole
EQ	Electric Quadrupole
MQ	Magnetic Quadrupole
EO	Electric Octupole
MO	Magnetic Octupole
CMOS	Complementary Metal-Oxide-Semiconductor
FWM	Four-Wave Mixing
SHG	Second Harmonic Generation
SFG	Sum-Frequency Generation
DFG	Difference-Frequency Generation
NLST	Nonlinear Scattering Theory
CDA	Coupled Dipole Approximation

Dedicated to the memory of my beloved grandfather.

Chapter 1

Introduction

1.1 Background

The ever-increasing demand for faster information transfer and processing continues to drive the development of advanced photonic technologies. Overcoming the limitations of electronic data handling, improving data storage, and enabling parallel information processing in compact platforms all rely on the efficient manipulation of optical signals.

Optical devices control light by modifying its phase, amplitude, and polarization. In conventional optics, this control is achieved through mechanisms such as refraction, reflection, and diffraction. Refractive elements, including lenses and waveplates, modify light as it propagates through materials with designed refractive indices, resulting in cumulative phase and polarization changes along the optical path. Diffractive elements, on the other hand, rely on the generation of secondary waves that propagate in free space and interfere in the far field, forming complex optical patterns. As a result, a substantial modification of an optical field typically requires propagation over distances much larger than the wavelength, imposing inherent limitations on the compactness and flexibility of conventional optical components [1], [2].

In addition to their relatively large dimensions, the capabilities of conventional optical devices are subject to fundamental physical constraints, such

as diffraction limit. These limitations make it difficult to achieve highly flexible and precise control of electromagnetic waves for applications such as subwavelength-resolution imaging, beam steering, and holography. The emergence of metamaterials provided a new approach to overcoming some of these restrictions [3].

Metamaterials are artificially structured media composed of periodically or non-periodically arranged subwavelength elements. Their electromagnetic responses are determined not only by the properties of their constituent materials but also by the geometry and arrangement of their unit cells. Therefore, metamaterials can exhibit electromagnetic properties that are not readily available in naturally occurring materials [4], [5].

The theoretical origin of metamaterials can be traced to the work of Victor G. Veselago in 1968. Veselago studied a hypothetical left-handed medium characterized by simultaneously negative electric permittivity and magnetic permeability [6]. In such a medium, the wave vector **k** and the electric- and magnetic-field vectors, **E** and **H**, form a left-handed coordinate system. This arrangement results in unconventional electromagnetic behaviour, including a negative refractive index. However, because no naturally occurring material was known to possess negative permittivity and permeability simultaneously, the practical realization of such a medium remained unresolved for almost three decades.

In the late 1990s, Sir John B. Pendry and his colleagues proposed methods for realizing these electromagnetic properties based on effective-medium theory. They showed that periodically arranged metallic wires at the subwavelength scale could produce an effective negative permittivity [7]. They also demonstrated that arrays of metallic split-ring resonators could generate an effective negative magnetic permeability [8]. These structures provided the necessary components for realizing the left-handed medium previously proposed by Veselago and established an important foundation for the theoretical and experimental investigation of metamaterials.

In 2000, Smith and co-workers experimentally demonstrated a microwave

left-handed medium composed of metallic-wire arrays and split-ring resonators. This study confirmed that an artificial structure could simultaneously exhibit negative effective permittivity and permeability and opened the way for extensive metamaterial research [9]. Based on the effective-medium model, metamaterials with controllable parameters were subsequently developed. These included structures exhibiting negative or near-zero refractive indices, extremely high permittivity, and non-unity magnetic permeability at high frequencies[10], [11]. Such electromagnetic responses were investigated over a broad spectral range extending from microwave to optical frequencies [4].

The ability to engineer metamaterials enabled several unconventional applications, including invisibility cloaks, flat lenses, and super-resolution imaging devices [3], [4]. Various electromagnetic devices, such as absorbers, spectral filters, and polarization converters, were also widely investigated [12]. These structures therefore provided substantial freedom for manipulating electromagnetic waves. Nevertheless, their responses were generally defined by fixed geometrical parameters, making real-time control difficult [13].

In parallel with the development of effective-medium metamaterials, plasmonic metamaterials attracted considerable attention because of their ability to control surface electromagnetic waves. At optical wavelengths, surface plasmons supported at metal–dielectric interfaces provide strong electromagnetic-field confinement and enhancement [14]. These properties have been extensively used for super-resolution imaging, ultrasensitive detection, and the development of miniaturized photonic devices [14], [15]. However, this behaviour cannot be extended directly to microwave and terahertz frequencies because noble metals behave as good conductors at these lower frequencies.

To overcome this limitation, Pendry and co-workers introduced the concept of designer, or spoof, surface plasmons in 2004 using structured metallic surfaces [16]. These structures imitate the behaviour of optical surface plasmon polaritons and reproduce their field-enhancement properties at lower frequencies. They therefore enable the subwavelength manipulation of surface

waves within frequency ranges in which natural optical surface plasmons cannot be directly supported [17].

Although three-dimensional metamaterials offer considerable control over electromagnetic waves, their practical implementation can require complicated volumetric structures. The difficulty of fabricating three-dimensional structures becomes particularly significant as the operating wavelength decreases and the required unit-cell dimensions reach the micro- and nanoscale. Metasurfaces emerged as the two-dimensional counterparts of metamaterials, providing a planar approach to electromagnetic-wave manipulation [18].

A major milestone in the development of metasurfaces was achieved in 2011, when Capasso's group introduced an approach for shaping electromagnetic beams through abrupt phase discontinuities. Arrays of optical antennas with deeply subwavelength thickness were designed to impose spatially varying phase changes, enabling anomalous reflection and refraction. This work demonstrated that optical wavefronts could be controlled at an interface without requiring propagation through a thick optical medium [19]. Following this development, metasurfaces were widely investigated for functions such as anomalous reflection and refraction, polarization conversion, vortex-beam generation, and holographic imaging [20].

These planar platforms, composed of arrays of engineered scatterers or optically thin films, provide compact and highly integrated optical functionalities at the nanoscale. The dimensions, geometry, orientation, and arrangement of their constituent elements can be designed to control the phase, amplitude, and polarization of the scattered light [1]. Consequently, metasurfaces have enabled numerous applications, including phase front shaping, spectral filtering, sensing, and imaging [20].

Further progress was made in 2014, when Engheta's group and Tie Jun Cui's group independently introduced the concept of digital metamaterials. Unlike conventional metamaterials, the digital and coding metamaterials developed by Cui and co-workers were represented using binary coding states.

Cui and colleagues also proposed field-programmable metamaterials in which switchable digital coding states enabled the real-time manipulation of electromagnetic waves[21], [22].

Beyond their linear functionalities, metasurfaces provide a versatile platform for extending light manipulation into the nonlinear regime by enhancing nonlinear optical processes that are typically weak in bulk materials. Their subwavelength elements can strongly confine the incident electromagnetic field and increase its local intensity, thereby improving the efficiency of light–matter interactions. These capabilities have enabled applications including all-optical switching, harmonic generation, and ultrashort-pulse lasers [23].

Early nonlinear metasurfaces were predominantly based on plasmonic nanostructures because localized surface-plasmon resonances provide strong field confinement at metal surfaces. In 2003, Anceau et al. demonstrated enhanced SHG from gold nanostructures [24], followed by the observation of SHG from subwavelength metallic-aperture arrays by Airola et al. in 2005 [25]. In 2012, Linden and co-workers showed that collective coupling between split-ring resonators could strongly modify their SHG response [26]. In 2013, Salomon and collaborators investigated size- and shape-dependent SHG resonances in silver nanocavities [27], while Zhang et al. demonstrated enhanced four-wave mixing through coherent Fano resonances in plasmonic nanoclusters [28].

Further progress extended nonlinear metasurfaces from field-enhancement platforms to devices capable of controlling the generated light. In 2014, Luo et al. demonstrated broadband terahertz generation from an ultrathin array of split-ring resonators [29], while In 2015, Celebrano and co-workers demonstrated enhanced SHG in multiresonant plasmonic nanoantennas [30]. In 2016, Almeida et al. demonstrated subwavelength nonlinear phase control in plasmonic metasurfaces, enabling the shaping of the generated field's wavefront [31]. Kauranen's group and other researchers also demonstrated that structural chirality and broken symmetry can produce strong nonlinear

chiroptical responses [32], [33]. Meanwhile, the losses and heating associated with metals motivated the transition toward all-dielectric platforms. In 2014, Shcherbakov and co-workers demonstrated enhanced THG from silicon nanodisks excited near a magnetic Mie resonance [34]. Subsequent studies demonstrated nonlinear interference, ultrafast switching, and enhanced harmonic generation in dielectric nanostructures [35]. In 2018, Wang et al. demonstrated nonlinear wavefront control, including THG beam steering and the generation of nonlinear vortex beams [36], while Liu and co-workers used a GaAs metasurface to generate eleven new frequencies through wave-mixing processes [37]. More recently, Koshelev et al., Carletti et al., and other researchers have employed high-Q collective modes and quasi-bound states in the continuum to enhance nonlinear interactions and control harmonic emission [38]. Cotrufo et al. further introduced nonlinear nonlocal metasurfaces that combine high-Q delocalized resonances with local phase control for directional THG [39]. Together, these advances have established nonlinear metasurfaces as compact platforms for simultaneously enhancing frequency conversion and controlling the amplitude, phase, polarization, and propagation direction of the generated light.

The historical developments reviewed above provide the foundation for the work presented in this thesis. The evolution from three-dimensional metamaterials to planar metasurfaces has enabled compact control of electromagnetic waves, while advances in resonant and nonlinear nanostructures have extended this control to field enhancement and frequency conversion. Building on these developments, this thesis investigates how material composition, particle geometry, symmetry, resonant behavior, and interactions between subwavelength elements form the linear and nonlinear optical responses of metasurfaces. These concepts are examined in the context of a broad range of applications, including spectral filtering, sensing, imaging, and nonlinear frequency conversion. The following sections introduce the principal classes of nanoantennas and the physical mechanisms required for understanding the metasurface platforms investigated in this thesis.

1.2 Metasurfaces

Photonic metamaterials consist of artificially engineered metallic and dielectric subwavelength structures embedded within a host material. When an electromagnetic wave interacts with such a composite system, electric and magnetic dipole moments are induced in the inclusions, which determine the effective permittivity and permeability of the medium. By controlling the size, shape, density, and orientation of these elements, materials with tailored electromagnetic responses can be realized [40]. In particular, resonant electric and magnetic responses can produce a negative effective refractive index and a reversed phase evolution within the material [10]. These capabilities enable optical properties not readily found in natural materials, including magnetism at optical frequencies, impedance matching for reduced reflection, and enhanced nonlinear optical responses, leading to a wide range of applications such as high-resolution imaging, compact polarization control devices, and cloaking technologies [40]. An example of a three-dimensional metamaterial is shown in Figure 1.1, consisting of periodically patterned alternating Ag and MgF_2 layers [41]. However, conventional metamaterials typically require three-dimensional architectures, which can complicate fabrication and limit their integration into compact optical systems.

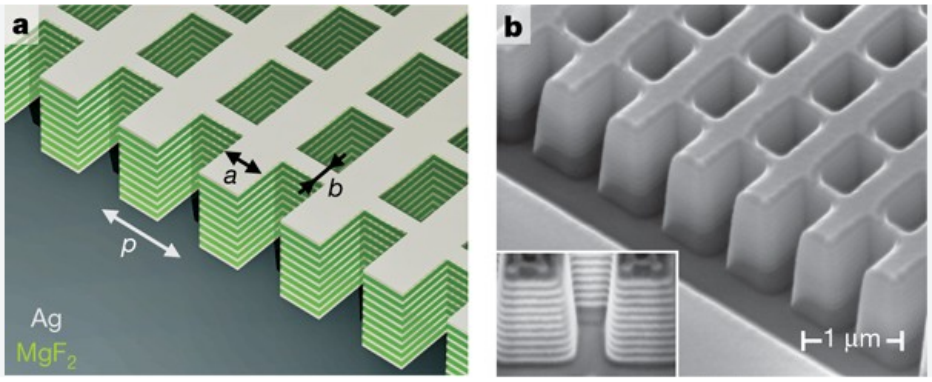

FIGURE 1.1: (a) Schematic and (b) SEM image of a three-dimensional metamaterial composed of alternating Ag and MgF_2 layers. From Ref. [41].

Metasurfaces are the two-dimensional counterparts of metamaterials, designed to control light at an interface rather than through bulk propagation [1], [18]. Similar to metamaterials, their optical response can be described in terms of induced multipole moments in the constituent nanoantennas (meta-atoms). Figure 1.2 illustrates a metasurface formed by a periodic array of L-shaped gold nanoantennas on a silica substrate [42]. While metamaterials rely on engineered material parameters to manipulate light during propagation, metasurfaces achieve comparable functionalities within an ultrathin layer, enabling more compact and efficient optical components. Their two-dimensional nature provides direct access to the phase front of light, making them well suited for applications such as beam shaping while also facilitating integration into other photonic platforms for on-chip applications [1].

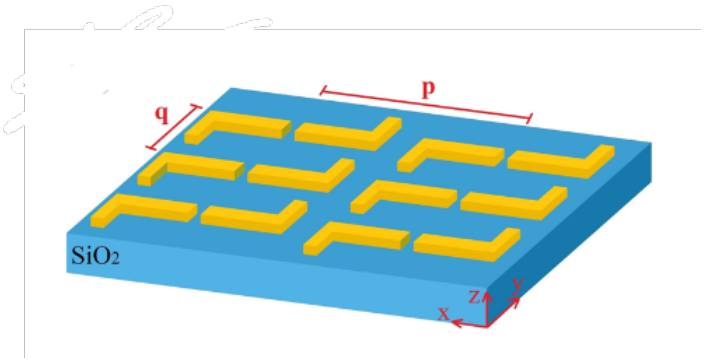

FIGURE 1.2: Schematic of a metasurface composed of a periodic array of L-shaped gold nanoantennas on a silica substrate. From Ref. [42].

1.3 Meta-atom

Meta-atoms, commonly referred to as nanoantennas, constitute the fundamental building blocks of metasurfaces. Based on their material composition, they can be broadly classified as plasmonic, dielectric, or semiconductor-based nanoantennas. Their dimensions, geometry, material composition, orientation, and spatial arrangement can be engineered to achieve a desired optical response [1], [43]. Individually, nanoantennas receive incident electromagnetic radiation and reradiate it with a modified amplitude, phase, and

polarization. When arranged in an array, their individual responses and mutual interactions determine the collective behavior of the metasurface. Consequently, spatially varying the properties of the nanoantennas across a surface enables functionalities such as beam steering, focusing, polarization conversion, and spectral control [1]. The principal classes of nanoantennas and their most important characteristics are reviewed in the following subsections.

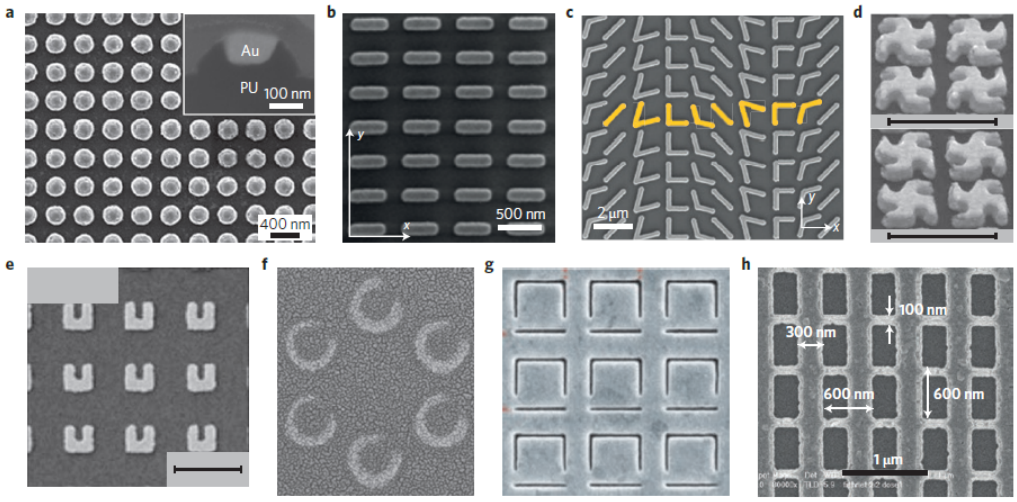

FIGURE 1.3: SEM images of common meta-atom geometries, including nanodisks, nanorods, V-shaped antennas, split-ring resonators, and fishnet structures. From Ref. [44].

Figure 1.3 shows several widely studied meta-atom geometries compiled by Meinzer et al. [44].

In order to study the optical response of meta-atoms, whether plasmonic or dielectric, it is first necessary to understand their dielectric function, which is fundamentally governed by their electronic properties. The dielectric response associated with bound electrons can be approximated using the classical harmonic-oscillator model introduced by Hendrik Lorentz. Within this framework, the dielectric function of a nonconducting material is expressed as [45], [46]

$$\varepsilon(\omega) = \varepsilon_\infty + \frac{f\,\omega_0^2}{\omega_0^2 - \omega^2 - i\gamma\omega}, \tag{1.1}$$

where ε_∞ is the high-frequency permittivity, f is the oscillator strength, ω_0 is the resonance frequency associated with bound electrons, and γ is a phenomenological damping constant.

For metals, the contribution of free electrons must also be included. This leads to the Lorentz–Drude model, in which the dielectric function is written as [45], [46]

$$\varepsilon(\omega) = \varepsilon_\infty - \frac{\omega_p^2}{\omega^2 + i\gamma_e\omega} + \sum_j \frac{f_j\,\omega_j^2}{\omega_j^2 - \omega^2 - i\gamma_j\omega}, \tag{1.2}$$

where the first term after ε_∞ describes the free-electron (Drude) response, characterized by the plasma frequency ω_p and damping constant γ_e. The summation accounts for bound-electron (Lorentz) oscillators, where f_j, ω_j, and γ_j denote the oscillator strength, resonance frequency, and damping constant of the j-th transition, respectively [45], [46].

The relative contributions of bound and free electrons determine the complex dielectric function, $\varepsilon(\omega) = \varepsilon'(\omega) + i\varepsilon''(\omega)$, and consequently the optical behavior of the material. The real part, ε', governs field propagation and confinement, whereas the imaginary part, ε'', represents optical loss. In dielectric materials, the bound-electron response generally produces a positive real permittivity with relatively low loss. In metals, the free-electron Drude contribution can produce a negative real permittivity below the screened plasma frequency. When this negative permittivity is combined with sufficiently low loss and an appropriate dielectric environment, collective oscillations of the conduction electrons couple to electromagnetic fields, giving rise to plasmonic modes. Semiconductors exhibit an intermediate and tunable response governed by their band structure, interband transitions, and free-carrier concentration [45], [46]. Based on these distinct electronic and dielectric responses, meta-atoms can therefore be broadly classified as plasmonic, dielectric, or semiconductor. These three classes, along with their underlying physical mechanisms and design principles, will be discussed in detail in the following sections.

1.3.1 Plasmonic meta-atom

Plasmonics describes the interaction between electromagnetic fields and the conduction electrons in metals, enabling the confinement of light to sub-wavelength dimensions [45], [46]. This behavior arises from the collective response of free electrons to an external electromagnetic field and can be accurately described within the framework of classical electromagnetism using Maxwell's equations. The optical response of metals is governed by their complex dielectric function, which captures both the effect of bound charges and the motion of free electrons.

A key feature of metallic systems is their strongly frequency-dependent dielectric response. At low frequencies, metals behave as good conductors, reflecting incident electromagnetic waves with minimal field penetration. As the frequency increases toward the visible regime, the electromagnetic field penetrates deeper into the metal, and dissipative effects become significant. This behavior is described by the free-electron model, in which conduction electrons respond to the applied field as a damped free particle, characterized by a plasma frequency and a relaxation time [45].

At the nanoscale, this electronic response gives rise to plasmonic behavior in metallic nanoparticles. When light interacts with a nanoparticle, the electric field displaces the conduction electrons relative to the positively charged ionic background. This charge separation produces a restoring force, leading to a collective oscillation of electrons that can be described as a driven harmonic oscillator. As a result, a resonance in the particle polarizability emerges, where the optical response is strongly enhanced and accompanied by a characteristic phase shift [46].

An important consequence of this response is the existence of collective charge oscillations known as plasmons. In bulk metals, these occur at the plasma frequency and correspond to longitudinal modes of the electron gas. At interfaces or in nanostructures, these excitations couple with electromagnetic

fields, giving rise to surface and localized plasmons. At a planar metal-dielectric interface, surface plasmon resonance (SPR) occurs when the wavevector of incident light matches that of the surface plasmon, leading to a propagating electromagnetic wave bound to the interface [45]. This resonant condition is highly sensitive to the refractive index near the metal surface, forming the basis for label-free biosensing and real-time molecular interaction monitoring [47]. In particular, localized surface plasmon resonances in metallic nanoparticles enable strong confinement and enhancement of electromagnetic fields at the nanoscale [45]. These effects form the physical basis for many applications in plasmonic metasurfaces and nanophotonics.

Noble metals, particularly gold, are widely employed in plasmonic systems over a broad spectral range. Figure 1.4 presents the optical response of a single gold nanoparticle for different radii.

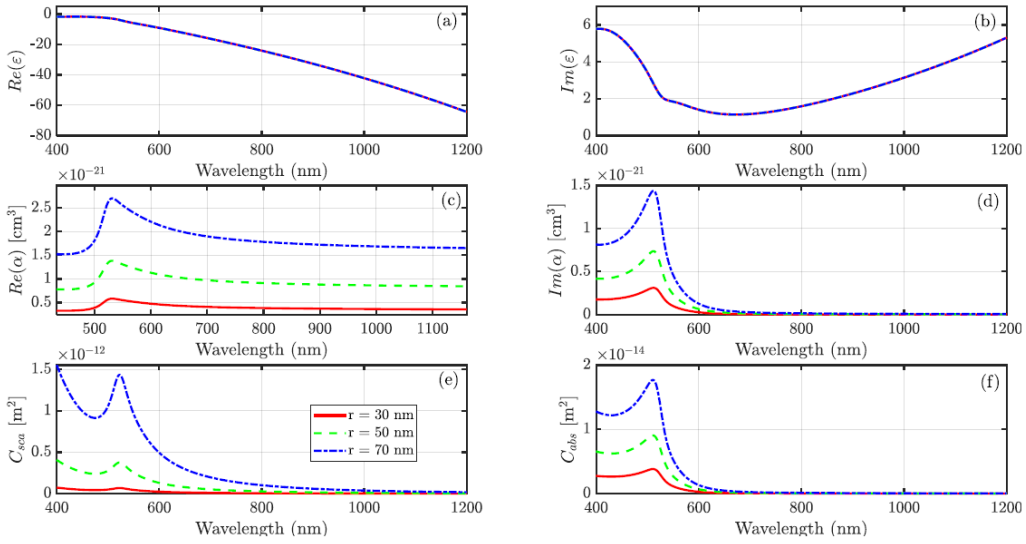

FIGURE 1.4: (a) Real and (b) imaginary parts of gold permittivity. (c) The real and (d) imaginary parts of polarizability for gold nanoparticles with three different radii. (e) The SCS and (f) the ACS of gold nanoparticles [48].

The nanoparticle polarizability exhibits a pronounced peak when the Fröhlich condition, $\varepsilon(\omega) \approx -2\varepsilon_m$, is satisfied, corresponding to the excitation of localized surface plasmon resonances (LSPRs), as shown in Fig. 1.4(c) and (d) [45], [46]. At this wavelength, the optical response is determined by two

channels: a radiative contribution associated with scattering into free space and a non-radiative contribution due to absorption within the particle. The scattered and absorbed cross sections, calculated are presented in Fig. 1.4 (e) and (f), respectively. The maxima observed in the scattering cross section (SCS) and absorption cross section (ACS) reflect this resonant behavior. Moreover, both SCS and ACS increase with particle radius, indicating a stronger light-matter interaction for larger nanoparticles.

1.3.2 Dielectric meta-atom

Despite the advantages discussed in the previous subsection, plasmonic meta-atoms suffer from intrinsic Ohmic losses and generally exhibit a weak magnetic response at optical frequencies. In noble metals such as gold and silver, electron scattering and interband transitions cause absorption and Joule heating. This heating can modify the refractive index of the structure and its environment through the thermo-optic effect and, at high illumination intensities, may deform or damage the nanostructure [49]. These limitations motivated the development of high-refractive-index dielectric and semiconductor meta-atoms as low-loss alternatives to plasmonic structures [50].

The theoretical foundation for understanding these structures originates from Mie's analytical solution for electromagnetic scattering by spherical particles [51]. Later, Kerker et al. investigated particular solutions for magnetodielectric particles and demonstrated that interference between their electric- and magnetic-dipole responses could suppress scattering in either the backward or forward direction [52]. These conditions, introduced in 1983, became known as the Kerker conditions and provided an important conceptual basis for controlling light scattering with subwavelength dielectric particles.

The possibility of realizing such magnetodielectric responses at optical frequencies was subsequently explored using high-index semiconductor particles. Evlyukhin and coauthors theoretically investigated the optical response

of silicon nanoparticle arrays in 2010 [53], while García-Etxarri and coauthors predicted a strong magnetic response from submicrometre silicon particles in 2011 [54]. In 2012, Evlyukhin and coauthors experimentally demonstrated magnetic-dipole resonances in dielectric nanospheres at visible wavelengths [55]. During the same year, Kuznetsov et al. experimentally showed that spherical silicon nanoparticles with diameters between approximately 100 and 200 nm support strong magnetic-dipole resonances that can be tuned throughout the visible spectrum by changing the particle size [56].

Unlike metallic particles, high-index dielectric particles allow electromagnetic fields to penetrate their volume. The resulting phase retardation produces circulating displacement currents, enabling the excitation of an intrinsic magnetic-dipole mode [54], [56]. This resonance approximately occurs when the wavelength inside the particle becomes comparable to its diameter, $2R \approx \lambda/n$. Dielectric particles can therefore support electric- and magnetic-dipole resonances of comparable strengths, as well as higher-order electric and magnetic multipoles [50]. Their spectral positions and relative amplitudes can be controlled through the particle size, refractive index, material, and geometry. Detailed Mie-theory and multipolar descriptions of these modes are presented in the following chapter.

In 2013, Fu et al. experimentally demonstrated directional visible-light scattering from silicon nanoparticles [57]. In parallel, Staude and coauthors showed that the interference between electric- and magnetic-dipole resonances in silicon nanodisks could be engineered to control the direction of scattering [58]. These studies demonstrated experimentally that high-index dielectric particles could approximate the magnetodielectric response considered by Kerker. Subsequent investigations extended this concept to spheroids, disks, dimers, oligomers, core–shell particles, and structures made from materials such as Si, Ge, GaP, and GaAs [50].

Building on the control of resonant scattering at the individual-particle level, these principles have been employed collectively in dielectric metasurfaces to manipulate transmitted and reflected light. When electric- and magnetic-dipole resonances overlap with comparable amplitudes and appropriate phases,

their interference can suppress backward scattering and enhance forward transmission. In 2015, Decker et al. experimentally demonstrated high-efficiency Huygens metasurfaces based on silicon nanodisks, achieving nearly unity transmission and complete 2π control over the transmission phase [59]. Alternatively, the collective interference of the resonant modes can produce destructive interference in transmission and correspondingly strong reflection [60]. These developments enabled the use of dielectric metasurfaces for efficient beam steering, wavefront shaping, focusing, and other flat-optical applications [50].

Beyond directional dipolar scattering, additional optical responses can be obtained by controlling interference among resonant modes. In 2012, Miroshnichenko and Kivshar theoretically demonstrated Fano resonances in all-dielectric oligomers arising from interference between individual and collective resonant modes [61]. In 2015, Miroshnichenko and co-workers experimentally observed an anapole state in silicon nanodisks [62]. This mode results from destructive interference between electric- and toroidal-dipole radiation, suppressing far-field scattering while maintaining strong field confinement inside the particle.

Beyond their important role in controlling linear light scattering, high-index dielectric nanostructures have emerged as promising platforms for nonlinear optics because their multipolar resonances provide greater control over local fields, even in simple geometries such as cylinders, while maintaining relatively low dissipative losses [63]. In 2014, Shcherbakov and coauthors demonstrated enhanced third-harmonic generation (THG) from silicon nanodisks driven by their magnetic-dipole resonances [34]. In 2015, Carletti and coauthors theoretically predicted enhanced second-harmonic generation (SHG) from AlGaAs nanoantennas excited near a magnetic-dipole resonance [64]. This was followed in 2016 by the experimental demonstration of resonantly enhanced SHG from GaAs all-dielectric metasurfaces by Liu and coauthors [65], and by the realization of monolithic AlGaAs second-harmonic nanoantennas by Gili and coauthors [66]. In the same year, Grinblat and coauthors demonstrated enhanced THG from individual germanium nanodisks excited near an anapole mode [67]. These developments

established dielectric resonators as efficient nonlinear nanoantennas and motivated subsequent research on collective, Fano, anapole, and high-Q resonances for enhancing and controlling nonlinear frequency conversion.

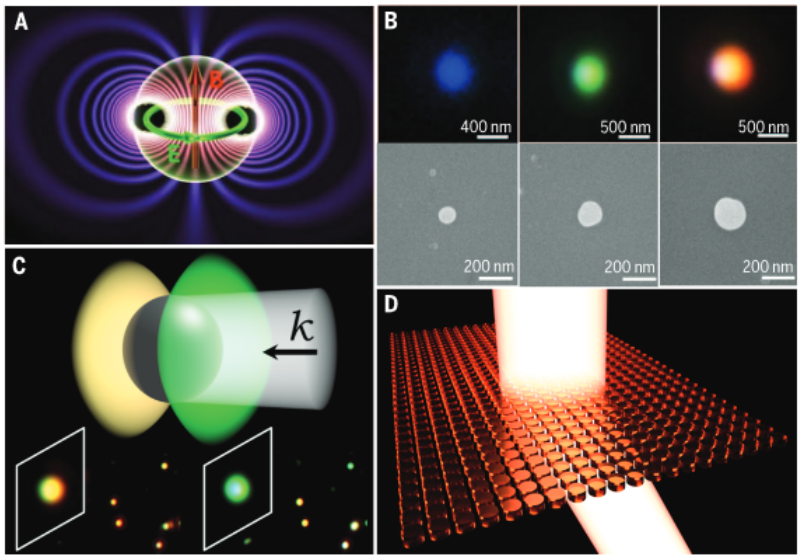

FIGURE 1.5: Manifestations of all-dielectric nanophotonics: (a) magnetic-dipole field distribution, (b) experimental optical magnetic response, (c) unidirectional scattering from a dielectric nanoparticle, and (d) light manipulation using a highly transparent Huygens metasurface. From Ref. [50].

Figure 1.5, presented by Kuznetsov and coauthors, illustrates the development of all-dielectric nanophotonics, from the excitation of magnetic-dipole resonances in individual dielectric nanoparticles to directional light scattering and highly transmissive Huygens metasurfaces [50].

1.3.3 III–V semiconductors

III–V semiconductors are alloys composed of two (binary), three (ternary), or four (quaternary) elements from group III, such as Al (aluminum) and Ga (gallium), and group V, such as P (phosphorus) and As (arsenic), of the periodic element table. These compounds exhibit flexibility in terms of bandgap energy and lattice constant, and they play a crucial role in optoelectronics. Generally, ternary and quaternary compounds can be expressed as $A_xB_{1-x}C$

and $A_xB_{1-x}C_yD_{1-y}$, respectively, where A, B, C, and D are elements from groups III and V, and x and y, with $0 < x, y < 1$, represent the fractions of the corresponding elements in the compound. Material parameters such as lattice constant, bandgap energy E_g, refractive index, and nonlinear optical coefficients vary with composition through the parameters x and y [68].

Although silicon is at the heart of photonic integrated circuits, it has an indirect bandgap that prevents it from functioning as an efficient light source. In contrast, most III–V compounds have a direct bandgap [68], [69].

The bandgap energy or lattice constant can be calculated using Vegard's law, which linearly interpolates between the semiconductors AC and BC:

$$T_{ABC}(x) = xT_{AC} + (1 - x)T_{BC}. \tag{1.3}$$

III-V semiconductors also have the advantage of a short electron lifetime compared to silicon, making them suitable for switching applications. For example, the recombination rate of GaAs is at least three orders of magnitude higher than that of silicon.

Another advantage of III–V semiconductors is their relatively high nonlinear optical coefficients. For instance, InGaAsP and AlGaAs have third-order susceptibilities $\chi^{(3)}$ of 4.2×10^{-10} esu and 4.1×10^{-11} esu, respectively, which are higher than that of silicon. Additionally, most III–V semiconductors have crystalline structures such as wurtzite or zincblende, which are noncentrosymmetric, a feature absent in silicon. This lack of inversion symmetry leads to significant second-order susceptibility $\chi^{(2)}$ in III–V semiconductors [70].

For example, AlGaAs has a zincblende crystal structure. Due to this crystal symmetry, its linear susceptibility $\chi^{(1)}$ is usually treated as isotropic, while its second-order susceptibility $\chi^{(2)}$ has only one independent nonzero tensor component which is commonly expressed as [70]

$$\chi^{(2)}_{xyz} = \chi^{(2)}_{xzy} = \chi^{(2)}_{yxz} = \chi^{(2)}_{yzx} = \chi^{(2)}_{zxy} = \chi^{(2)}_{zyx} \tag{1.4}$$

The magnitude of the second-order susceptibility in AlGaAs is typically on the order of $\sim$ 100–200 pm/V, depending on the wavelength and material composition [70].

In this thesis, we use these properties, together with the high refractive index and large second-order nonlinear susceptibility of AlGaAs, to design nonlinear metasurfaces.

1.4 Theoretical Description of Light Scattering by Nanoantennas

The interaction of light with nanoantennas can be described by solving Maxwell's equations under the appropriate boundary conditions. However, exact analytical solutions are available only for relatively simple geometries. A notable example is the rigorous solution developed by Gustav Mie for the scattering of light by a homogeneous sphere [45], [71]. Mie theory demonstrates that the optical response of a nanoparticle can be expressed as a series of electric and magnetic multipolar contributions. The excitation, spectral position, and strength of these contributions depend on the particle's size, shape, material composition, and surrounding medium. This framework therefore provides a fundamental basis for understanding light scattering by nanoantennas and for extending the analysis to more complex nanostructures.

Here, as a representative example, we consider light scattering from a spherical particle whose size is much smaller than the wavelength. More complex situations will be addressed in the next sections.

In the quasistatic approximation, light scattering by such a particle is described by solving Laplace's equation for the scalar electric potential,

$$\nabla^2 \Phi = 0, \qquad \mathbf{E} = -\nabla \Phi, \tag{1.5}$$

subject to boundary conditions at the particle surface $r = a$, requiring continuity of the potential and of the normal component of the displacement

field:

$$\Phi_{\text{in}}|_{r=a} = \Phi_{\text{out}}|_{r=a}, \qquad \varepsilon_p \left.\frac{\partial \Phi_{\text{in}}}{\partial r}\right|_{r=a} = \varepsilon_m \left.\frac{\partial \Phi_{\text{out}}}{\partial r}\right|_{r=a}, \tag{1.6}$$

where a is the particle radius, and ε_p and ε_m denote the dielectric functions of the particle and surrounding medium, respectively. The system is driven by an external uniform electric field $\mathbf{E}_0$.

By comparing the resulting scattered potential with that of an induced dipole, the effective dipole moment can be expressed as [45], [71]

$$\mathbf{p} = 4\pi\varepsilon_m(\omega)a^3 \frac{\varepsilon_p(\omega) - \varepsilon_m(\omega)}{\varepsilon_p(\omega) + 2\varepsilon_m(\omega)} \mathbf{E}_0 \tag{1.7}$$

The corresponding polarizability is given by [45], [71]

$$\alpha(\omega) = 4\pi a^3 \frac{\varepsilon_p(\omega) - \varepsilon_m(\omega)}{\varepsilon_p(\omega) + 2\varepsilon_m(\omega)} \tag{1.8}$$

Once the polarizability is known, the scattering cross section (C_{sca}) is given by [45], [71]

$$C_{\text{sca}}(\omega) = \frac{\omega^4}{6\pi c^4} \left(\frac{\varepsilon_m}{\varepsilon_0}\right)^2 |\alpha(\omega)|^2 \tag{1.9}$$

absorption cross section (C_{abs}) by [45], [71]

$$C_{\text{abs}}(\omega) = \frac{\omega}{c} \left(\frac{\varepsilon_m}{\varepsilon_0}\right)^{1/2} \text{Im}[\alpha(\omega)] \tag{1.10}$$

and extinction cross section (C_{ext}) by [45], [71]

$$C_{\text{ext}}(\omega) = C_{\text{sca}}(\omega) + C_{\text{abs}}(\omega) \tag{1.11}$$

$$C_{\text{ext}}(\omega) = \frac{\omega}{c}\left(\frac{\varepsilon_m}{\varepsilon_0}\right)^{1/2} \text{Im}[\alpha(\omega)] + \frac{\omega^4}{6\pi c^4}\left(\frac{\varepsilon_m}{\varepsilon_0}\right)^2 |\alpha(\omega)|^2 \tag{1.12}$$

In the following sections, we present the exact scattering response of spherical particles using Mie theory and multipole decomposition.

1.5 Collective effects in metasurfaces

The optical response of a metasurface is not solely determined by the resonances of its individual meta-atoms. In a periodic array, the fields scattered by different elements interact coherently, giving rise to collective modes whose spectral position, linewidth, and radiation pattern depend on the lattice periodicity, array symmetry, surrounding refractive index, and angle of illumination [72], [73].

The historical foundations of these collective effects can be traced to the diffraction anomalies observed by Wood in 1902 [74]. In 1907, Rayleigh explained that one class of these anomalies occurs when a diffraction order propagates parallel to the grating surface [75]. Although a Rayleigh anomaly is not itself a resonance, it provides the diffraction condition required for the formation of several collective optical modes. In dielectric structures, Magnusson, Wang, and their collaborators established the theoretical basis of guided-mode resonance filters in the early 1990s [76], [77]. In this mechanism, the periodic modulation provides the additional in-plane momentum required to couple incident light to a leaky mode supported by a dielectric layer.

The significance of collective effects in metallic periodic structures was further demonstrated in 1998, when Ebbesen et al. reported extraordinary optical transmission through arrays of subwavelength holes in metallic films [78]. These observations demonstrated that the response resulted from collective interactions involving the periodic structure rather than from the independent transmission of individual holes.

A major step toward the development of surface-lattice resonances was taken in 2004 by Zou et al. predicted remarkably narrow plasmonic resonances in periodic silver-nanoparticle arrays [79]. In 2008, Auguié and Barnes experimentally demonstrated collective resonances in two-dimensional arrays of gold nanorods [72]. During the same year, Kravets et al. observed extremely narrow resonances near the Rayleigh cutoff wavelength [80]. These studies established that coupling between the localized plasmonic response of individual particles and lattice diffraction can produce a collective resonance considerably narrower than the resonance of an isolated particle. In 2009, Vecchi et al. showed that lattice resonances in periodic plasmonic nanoantenna arrays can enhance and control directional optical emission [81]. In 2011, Rodriguez and coauthors demonstrated the coupling of bright and dark surface-lattice resonances in two-dimensional plasmonic arrays [82].

Another important development involved trapped modes and bound states in the continuum (BICs). In 2007, Fedotov and coauthors demonstrated high-Q trapped modes in asymmetric planar metamaterials. The nearly out-of-phase currents in different parts of the unit cell suppressed the net electric-dipole radiation, resulting in a narrow resonance [83]. In 2008, Marinica et al. theoretically demonstrated photonic bound states in the continuum in periodic dielectric structures. In these states, radiation is completely suppressed even though the mode lies within the radiation continuum [84]. An ideal BIC cannot be excited directly from the far field; however, controlled symmetry breaking transforms it into an accessible quasi-BIC with a finite but high quality factor.

In 2018, Koshelev et al. established the connection between high-Q resonances in asymmetric dielectric metasurfaces and quasi-BICs. They showed that the radiative quality factor can be controlled by varying the degree of structural asymmetry [85]. These developments illustrate how diffraction, coherent inter-particle coupling, and symmetry can transform localized meta-atom responses into narrow collective resonances of the entire metasurface.

1.6 Nonlinear Optics

Nonlinear optics describes the interaction of intense light with matter, where the induced polarization exhibits a nonlinear dependence on the electric field amplitude. In many practical situations, this response can be treated within the perturbative regime, in which the polarization is expressed as a power series in the applied electric field. Accordingly, the induced polarization $\mathbf{P}$ can be written in terms of the electric field $\mathbf{E}$ as:

$$\mathbf{P} = \varepsilon_0 \left[\chi^{(1)}\mathbf{E} + \chi^{(2)}\mathbf{EE} + \chi^{(3)}\mathbf{EEE} + \cdots \right], \tag{1.13}$$

where ε_0 is the permittivity of free space and $\chi^{(1)}$ is a second-rank tensor describing the linear response of the material. The higher-order terms describe the nonlinear response, where $\chi^{(n)}$ is the nth-order nonlinear susceptibility and is an $(n+1)$ rank tensor [70].

In component form, the polarization can be written as

$$P_i = \varepsilon_0 \left(\chi^{(1)}_{ij} E_j + \chi^{(2)}_{ijk} E_j E_k + \chi^{(3)}_{ijkl} E_j E_k E_l + \cdots \right), \tag{1.14}$$

where P_i and E_i are the ith components of the induced polarization and applied optical field, respectively, with $(i, j, k, l) = (x, y, z)$. The nonlinear coefficient $\chi^{(n)}_{ijk}$ is related to the nth-order susceptibility.

1.6.1 Second-Harmonic Generation

Second-harmonic generation (SHG) is a nonlinear optical process in which two photons at frequency ω combine to generate a photon at frequency 2ω. The corresponding energy-level diagram is shown in Fig. 1.6. The nonlinear polarization responsible for SHG is given by

$$P^{(2)}(2\omega) = \varepsilon_0 \chi^{(2)} E^2(\omega), \tag{1.15}$$

which, in contracted form, can be written as

$$\begin{bmatrix} P_x(2\omega) \\ P_y(2\omega) \\ P_z(2\omega) \end{bmatrix} = 2\varepsilon_0 \begin{bmatrix} d_{11} & d_{12} & d_{13} & d_{14} & d_{15} & d_{16} \\ d_{21} & d_{22} & d_{23} & d_{24} & d_{25} & d_{26} \\ d_{31} & d_{32} & d_{33} & d_{34} & d_{35} & d_{36} \end{bmatrix} \begin{bmatrix} E_x^2(\omega) \\ E_y^2(\omega) \\ E_z^2(\omega) \\ 2E_y(\omega)E_z(\omega) \\ 2E_z(\omega)E_x(\omega) \\ 2E_x(\omega)E_y(\omega) \end{bmatrix}. \quad (1.16)$$

The effective nonlinear coefficient d_{eff} is related to the susceptibility through

$$d_{\text{eff}} = \frac{1}{2}\chi^{(2)}_{\text{eff}}. \quad (1.17)$$

Under the undepleted pump approximation, and by solving the nonlinear wave equation, the SHG conversion efficiency in a bulk nonlinear crystal of length L is found to scale as

$$\eta_{\text{SHG}} \propto |d_{\text{eff}}|^2 L^2 \,\text{sinc}^2\left(\frac{\Delta k L}{2}\right), \quad (1.18)$$

where $\Delta k = k(2\omega) - 2k(\omega)$ is the wavevector mismatch, and $\text{sinc}(x) = \sin(x)/x$.

Maximum conversion efficiency is achieved under perfect phase-matching conditions ($\Delta k = 0$). However, due to material dispersion, $n(2\omega) \neq n(\omega)$ in most crystals, and phase matching must be achieved through birefringence engineering or quasi-phase matching [70].

In this thesis, we focus on nonlinear metasurfaces. Unlike bulk crystals, metasurfaces rely on subwavelength resonant structures; therefore, the phase-matching condition is significantly relaxed due to the short interaction length.

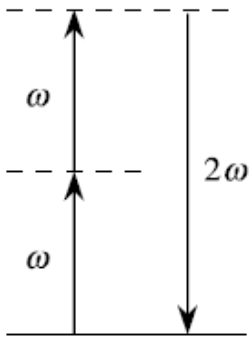

FIGURE 1.6: (a) Energy-level representation of second-harmonic generation (SHG). From Ref. [70].

1.6.2 Sum- and Difference-Frequency Generation

Beyond second-harmonic generation, second-order nonlinear interactions described by $\chi^{(2)}$ give rise to sum-frequency generation (SFG) and difference-frequency generation (DFG), for which the corresponding energy-level diagrams are shown in Fig. 1.7 [70].

In sum-frequency generation, two input fields at frequencies ω_1 and ω_2 interact to produce radiation at $\omega_3 = \omega_1 + \omega_2$, with nonlinear polarization

$$P(\omega_3) = 2\varepsilon_0 \chi^{(2)} E_1 E_2. \tag{1.19}$$

In a general tensor form, the polarization components can be expressed as

$$\begin{bmatrix} P_x(\omega_3) \\ P_y(\omega_3) \\ P_z(\omega_3) \end{bmatrix} = 4\varepsilon_0 \begin{bmatrix} d_{11} & d_{12} & d_{13} & d_{14} & d_{15} & d_{16} \\ d_{21} & d_{22} & d_{23} & d_{24} & d_{25} & d_{26} \\ d_{31} & d_{32} & d_{33} & d_{34} & d_{35} & d_{36} \end{bmatrix}$$

$$\times \begin{bmatrix} E_x(\omega_1)E_x(\omega_2) \\ E_y(\omega_1)E_y(\omega_2) \\ E_z(\omega_1)E_z(\omega_2) \\ E_y(\omega_1)E_z(\omega_2) + E_z(\omega_1)E_y(\omega_2) \\ E_x(\omega_1)E_z(\omega_2) + E_z(\omega_1)E_x(\omega_2) \\ E_x(\omega_1)E_y(\omega_2) + E_y(\omega_1)E_x(\omega_2) \end{bmatrix} \tag{1.20}$$

The factor of $4\varepsilon_0$ arises from permutation symmetry of the second-order susceptibility tensor.

SFG is commonly used for frequency upconversion, for example to generate tunable ultraviolet radiation by mixing a fixed-frequency visible laser with a tunable source, and is also widely applied in surface and interface spectroscopy [70].

In difference-frequency generation, the generated frequency is $\omega_3 = \omega_1 - \omega_2$, and the nonlinear polarization is given by

$$P(\omega_3) = 2\varepsilon_0 \chi^{(2)} E_1 E_2^*. \tag{1.21}$$

In this process, a photon at ω_1 is converted into photons at ω_2 and $\omega_3 = \omega_1 - \omega_2$, leading to amplification of the lower-frequency field. For this reason, DFG is also referred to as optical parametric amplification. the presence of the ω_2 field stimulates the emission of photons at ω_2 and ω_3. In the absence of the ω_2 field, the process reduces to weak spontaneous emission, known as parametric fluorescence or spontaneous parametric down-conversion.

DFG is commonly used for frequency downconversion, particularly for generating tunable infrared and terahertz radiation [70].

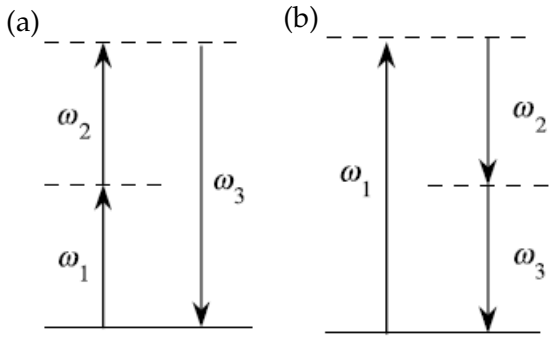

FIGURE 1.7: (a) Energy-level diagram illustrating a sum-frequency generation (SFG) and (b) difference-frequency generation (DFG). From Ref. [70].

1.6.3 Third-Order Nonlinear Processes

Third-order nonlinear interactions governed by the third-order susceptibility $\chi^{(3)}$ give rise to a variety of phenomena, including third-harmonic generation (THG). In THG, three photons at frequency ω combine to generate radiation at frequency 3ω. The corresponding nonlinear polarization is given by

$$P(3\omega) = \varepsilon_0 \chi^{(3)} E^3(\omega). \tag{1.22}$$

Figure 1.8 [70] illustrates the energy-level diagram associated with this process.

Another key third-order nonlinear process is four-wave mixing (FWM), in which interacting waves generate new frequency components. In degenerate four-wave mixing (DFWM), the idler frequency ω_i is related to the pump frequency ω_p and signal frequency ω_s as

$$\omega_i = 2\omega_p - \omega_s, \tag{1.23}$$

while in non-degenerate four-wave mixing (NDFWM), it is given by

$$\omega_i = \omega_{p1} + \omega_{p2} - \omega_s. \tag{1.24}$$

In these processes, the interacting fields are typically referred to as pump and signal waves, while the newly generated frequency component is called the idler. Four-wave mixing plays a central role in applications such as all-optical wavelength conversion and frequency-comb generation.

More generally, three waves at frequencies ω_1, ω_2, and ω_3 can interact to produce a new component at $\omega_1 + \omega_2 + \omega_3$. The corresponding nonlinear polarization can be written as

$$P(\omega_1 + \omega_2 + \omega_3) = 6\varepsilon_0 \chi^{(3)} E_1 E_2 E_3, \tag{1.25}$$

where the factor of 6 arises from the permutation symmetry among the interacting fields. This process is commonly referred to as third-order sum-frequency generation.

Beyond harmonic generation, third-order nonlinearities also give rise to intensity-dependent refractive index changes. In this regime, the refractive index can be expressed as

$$n = n_0 + n_2 I, \tag{1.26}$$

where n_0 is the linear refractive index, I is the optical intensity, and n_2 is the nonlinear refractive index coefficient. For isotropic media, n_2 is related to the third-order susceptibility by [70]

$$n_2 = \frac{3}{4n_0^2 \varepsilon_0 c} \chi^{(3)}. \tag{1.27}$$

This intensity dependence of the refractive index leads to important nonlinear effects such as self-focusing and self-phase modulation.

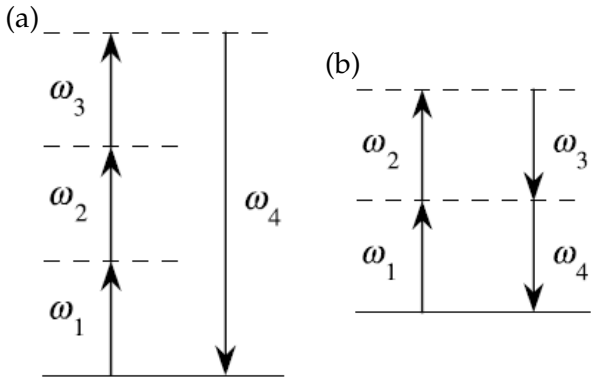

FIGURE 1.8: Two possible mixing processes can occur when three input waves interact in a medium characterized by a $\chi^{(3)}$ susceptibility. From Ref. [70]

.

1.6.4 Cascaded Nonlinearities

Cascaded nonlinearity refers to a process in which an effective higher-order nonlinear optical response arises from a sequence of lower-order interactions,

rather than from the direct higher-order susceptibility $\chi^{(n)}$. In particular, in materials with a strong second-order susceptibility $\chi^{(2)}$, third-order effects can be realized through second-order processes.

A representative example is third-harmonic generation achieved via cascading. In this case, the interaction proceeds in two steps: first, second-harmonic generation produces a field at 2ω from the fundamental frequency ω ($\omega + \omega \rightarrow 2\omega$); subsequently, sum-frequency generation between the fundamental and second-harmonic fields generates radiation at 3ω ($\omega + 2\omega \rightarrow 3\omega$). Although each step is governed by $\chi^{(2)}$, the overall process results in a nonlinear polarization that scales as E^3, corresponding to an effective third-order nonlinearity [70].

Cascaded nonlinearities are particularly advantageous in systems where the intrinsic higher-order susceptibilities are weak, while the lower-order processes are strong and efficiently phase-matched. Under such conditions, the sequential interactions can significantly enhance the efficiency of the resulting higher-order process.

Overall, cascading provides an alternative physical pathway for achieving higher-order frequency conversion by exploiting strong lower-order nonlinear interactions.

1.7 Nonlinear Metasurfaces

As reviewed in Section 1.1, nonlinear metasurfaces have evolved from early plasmonic structures to dielectric, high-Q, and nonlocal platforms capable of both enhancing and controlling nonlinear emission. The following discussion introduces the main physical mechanisms underlying these capabilities.

Nonlinear optical processes, including second-harmonic generation (SHG), third-harmonic generation (THG), and frequency mixing, enable the generation of new optical frequencies and support applications in spectroscopy, imaging, optical communication, and quantum photonics. However, these

processes are generally weak because the induced nonlinear polarization is much smaller than its linear counterpart. Representative nonlinear susceptibilities are on the order of $\chi^{(2)} \sim 10^{-12}\,\mathrm{m/V}$ and $\chi^{(3)} \sim 10^{-19}\,\mathrm{m^2/V^2}$, although their values vary considerably among materials [70]. Conventional nonlinear optical systems therefore commonly require high pump intensities, millimeter- to centimeter-scale interaction lengths, and careful phase matching to produce measurable signals. These requirements increase the dimensions and complexity of nonlinear devices and hinder their integration into compact photonic systems [23].

Nonlinear metasurfaces provide an alternative approach based on resonant light-matter interactions in ultrathin arrays of subwavelength nanoantennas. By tailoring the material, geometry, and arrangement of the constituent elements, metasurfaces can concentrate electromagnetic energy into small volumes and substantially enhance the local fields at the fundamental and generated frequencies. Because an nth-order nonlinear polarization depends on the nth power of the local electric field, even moderate local-field enhancement can significantly strengthen the nonlinear response. Furthermore, the resonances can be engineered at the pump frequency, the generated frequency, or both, thereby enhancing the excitation and radiation of the nonlinear signal [23]. Coupling among the nanoantennas can also produce collective high-Q modes that further improves the field confinement [86].

In addition to field enhancement, the reduced thickness of these systems fundamentally alters the role of phase matching. In bulk nonlinear media, efficient frequency conversion requires maintaining a fixed phase relationship between interacting waves over extended distances, which imposes strict constraints on material dispersion and geometry. In contrast, when the interaction length is much smaller than the wavelength, phase accumulation along the propagation direction becomes negligible. This effectively relaxes phase-matching requirements and allows nonlinear processes to occur efficiently without the need for complex dispersion engineering [87].

Another important mechanism arises from the ability to control structural symmetry. Second-order nonlinearities vanish in centrosymmetric media but

can be generated through symmetry breaking at the nanoscale [70]. By designing geometries that lack inversion symmetry, or by exploiting surface and interface contributions where symmetry is broken, it is possible to obtain effective second-order responses even in materials that are intrinsically centrosymmetric [88]. This provides a powerful degree of freedom for engineering nonlinear interactions that are not accessible in bulk materials.

the symmetry of the nanostructure can be tailored to selectively enhance or suppress specific harmonic orders; for example, a particular geometry may enhance the seventh harmonic while suppressing the fifth. Unlike bulk nonlinear crystals, where phase matching typically supports a single nonlinear process, the relaxed phase constraints in subwavelength systems allow multiple harmonic orders to coexist and be efficiently generated within the same platform. This enables simultaneous or selective enhancement of different nonlinear signals through appropriate structural design [23], [89].

Finally, nonlinear metasurfaces enable direct control over the phase of the generated fields through geometric phase engineering. By varying the orientation of the nanostructures, the nonlinear polarization acquires a spatially dependent phase, allowing precise shaping of the emitted harmonic wavefront. This enables functionalities such as beam steering, focusing, and holography at harmonic frequencies, which are not readily achievable in conventional bulk nonlinear media [90], [91].

Together, resonant field enhancement, relaxed phase-matching constraints, symmetry engineering, and nonlinear phase control distinguish nonlinear metasurfaces from conventional bulk optical systems. Their combination enables compact platforms that can not only enhance frequency conversion but also control the spectral, polarization, and spatial properties of the generated light. These principles provide the foundation for the nonlinear metasurface platforms investigated in the following chapters.

1.8 THz and infrared meta-filters

The mid- and far-infrared (IR) spectral regions, typically spanning wavelengths from approximately 2.5 to 100 μm, have attracted considerable attention due to their wide range of scientific and technological applications [92]. In astronomy, infrared radiation enables the observation of thermal emission from celestial objects and provides access to the characteristic spectral signatures of cosmic dust and molecules, offering valuable insights into star and planet formation, the composition of the interstellar medium, and the evolution of galaxies[93], [94]. In addition, many gases and organic compounds exhibit distinct absorption fingerprints within the mid- and far-infrared region, making these wavelengths highly suitable for spectroscopic applications such as gas sensing, air quality monitoring, and medical diagnostics [95], [96].

Optical bandpass filters are essential components in many infrared and terahertz (THz) systems. They selectively transmit a desired spectral band while rejecting unwanted wavelengths, thereby improving the signal-to-noise ratio and suppressing out-of-band signals. Such filters play an important role in communication and spectroscopic systems [97], where accurate wavelength selection is required. However, the development of high-performance active and passive THz devices remains challenging. Consequently, there is a growing demand for bandpass filters that provide high optical performance while maintaining robustness against thermal and mechanical variations. Commercial bandpass filters are available with center wavelengths in the 20–100 µm range. For example, Nielson Scientific offers single-layer metal-mesh bandpass filters with customizable center wavelengths and bandwidths [98]. However, standard commercial filters offer limited control over the passband shape. This limitation motivates the development of filters whose transmission spectra can be tailored to specific applications.

The emergence of metamaterials and metasurfaces has opened new possibilities for the realization of compact and high-performance optical and THz filters. By engineering the geometry and arrangement of subwavelength resonant elements, these artificially structured surfaces enable precise control

over the transmission bandwidth, resonance frequency, and overall spectral response through structural design. As a result, metasurface-based bandpass filters have attracted considerable attention for infrared and terahertz applications, owing to their compact size, high spectral selectivity, and compatibility with modern microfabrication technologies [96], [99].

Despite these advantages, the design of metasurface-based filters remains challenging because their performance is governed by a trade-off between structural complexity, material selection, and fabrication technology. Achieving the desired spectral response requires precise control of the unit-cell geometry, efficient impedance matching, and the suppression of parasitic losses over a broad frequency range. Furthermore, the targeted operating wavelength and application-specific requirements impose additional constraints on the desired filtering bandwidth. Consequently, a wide range of design strategies has been proposed to simultaneously achieve high transmission within the passband and strong suppression of out-of-band spectral leakage [96].

Conventional approaches for designing bandpass filters are commonly based on topographically patterned substrates and multilayer structures. In these designs, antireflection and high-transmission bands are achieved through mechanisms such as impedance matching, multiple-beam interference, and gradient refractive index engineering. One widely adopted approach to achieving ultrabroadband impedance matching utilizes a matching layer, enabling high optical transmission over broad spectral and angular ranges [96], [97], [99], [100]. Nowadays, these design concepts are widely employed and further developed for the realization of both narrowband and broadband metamaterial-based THz bandpass filters, with the aim of achieving structurally simple devices while maintaining high transmission efficiency.

In the following chapters, the detailed design strategy and fabrication steps for THz and infrared transmissive broadband bandpass filters based on multilayer complementary structures will be discussed.

1.9 Thesis Structure

This thesis investigates the physics and design of linear and nonlinear metamaterials and their two-dimensional counterparts, metasurfaces, with an emphasis on controlling light–matter interactions at the nanoscale. By engineering artificial nanostructures, we tailor optical responses for applications in sensing, imaging, and high-harmonic generation.

Chapter 2 establishes the theoretical foundation of this thesis. First, Mie theory is introduced through the scattering of light by spherical particles, including the resonance conditions and the extraction of multipolar coefficients. The contributions of different multipolar modes to linear and nonlinear optical processes are then discussed. Next, the coupling between meta-atoms is described mathematically, followed by an analysis of two widely studied collective resonances arising from interparticle interactions in metasurfaces: Fano and surface-lattice resonances. The theoretical and numerical approaches used to model nonlinear metasurfaces are subsequently presented, including the hydrodynamic model for nonlinear optical processes in plasmonic materials and nonlinear scattering theory for calculating far-field emission using the Lorentz reciprocity theorem. Finally, the theoretical principles underlying the design and operation of multilayer complementary filters for the terahertz and infrared spectral ranges are introduced.

Building on this framework, the subsequent chapters present targeted applications. Chapter 3 explores broadband transmissive THz metasurface filters operating near 30, 50, and 80 μm.

Chapter 4 focuses on near-field second-harmonic generation (SHG) microscopy of randomly oriented polar molecules, modeled using asymmetric plasmonic nanoparticles supporting LSPRs. The engineered structures enable enhanced nonlinear emission, validated through SHG imaging.

Chapter 5 introduces a multilayer metasurface architecture that integrates an SLR-supporting periodic layer beneath an LSPR-based nanoparticle layer.

This configuration enhances imaging performance by exploiting engineered coupling between the layers to improve spatial resolution.

Finally, Chapter 6 theoretically and experimentally investigates the nonlinear optical response of non-centrosymmetric gold nanostructures. The second-order hyperpolarizability tensors of the corresponding particles are extracted and analyzed using a spectroscopy-based measurement approach.

Overall, this work provides both theoretical modeling and experimental validation to advance the understanding and application of linear and nonlinear metasurfaces, particularly for microscopy and spectral filtering.

Chapter 2

Theoretical Foundations of Metasurfaces and metamaterials

In this chapter, we present the theoretical foundations required for the analysis of metamaterials and metasurfaces. We begin by describing the electromagnetic response of an isolated nanoparticle within a general framework applicable to both metallic and dielectric materials. The linear and nonlinear contributions of different multipolar modes to electromagnetic scattering and radiation are then discussed.

The formulation is subsequently extended to periodic arrays of nanoparticles by modeling them as interacting dipoles. Within this framework, two important collective phenomena, namely surface lattice resonances and Fano resonances, are introduced and their underlying physical mechanisms are discussed.

Next, nonlinear effects are incorporated into the response of both individual nanostructures and periodic arrays. Various theoretical approaches for describing the nonlinear optical response are presented, including the effective susceptibility formalism, equivalent circuit models, and the hydrodynamic model. The chapter then introduces nonlinear scattering theory, which provides the framework for calculating the far-field nonlinear radiation generated by these structures.

Finally, the computational methods employed throughout this thesis are presented. Overall, this chapter establishes the theoretical and numerical framework that forms the basis for the modeling and analysis of the linear and nonlinear optical response of the metasurfaces investigated in the following chapters.

2.1 Mie theory

Mie theory provides the exact analytical solution for the scattering of electromagnetic waves by a homogeneous spherical particle [45], [71], [101]. It is named after the German physicist Gustav Mie, who first published this solution in 1908. Since its introduction, Mie theory has become a fundamental framework for analyzing the interaction of electromagnetic waves with spherical particles over a broad range of sizes and optical properties, enabling accurate calculations of their scattering and absorption characteristics for arbitrary particle sizes relative to the wavelength [101], [102]. The theory considers a harmonic plane wave with angular frequency (ω) incident on a spherical particle. According to Maxwell's equations, the electromagnetic fields in regions of uniform dielectric permittivity (ε), in the absence of free charges and currents, can be expressed in terms of transverse magnetic (TM) and transverse electric (TE) modes as follows:

$$\mathbf{H} = \left(\mathbf{H}^{\mathrm{TM}} - \frac{i}{k_0} \sqrt{\frac{\varepsilon_0}{\mu_0}} \nabla \times \mathbf{E}^{\mathrm{TE}} \right) e^{-i\omega t}, \tag{2.1}$$

$$\mathbf{E} = \left(\mathbf{E}^{\mathrm{TE}} + \frac{i}{k_0 \varepsilon} \sqrt{\frac{\mu_0}{\varepsilon_0}} \nabla \times \mathbf{H}^{\mathrm{TM}} \right) e^{-i\omega t}, \tag{2.2}$$

where $\mathbf{H}^{\mathrm{TM}}$ and $\mathbf{E}^{\mathrm{TE}}$ denote the amplitude vectors of the TM and TE field components, respectively. The vacuum wavenumber is defined as $k_0 = \omega\sqrt{\varepsilon_0 \mu_0}$, with ε_0 and μ_0 being the permittivity and permeability of free space [101].

In spherical coordinates (r, θ, ϕ), the TM and TE fields are expanded using vector spherical harmonics, which separate the radial and angular dependences. This expansion is indexed by the orbital number l and azimuthal

number:

$$\mathbf{H}^{\mathrm{TM}} = \sum_{l=0}^{\infty} \sum_{m=-l}^{l} H_{lm} \left(\mathbf{e}_{\phi} \frac{\partial Y_{lm}}{\partial \theta} - \frac{\mathbf{e}_{\theta}}{\sin\theta} \frac{\partial Y_{lm}}{\partial \phi} \right), \tag{2.3}$$

$$\mathbf{E}^{\mathrm{TE}} = \sum_{l=0}^{\infty} \sum_{m=-l}^{l} E_{lm} \left(\mathbf{e}_{\phi} \frac{\partial Y_{lm}}{\partial \theta} - \frac{\mathbf{e}_{\theta}}{\sin\theta} \frac{\partial Y_{lm}}{\partial \phi} \right), \tag{2.4}$$

where $\mathbf{e}_r$, $\mathbf{e}_\theta$, and $\mathbf{e}_\phi$ are the unit vectors in the spherical coordinate system. The angular part of the solution is described by the scalar spherical harmonics:

$$Y_{lm}(\theta, \phi) = \sqrt{\frac{2l+1}{4\pi} \frac{(l-m)!}{(l+m)!}} P_l^m(\cos\theta) e^{im\phi}, \tag{2.5}$$

with $P_l^m(\cos\theta)$ representing the associated Legendre polynomials. The radial functions H_{lm} and E_{lm}, which are generally independent of each other, satisfy the same radial wave equation:

$$\frac{d^2 H_{lm}}{dr^2} + \frac{2}{r} \frac{dH_{lm}}{dr} - \left[\frac{l(l+1)}{r^2} - k_0^2 \varepsilon \right] H_{lm} = 0, \tag{2.6}$$

$$\frac{d^2 E_{lm}}{dr^2} + \frac{2}{r} \frac{dE_{lm}}{dr} - \left[\frac{l(l+1)}{r^2} - k_0^2 \varepsilon \right] E_{lm} = 0. \tag{2.7}$$

For a spherical particle of radius R, the radial functions are defined piecewise:

$$E_{lm} = \begin{cases} E_{lm}^{\mathrm{int}}, & r < R, \\ E_{lm}^{\mathrm{inc}} + E_{lm}^{\mathrm{sca}}, & r > R, \end{cases} \tag{2.8}$$

$$H_{lm} = \begin{cases} H_{lm}^{\mathrm{int}}, & r < R, \\ H_{lm}^{\mathrm{inc}} + H_{lm}^{\mathrm{sca}}, & r > R. \end{cases} \tag{2.9}$$

The incident, scattered, and internal field amplitudes are expressed in terms of spherical Bessel functions j_l (regular at the origin) and spherical Hankel

functions of the first kind $h_l^{(1)}$ (representing outgoing waves) [101]:

$$H_{lm}^{\text{inc}} = \tilde{H}_{lm} j_l(k_e r), \tag{2.10}$$
$$E_{lm}^{\text{inc}} = \tilde{E}_{lm} j_l(k_e r), \tag{2.11}$$
$$H_{lm}^{\text{sca}} = -a_l \tilde{H}_{lm} h_l^{(1)}(k_e r), \tag{2.12}$$
$$E_{lm}^{\text{sca}} = -b_l \tilde{E}_{lm} h_l^{(1)}(k_e r), \tag{2.13}$$
$$H_{lm}^{\text{int}} = d_l \tilde{H}_{lm} j_l(k_i r), \tag{2.14}$$
$$E_{lm}^{\text{int}} = c_l \tilde{E}_{lm} j_l(k_i r), \tag{2.15}$$

where $k_i = k_0\sqrt{\varepsilon_i}$ and $k_e = k_0\sqrt{\varepsilon_e}$ are the wavenumbers in the internal (particle) and external (surrounding) media, respectively. The internal and incident fields are expressed using the spherical Bessel functions j_l, as they remain regular and finite at the origin $r = 0$. In contrast, the scattered field is described by the spherical Hankel functions of the first kind $h_l^{(1)}$, which correspond to outgoing waves radiating outward from the particle [101].

The incident plane wave is assumed to be x-polarized and propagating along the z-direction:

$$\mathbf{E}^{\text{inc}} = \mathbf{e}_x E_0 e^{i(k_e r\cos\theta - \omega t)}, \tag{2.16}$$
$$\mathbf{H}^{\text{inc}} = \sqrt{\frac{\varepsilon_0\varepsilon_e}{\mu_0}}\mathbf{e}_y E_0 e^{i(k_e r\cos\theta - \omega t)}. \tag{2.17}$$

For a transparent external medium ($\operatorname{Im}\varepsilon_e = 0$), the spherical harmonic expansion yields the following amplitudes for the incident fields:

$$\tilde{H}_{lm} = -i^l\sqrt{\frac{\pi(2l+1)}{l(l+1)}}\sqrt{\frac{\varepsilon_0\varepsilon_e}{\mu_0}}\, m\delta_{m,\pm1}E_0, \tag{2.18}$$
$$\tilde{E}_{lm} = -i^{l+1}\sqrt{\frac{\pi(2l+1)}{l(l+1)}}\,\delta_{m,\pm1}E_0. \tag{2.19}$$

The Mie coefficients a_l, b_l, c_l, and d_l are determined by imposing the continuity of the tangential electric and magnetic field components at the particle

surface. They are given by:

$$a_l = \frac{q_i\psi_l(q_i)\psi_l'(q_e) - q_e\psi_l(q_e)\psi_l'(q_i)}{q_i\psi_l(q_i)\xi_l'(q_e) - q_e\xi_l(q_e)\psi_l'(q_i)}, \tag{2.20}$$

$$b_l = \frac{q_e\psi_l(q_i)\psi_l'(q_e) - q_i\psi_l(q_e)\psi_l'(q_i)}{q_e\psi_l(q_i)\xi_l'(q_e) - q_i\xi_l(q_e)\psi_l'(q_i)}, \tag{2.21}$$

$$c_l = \frac{q_i\psi_l(q_e)\xi_l'(q_e) - q_i\xi_l(q_e)\psi_l'(q_e)}{q_e\psi_l(q_i)\xi_l'(q_e) - q_i\xi_l(q_e)\psi_l'(q_i)}, \tag{2.22}$$

$$d_l = \frac{q_i\psi_l(q_e)\xi_l'(q_e) - q_i\xi_l(q_e)\psi_l'(q_e)}{q_i\psi_l(q_i)\xi_l'(q_e) - q_e\xi_l(q_e)\psi_l'(q_i)}, \tag{2.23}$$

where $\psi_l(q_i) = q_i j_l(q_i)$ and $\xi_l(q_e) = q_e h_l^{(1)}(q_e)$ are the Riccati–Bessel functions, with $q_i = k_i R$ and $q_e = k_e R$.

From the scattered fields obtained via this procedure, the total scattering and absorption cross-sections are computed by integrating the Poynting vector over a closed surface surrounding the particle:

$$\sigma_{\text{sca}} = \frac{2\pi}{k_e^2}\sum_{l=1}^{\infty}(2l+1)\left(|a_l|^2 + |b_l|^2\right), \tag{2.24}$$

$$\sigma_{\text{abs}} = \frac{2\pi}{k_e^2}\sum_{l=1}^{\infty}(2l+1)\left[\text{Re}(a_l + b_l) - \left(|a_l|^2 + |b_l|^2\right)\right]. \tag{2.25}$$

Here, the coefficients a_l and b_l correspond to the TM and TE spherical vector harmonics, respectively.

Because Mie theory is based on the linear response of the electromagnetic field, the incident fields can be decomposed into two parts, allowing us to study how each part separately induces the scattered and internal fields:

$$H_{lm}^{\text{inc}} = H_{lm}^{\text{inc},1} + H_{lm}^{\text{inc},2}, \tag{26}$$

$$E_{lm}^{\text{inc}} = E_{lm}^{\text{inc},1} + E_{lm}^{\text{inc},2}, \tag{27}$$

and

$$H_{lm}^{\text{sca}} = H_{lm}^{\text{sca},1} + H_{lm}^{\text{sca},2}, \tag{28}$$

$$E_{lm}^{\text{sca}} = E_{lm}^{\text{sca},1} + E_{lm}^{\text{sca},2}, \tag{29}$$

$$H_{lm}^{\text{int}} = H_{lm}^{\text{int},1} + H_{lm}^{\text{int},2}, \tag{30}$$

$$E_{lm}^{\text{int}} = E_{lm}^{\text{int},1} + E_{lm}^{\text{int},2}. \tag{31}$$

In particular, the incident fields can be decomposed into spherically outgoing and spherically incoming fields:

$$H_{lm}^{\text{inc},j} = \frac{1}{2}\widetilde{H}_{lm} h_l^{(j)}(k_e r), \tag{32}$$

$$E_{lm}^{\text{inc},j} = \frac{1}{2}\widetilde{E}_{lm} h_l^{(j)}(k_e r), \tag{33}$$

where $h_l^{(j)}(k_e r)$ are the spherical Hankel functions of the first and second kinds, with $j = 1, 2$ corresponding to the spherically outgoing and spherically incoming fields, respectively. The respective internal and scattered fields can then be written as follows:

$$\begin{aligned} H_{lm}^{\text{sca},j} &= -a_{lm}^{(j)} \widetilde{H}_{lm} h_l^{(1)}(k_e r), \\ E_{lm}^{\text{sca},j} &= -b_{lm}^{(j)} \widetilde{E}_{lm} h_l^{(1)}(k_e r), \\ H_{lm}^{\text{int},j} &= d_{lm}^{(j)} \widetilde{H}_{lm} j_l(k_i r), \\ E_{lm}^{\text{int},j} &= c_{lm}^{(j)} \widetilde{E}_{lm} j_l(k_i r). \end{aligned} \tag{34–37}$$

The new Mie coefficients for the spherically outgoing incident fields are

$$a_l^{(1)} = b_l^{(1)} = \frac{1}{2}, \qquad c_l^{(1)} = d_l^{(1)} = 0, \tag{38}$$

while for the spherically incoming incident fields,

$$a_l^{(2)} = \frac{1}{2}\frac{q_i \psi_l(q_i)\zeta_l'(q_e) - q_e \zeta_l(q_e)\psi_l'(q_i)}{q_i \psi_l(q_i)\xi_l'(q_e) - q_e \xi_l(q_e)\psi_l'(q_i)}, \tag{39}$$

$$b_l^{(2)} = \frac{1}{2}\frac{q_e \psi_l(q_i)\zeta_l'(q_e) - q_i \zeta_l(q_e)\psi_l'(q_i)}{q_e \psi_l(q_i)\xi_l'(q_e) - q_i \xi_l(q_e)\psi_l'(q_i)}, \tag{40}$$

$$c_l^{(2)} = \frac{1}{2}\frac{q_i\psi_l(q_e)\zeta_l'(q_e) - q_i\zeta_l(q_e)\psi_l'(q_e)}{q_e\psi_l(q_i)\xi_l'(q_e) - q_i\xi_l(q_e)\psi_l'(q_i)}, \tag{41}$$

$$d_l^{(2)} = \frac{1}{2}\frac{q_i\zeta_l(q_e)\xi_l'(q_e) - q_i\xi_l(q_e)\zeta_l'(q_e)}{q_i\psi_l(q_i)\xi_l'(q_e) - q_e\xi_l(q_e)\psi_l'(q_i)}. \tag{42}$$

As shown above, the spherically outgoing component of the incident field produces no internal field and cancels the incident field outside the sphere, resulting in a trivial solution of Maxwell's equations. Nevertheless, it generates a nonzero scattered field in the absence of induced currents inside the scatterer. This component is therefore referred to as a source-free scattered field. In contrast, the spherically incoming component produces nonzero internal electric and magnetic fields, giving rise to a current-sourced scattered field through the currents induced within the scatterer. Consequently, the electromagnetic fields in Mie theory, including the scattered field, can be decomposed into source-free and current-sourced components. The latter are generated by currents induced inside the scatterer, whereas the former arise as the trivial response of Maxwell's equations to the source-free incident fields. Importantly, the Mie coefficients associated with the source-free scattered fields are constant and independent of the particle size and material properties. Consequently, the effect of the scatterer is entirely determined by the scattered current-sourced fields [101].

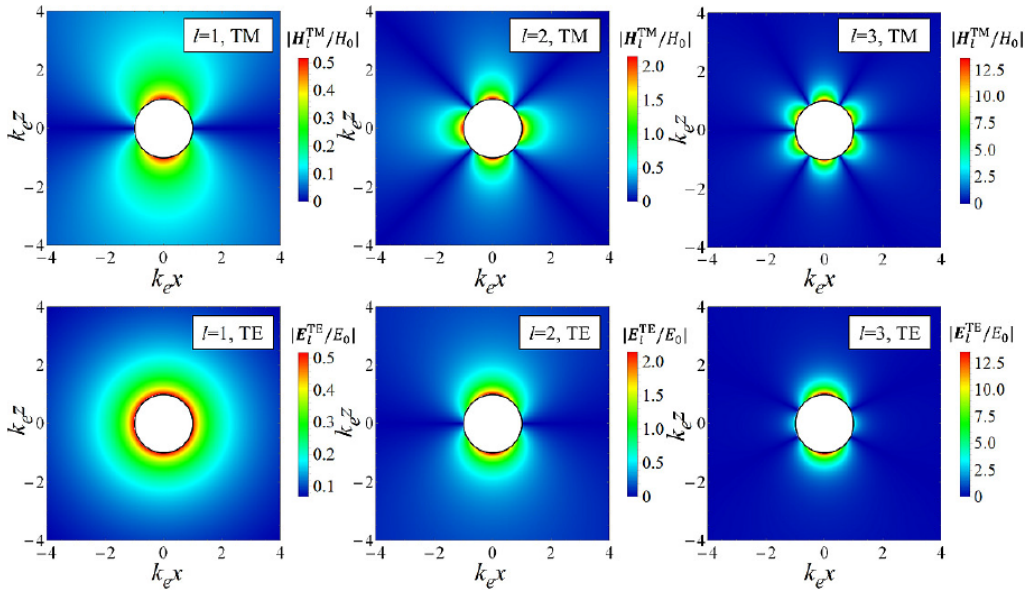

FIGURE 2.1: Source-free scattered field normalized to the incident amplitude for different l values and polarizations. From Ref. [101].

Akimov calculated the source-free scattered field distributions, normalized to the incident field amplitude, for different orbital indices l and polarizations, as shown in Fig. 2.1 [101].

2.1.1 Super-radiating and non-radiating states

Since the electromagnetic response is determined by the interference between the source-free and current-sourced fields, this interference can be either constructive or destructive. When one of the Mie coefficients, a_l or b_l, is equal to 1, the interference is constructive, corresponding to a super-radiating state, in which the channel's scattering cross section reaches its maximum value. Conversely, when one of these coefficients is equal to 0, the interference is destructive, corresponding to a non-radiating state, in which the channel's scattering cross section reaches its minimum value [101].

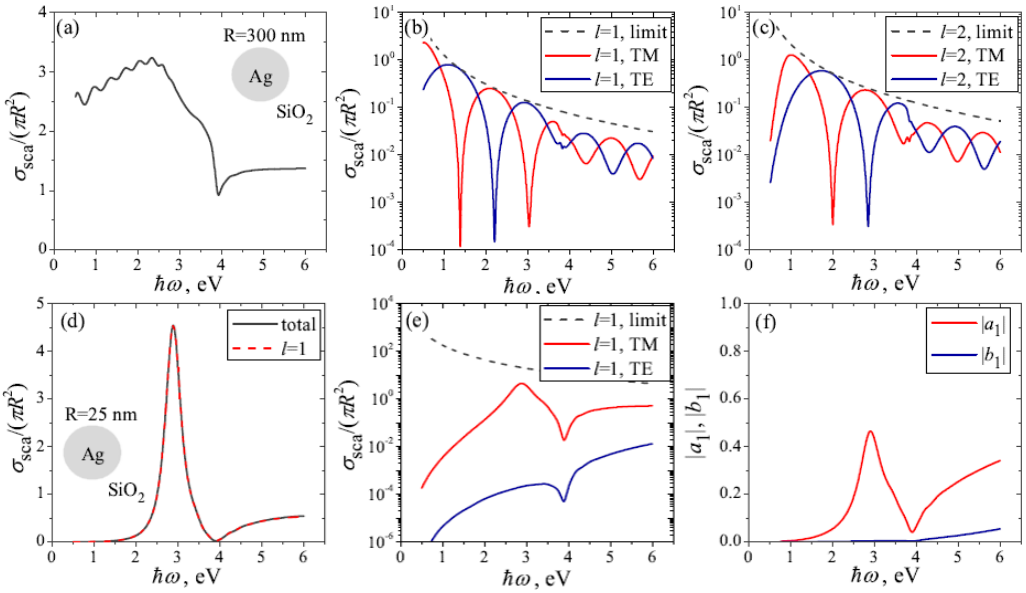

FIGURE 2.2: Normalized scattering cross section and the respective contributions of the TM and TE fields for $l = 1, 2$ in panels (a)–(f), for silver particles with radii of 300 nm and 25 nm embedded in SiO_2. From Ref. [101].

Figure 2.2 compares the normalized scattering cross-sections calculated by Akimov for silver spheres with radii of $R = 300$ nm and $R = 25$ nm [101]. The larger sphere exhibits multiple maxima and minima resulting from interference between different orbital contributions ($l = 1, 2$) for both TM and TE polarizations. In contrast, the scattering response of the smaller sphere ($R = 25$ nm) is dominated by the dipolar ($l = 1$) contribution, consistent with the Rayleigh scattering regime. As the particle size decreases, higher-order orbital contributions become less significant, resulting in fewer interference features in the scattering spectrum.

2.2 Multipole decomposition

The optical response of metamaterials is intrinsically linked to the electromagnetic properties of their individual meta-atoms. A powerful and widely adopted approach to analyzing such structures is multipole decomposition, which reduces the complex near-field distribution of a scatterer to a discrete set of multipole moments such as electric and magnetic dipoles, quadrupoles, and higher-order terms that fully describe its far-field radiation.

These moments serve as the basis for understanding light–matter interactions at the nanoscale, as the interference between different multipolar channels governs key scattering features, including Fano resonances, electromagnetically induced transparency, and perfect absorption [102], [103].

The multipole framework has become increasingly important in the development of all-dielectric meta-atoms, nanoantennas, and metasurfaces. Compared with metallic systems, all-dielectric structures offer lower absorption losses while supporting strong multipolar resonances. A prominent example is the Huygens' element, where balanced electric and magnetic dipole responses can suppress back scattering and enable full control over the transmitted phase. More broadly, multipole analysis provides valuable insight into a wide range of optical phenomena, including the determining the direction of optical forces, to quantifying near-surface directional coupling and evaluating the effective permeability of metamaterials [103].

In spherical geometries, this decomposition is naturally formulated within Mie theory, as described in the previous section. The scattered field is expanded in terms of transverse electric (TE) and transverse magnetic (TM) coefficients, labeled by the orbital index l, which denotes the multipole order (dipole for $l = 1$, quadrupole for $l = 2$, etc.). The polarization type determines the nature of the multipole: TM modes correspond to electric multipoles, while TE modes correspond to magnetic multipoles. For example, the Mie coefficients b_1 and a_1 represent the magnetic dipole (MD) and electric dipole (ED), respectively, while b_2 and a_2 correspond to the magnetic and electric quadrupoles, respectively [102].

Although conventional Mie theory is formulated for spherical particles, its framework can be extended to more complex geometries to determine the corresponding multipole coefficients and expand the scattered and internal fields in terms of these multipolar contributions.

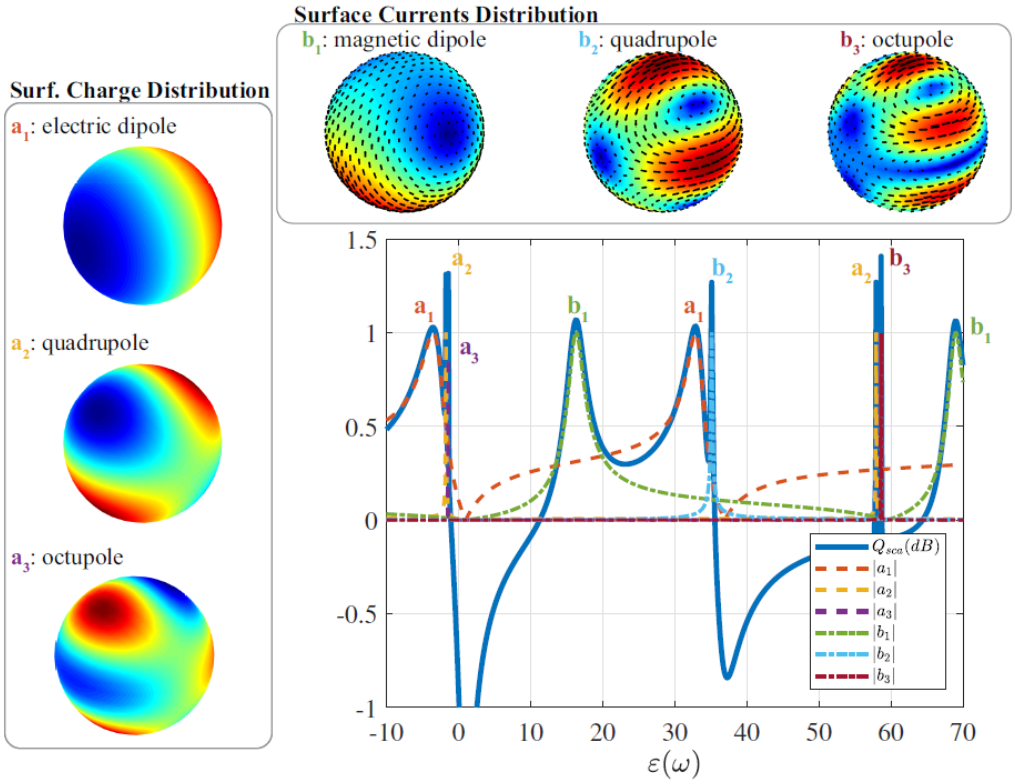

FIGURE 2.3: Total scattering efficiency (blue line, logarithmic scale) versus permittivity (lossless) for size parameter $x = 0.75$ ($x = k_0 r = 2\pi r/\lambda$). The dashed and dash-dot lines show the absolute values of the first three electric (a_1, a_2, a_3) and magnetic (b_1, b_2, b_3) multipole coefficients, respectively. The insets display the corresponding surface charge (electric multipoles) and surface current (magnetic multipoles) distributions. From Ref. [102].

As depicted in Figure 2.3, Tzarouchis and Sihvola calculated the scattering efficiency and the first three electric and magnetic multipole coefficients for a sphere with a fixed size parameter of $x = 0.75$ [102]. The inset figures illustrate the corresponding surface charge and current distributions for the a_1, a_2, a_3 and b_1, b_2, b_3 coefficients, respectively. The magnetic multipoles exhibit pronounced circulating surface current distributions, corresponding to magnetic dipole, quadrupole, and octupole configurations. This phenomenon is particularly important for enabling magnetic responses in dielectric spheres at optical and near-infrared frequencies, where naturally occurring magnetic materials are generally unavailable. In contrast, the electric multipoles are

characterized by surface charge distributions with dipolar, quadrupolar, and octupolar symmetries. However, the magnetic resonances appear only for positive permittivity values (the dielectric regime). This indicates that, for a subwavelength metallic sphere at the considered size parameter, the induced surface currents cannot form the circulating patterns required to support magnetic multipolar resonances [102].

2.3 Coupled Meta-atoms

2.3.1 Coupled dipole approximation

There are several approaches to modelling the interactions between coupled nanoparticles. Here, we approximate each particle as an electric dipole, resulting in an array of interacting dipoles. Under this approximation, the coupled-dipole approximation (CDA) provides an effective framework for describing the electromagnetic interactions within the array.

In this framework, an array of N nanoparticles is considered, where each particle is characterized by its polarizability α_i and position $\mathbf{r}_i$. The induced dipole moment $\mathbf{P}_i$ of the ith nanoparticle is related to the local electric field $\mathbf{E}_{\mathrm{loc},i}$ through its polarizability α_i as [79]

$$\mathbf{P}_i = \alpha_i \mathbf{E}_{\mathrm{loc},i}. \tag{2.26}$$

The local electric field at the position of the ith nanoparticle consists of the incident field and the retarded fields generated by all other dipoles in the array. For an incident plane wave with amplitude E_0 and wavenumber $k = 2\pi/\lambda$, the local field can be expressed as [79]

$$\mathbf{E}_{\mathrm{loc},i} = \mathbf{E}_{\mathrm{inc},i} - \sum_{\substack{j=1 \\ j\neq i}}^{N} \mathbf{A}_{ij} \cdot \mathbf{P}_j = E_0 \exp(i\mathbf{k} \cdot \mathbf{r}_i) - \sum_{\substack{j=1 \\ j\neq i}}^{N} \mathbf{A}_{ij} \cdot \mathbf{P}_j, \qquad i = 1, 2, \ldots, N, \tag{2.27}$$

where $\mathbf{A}_{ij}$ is the dipole interaction matrix describing the electromagnetic coupling between the ith and jth dipoles. The interaction matrix is given by [79]

$$\mathbf{A}_{ij} \cdot \mathbf{P}_j = k^2 \exp(ikr_{ij}) \frac{\mathbf{r}_{ij} \times (\mathbf{r}_{ij} \times \mathbf{P}_j)}{r_{ij}^3} + \exp(ikr_{ij}) (1 - ikr_{ij}) \frac{\left[r_{ij}^2 \mathbf{P}_j - 3\mathbf{r}_{ij} (\mathbf{r}_{ij} \cdot \mathbf{P}_j)\right]}{r_{ij}^5}, \tag{2.28}$$

where $\mathbf{r}_{ij}$ is the vector connecting dipoles i and j, and $r_{ij} = |\mathbf{r}_{ij}|$. The $3N$ coupled equations resulting from Eq. (2.27) can be solved to obtain the induced polarization vectors of all nanoparticles in the array.

For an infinite array of identical nanoparticles with polarizability α_s, the periodicity of the system allows the induced polarization of each particle to be described in terms of a dipole lattice sum S [79]:

$$P = \frac{E_0}{1/\alpha_s - S}, \tag{2.29}$$

where S accounts for the collective electromagnetic interactions between the dipoles in the array. For the specific case in which the incident wavevector is perpendicular to the plane of the array, the retarded dipole lattice sum can be expressed as

$$S = \sum_{j \neq i} \left[\frac{(1 - ikr_{ij}) (3\cos^2\theta_{ij} - 1) \exp(ikr_{ij})}{r_{ij}^3} + \frac{k^2 \sin^2\theta_{ij} \exp(ikr_{ij})}{r_{ij}} \right], \tag{2.30}$$

where θ_{ij} is the angle between the vector $\mathbf{r}_{ij}$ connecting the two dipoles and the direction of the induced polarization [79].

2.3.2 Surface lattice resonance

When the real parts of $1/\alpha_s$ and the dipole sum S are equal, the real part of the denominator in Eq. (2.29) vanishes, resulting in a significant enhancement of the induced polarization in each nanoparticle. This condition corresponds to the excitation of a surface lattice resonance (SLR). In this respect, the excitation of an SLR is analogous to that of a localized surface plasmon resonance (LSPR), where resonance occurs when the real part of the denominator

governing the particle polarization approaches zero. The key distinction between these two types of resonances is the presence of the dipole interaction term S in the SLR case. Unlike LSPRs, the dipole sum depends on the geometrical characteristics of the nanoparticle array, including the lattice period, providing additional degrees of freedom for tailoring the resonance properties. In particular, the linewidth of an SLR is determined by $\mathrm{Im}(1/\alpha_s - S)$, which can be reduced through partial cancellation between $\mathrm{Im}(1/\alpha_s)$ and $\mathrm{Im}(S)$. The dipole sum becomes significant only when a diffracted order propagates parallel to the array surface, explaining why SLRs are also referred to as diffraction-coupled localized plasmons. As a result, SLRs typically exhibit much narrower resonance linewidths and higher quality factors than the LSPRs of isolated nanoparticles. Figure 2.4 shows an example of the calculated transmission spectra reported by V. G. Kravets et al., highlighting the difference between the spectral features associated with localized surface plasmon resonance (LSPR) in isolated nanoparticles and surface lattice resonance (SLR) in periodic nanoparticle chain [73].

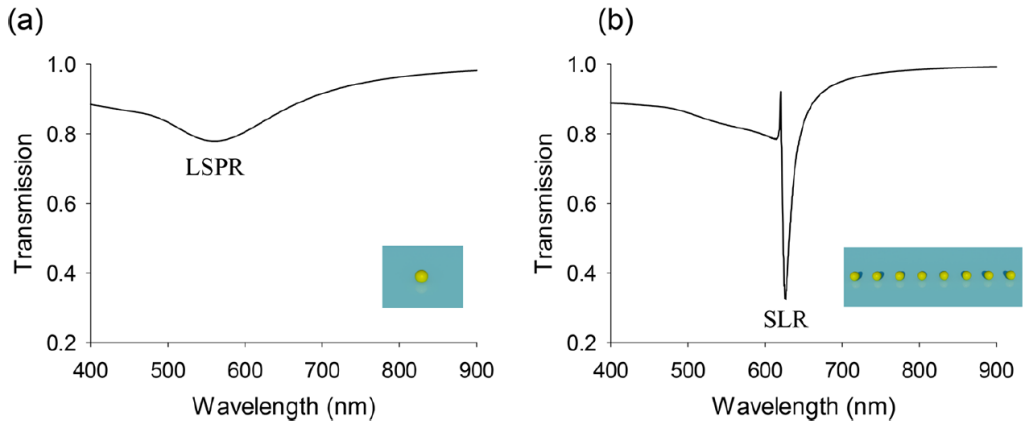

FIGURE 2.4: (a) Calculated transmission spectrum of a single gold sphere with a radius of 80 nm in an air environment. (b) Transmission response of a one-dimensional periodic chain formed by 1000 identical gold spheres, where the particles are separated by a period of 620 nm. From Ref. [73].

To demonstrate the influence of lattice periodicity on collective plasmonic resonances, Zou *et al.* analyzed periodic arrays of 400 nanoparticles using the coupled-dipole approximation [79]. The lattice period was varied between

200 and 700 nm, and both one-dimensional chains and two-dimensional hexagonal arrays were investigated. The optical response was characterized by the extinction efficiency, which is defined as the extinction cross section divided by the geometrical cross-sectional area of the particles. The resulting extinction spectra are presented in Fig 2.5. For reference, the extinction spectrum of a single isolated nanoparticle is also shown, highlighting the effect of interparticle coupling on the collective optical response [79].

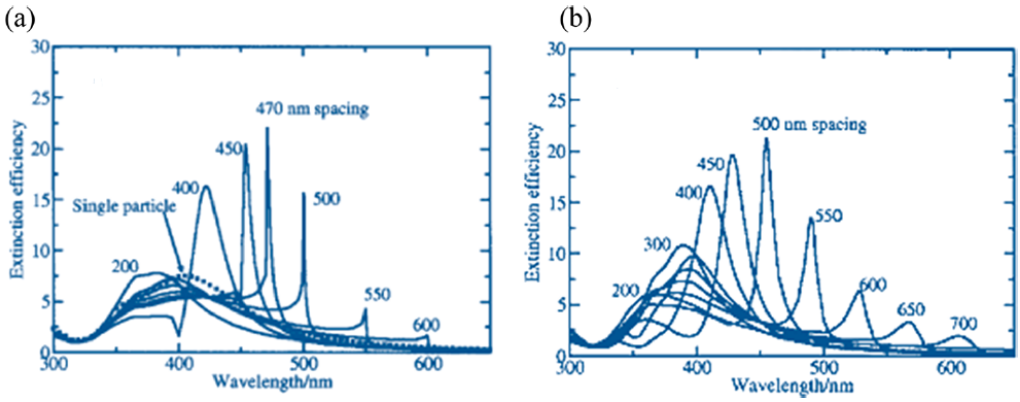

FIGURE 2.5: Extinction spectra obtained from simulations for silver nanoparticles with a diameter of 100 nm arranged in (a) a linear chain of 400 particles and (b) a hexagonally packed two-dimensional array containing 400 particles. The effect of varying the interparticle spacing is examined by presenting spectra for several array periods. In the 1D configuration, the incident polarization and propagation direction are both transverse to the chain axis. In the 2D array, illumination occurs normal to the array surface, with the electric field polarized parallel to the nanoparticle plane. From Ref. [79].

Zou et al. showed that increasing the interparticle spacing in nanoparticle arrays leads to a redshift and narrowing of the SLR compared with the single-particle LSPR. They found that 1D chains exhibit the sharpest resonances, achieving a quality factor above 100, while 2D arrays show similar trends with broader spectral features [79].

2.3.3 Fano resonance

A Fano resonance arises from the interference between a narrow discrete state and a broad continuum, resulting in a characteristic asymmetric peak-dip spectral profile. This phenomenon can be described using a system of two coupled oscillators, represented by the following matrix equation [104]:

$$\begin{pmatrix} \omega_1 - \omega - i\gamma_1 & g \\ g & \omega_2 - \omega - i\gamma_2 \end{pmatrix} \begin{pmatrix} x_1 \\ x_2 \end{pmatrix} = i \begin{pmatrix} f_1 \\ f_2 \end{pmatrix}, \tag{2.31}$$

where x_1 and x_2 denote the amplitudes of the two oscillators, ω_1 and ω_2 are their respective resonance frequencies, γ_1 and γ_2 represent their damping rates, and g denotes the coupling strength between the oscillators.

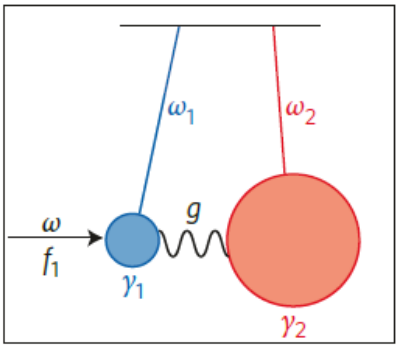

FIGURE 2.6: Schematic representation of two coupled damped oscillators, with a driving force f_1 applied to the first oscillator. From Ref. [104].

Figure 2.6 illustrates the mechanical analogue of a Fano resonance, in which the external force f_1 is applied only to the first mass [104].

In the weak-coupling regime, where $|g| \ll |\gamma_1|$ or $|g| \ll |\gamma_2|$, a Fano resonance can emerge when only one of the oscillators is directly excited, such that $f_1 \neq 0$ and $f_2 = 0$. In particular, when the oscillator with the larger damping rate is driven, the response near the resonance of the weakly damped oscillator can be expressed approximately as [104]

$$|x_1(\Omega)|^2 \approx |f_1|^2 \frac{\gamma_1^2}{(\omega_1-\omega_2)^2+\gamma_1^2}\frac{(\Omega+q)^2}{\Omega^2+1}, \tag{2.32}$$

$$\Omega = \left[\omega-\omega_2+\left(\frac{g^2}{\gamma_1}\right)\frac{\omega_1-\omega_2}{1+q^2}\right]\frac{\gamma_1(1+q^2)}{g^2}, \tag{2.33}$$

$$q = \cot\delta, \tag{2.34}$$

$$\delta = \arg\left(\omega_2-\omega_1+i\gamma_1\right)^{-1} \tag{2.35}$$

where $q = \cot\delta$ is the Fano asymmetry parameter and δ represents the phase difference between the two oscillators.

The value of the Fano parameter q determines the resulting spectral lineshape. In the limit $q \to \infty$, the response approaches a symmetric Lorentzian peak, whereas $q = 0$ produces a symmetric dip, commonly referred to as a Fano window. For intermediate values, such as $q \approx 1$ or $q \approx -1$, the spectrum exhibits an asymmetric profile characterized by a sharp peak adjacent to a pronounced dip. This interference-induced lineshape can lead to nearly complete suppression of scattering at one frequency while producing a strong scattering maximum at a nearby frequency. Figure 2.7, presented by Limonov et al., illustrates the relationship q given by equation (2.34), together with representative line shapes of the Fano response function appearing in equation (2.32) [104]. As the phase shift δ varies from 0 to π, the Fano parameter decreases from $+\infty$ to $-\infty$. For $|q| \to \infty$, the response approaches a symmetric Lorentzian peak. For finite nonzero values of q, an asymmetric peak–dip profile is obtained, and changing the sign of q reverses its orientation. The response vanishes at $\Omega = -q$, defining the Fano minimum, while $q = 0$ produces a symmetric dip centered at $\Omega = 0$ [104].

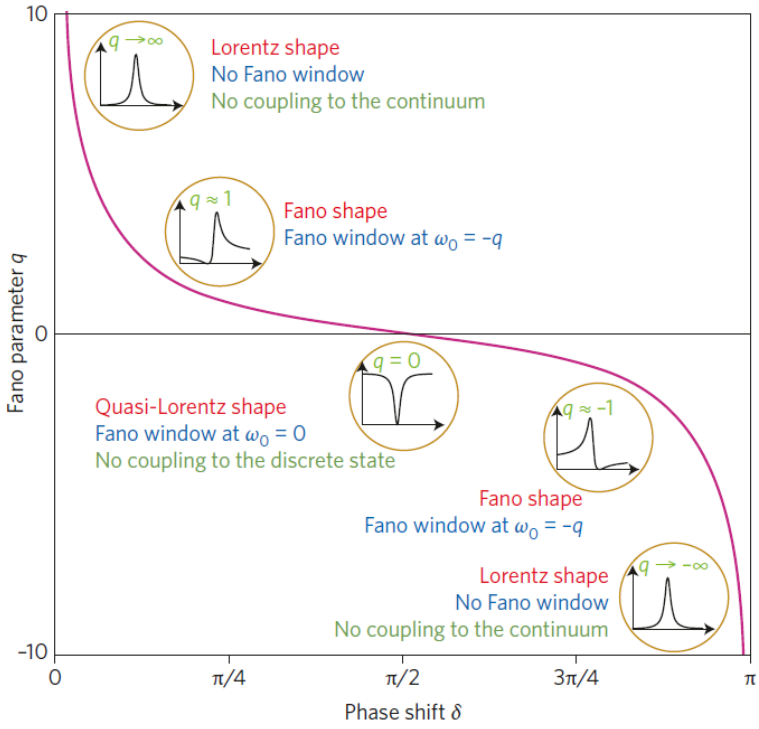

FIGURE 2.7: Fano parameter versus phase shift and the Fano response function. From Ref. [104].

2.4 Nonlinear Multipoles

In the previous sections, we demonstrated how a particle's optical response can be decomposed into its constituent multipolar moments and how the scattering cross-section of a perfect sphere can be calculated within this framework. This approach provided valuable insight into the linear optical properties of the material.

Beyond the linear regime, multipolar modes also play a crucial role in understanding nonlinear optical responses, which can be approached in two complementary ways. First, even within the conventional electric-dipole approximation commonly employed in nonlinear optics, the induced nonlinear polarization and dipole moment are expressed in terms of the local fundamental field. This local field, in turn, arises from the interference and superposition of different multipolar contributions (e.g., electric dipole, magnetic dipole, and electric quadrupole), thereby linking the nonlinear response to the multipolar composition of the excited modes [105]. Second, in a more

general framework, the nonlinear source need not be restricted to the electric dipole moment and its associated polarization current. Instead, higher-order contributions such as magnetic dipole and electric quadrupole moments, as well as even higher-order multipolar terms can act as nonlinear sources. When these higher-order nonlinear current sources are expanded, they can likewise be decomposed into electric dipole, magnetic dipole, electric quadrupole, and higher-order multipolar components [106].

This concept is elegantly demonstrated in the work of Kauranen et al., who used second-harmonic generation (SHG) to investigate the chiral properties of thin films [107]. They developed a general formalism for analyzing such chiral effects and applied it to review known phenomena while also introducing new effects. To achieve this, they assumed that the light-matter interaction Hamiltonian consists of electric dipole, magnetic dipole, and electric quadrupole contributions, as shown in Eq. (2.26) [107]:

$$H = -\mathbf{d}\cdot\mathbf{E} - \mathbf{m}\cdot\mathbf{B} - \mathbf{Q}:\nabla\mathbf{E} + \cdots \tag{2.36}$$

Based on this Hamiltonian, the nonlinear polarization, magnetization, and quadrupolarization at the second-harmonic frequency are expressed in terms of the electric field, magnetic field, and gradient of the electric field, as given by Eqs. (2.37)-(2.39) [107], [108].

$$\begin{aligned} P_i(2\omega) = {} & \chi^{eee}_{ijk}(2\omega,\omega,\omega)E_j(\omega)E_k(\omega) + \chi^{eem}_{ijk}(2\omega,\omega,\omega)E_j(\omega)B_k(\omega) + \\ & \chi^{eeQ}_{ijkl}(2\omega,\omega,\omega)E_j(\omega)\nabla_k E_l(\omega), \end{aligned} \tag{2.37}$$

$$M_i(2\omega) = \chi^{mee}_{ijk}(2\omega,\omega,\omega)E_j(\omega)E_k(\omega), \tag{2.38}$$

$$Q_{ij}(2\omega) = \chi^{Qee}_{ijkl}(2\omega,\omega,\omega)E_k(\omega)E_l(\omega). \tag{2.39}$$

Since the linear magnetic field and the gradient of the linear electric field are linearly related to the local electric field, and since the nonlinear sources are linearly related to the generated second-harmonic generation (SHG) field, the SHG electric field can be expressed as a quadratic expansion of the fundamental electric field, with different combinations of p- and s-polarized components:

$$E_i^{(2\omega)} = f_i E_p^2(\omega) + g_i E_s^2(\omega) + h_i E_p(\omega) E_s(\omega). \tag{2.40}$$

In this formalism, the nonlinear contributions of the different multipolar moments are effectively incorporated into the expansion coefficients f_i, g_i, and h_i, providing a unified description of the chiral nonlinear response [107].

2.5 Nonlinear metasurfaces

Accurate modeling of nonlinear processes in nanostructures is essential for the rational design and optimization of nonlinear photonic devices. Nonlinear phenomena, such as second-harmonic generation (SHG), strongly depend on local electromagnetic field distributions, nanostructure geometry, symmetry properties, and the contribution of higher-order multipolar modes. Several theoretical approaches have been developed to describe the nonlinear response of nanostructures, including Miller's rule, the nonlinear effective susceptibility approach, and the hydrodynamic model [109], [110], [111].

Based on Miller's rule, the second-order nonlinear susceptibility can be approximated as the product of Miller's coefficient and the linear susceptibilities evaluated at the fundamental and second-harmonic frequencies [112], [113]. This empirical relationship can also be understood within the classical anharmonic-oscillator model [70]. Although useful for estimating nonlinear susceptibilities, Miller's rule has important limitations when applied to SHG from plasmonic nanostructures. In particular, it may not accurately reproduce the effects of complex geometries and strong near-field coupling. For example, it fails to describe the dependence of the SHG response on the

morphology of split-ring resonators and may therefore predict an incorrect geometry for maximizing SHG [109].

At first glance, the different applicability of the model to THG and SHG may appear contradictory. This discrepancy arises from the distinct selection rules governing second- and third-order nonlinear optical processes. In plasmonic nanostructures, SHG can be strongly influenced by higher-order multipolar contributions, including electric quadrupole, electric octupole, and magnetic dipole modes, which are not captured by Miller's rule. Consequently, this approximation is only valid for specific situations, such as nanostructures exhibiting resonant behavior at the second-harmonic wavelength while lacking a resonance at the fundamental wavelength [109].

To provide a clearer demonstration of these limitations, Butet and Martin investigated the nonlinear response of gold split-ring resonators and compared the predictions of Miller's rule with results obtained from a surface integral formulation [109]. According to Miller's rule, the SHG intensity can be estimated from the linear scattering response at the fundamental and second-harmonic frequencies as [109]

$$I_{\mathrm{SHG}} \propto I^2_{\mathrm{Scat},x}(\omega), I_{\mathrm{Scat},y}(2\omega), \tag{2.41}$$

where the subscripts indicate the polarization directions at the fundamental and second-harmonic frequencies. Their results demonstrated that, although Miller's rule can successfully predict the SHG response in certain cases, it cannot be generally applied to arbitrary plasmonic nanostructures with complex geometries [109].

The nonlinear effective susceptibility method is a linear–nonlinear hybrid approach in which the nonlinear polarization associated with a specific nonlinear process is first calculated [109]. The corresponding nonlinear current density is then obtained from the time derivative of the nonlinear polarization. Finally, using nonlinear scattering theory, which will be discussed in

detail in the following sections, the generated nonlinear far-field emission is calculated through the overlap integral between the linear near-field distribution at the fundamental frequency and the field generated by a test dipole at the harmonic frequency.

For the case of second-harmonic generation, the generated SH electric field can be expressed as a surface integral over the nanostructure surface as

$$E_{\mathrm{SHG}} \propto \iint \chi^{\mathrm{surf}}_{nnn} E_n^2(\omega) E_n(2\omega) dS, \tag{2.42}$$

where $E_n(\omega)$ and $E_n(2\omega)$ represent the normal components of the electric field at the fundamental and second-harmonic frequencies, respectively, and $\chi^{\mathrm{surf}}_{nnn}$ is the normal component of the surface nonlinear susceptibility tensor [109].

Although this method has been successfully applied to calculate SHG from non-centrosymmetric plasmonic nanostructures, its applicability to centrosymmetric nanoparticles is more limited because it cannot fully account for the multipolar nature of the SH emission induced by retardation effects.

Despite these limitations, the nonlinear effective susceptibility method offers a simple implementation that can be realized using commercially available electromagnetic solvers. Therefore, it provides a practical alternative to full-wave nonlinear simulations. However, it must be applied with caution when analyzing nanostructures with complex multipolar responses.

The hydrodynamic model provides a more comprehensive approach for describing the nonlinear response of plasmonic nanostructures. In this framework, the conduction electrons are treated as a pressure-driven interacting electron fluid governed by the nonlinear Euler equation coupled with the continuity and Maxwell equations. Consequently, the nonlinear response is

obtained by solving a coupled system of nonlinear partial differential equations for the electron velocity and electromagnetic fields throughout the nanostructure volume, rather than relying on a surface integral based on an effective nonlinear susceptibility [110], [114].

Although this approach involves significantly greater computational complexity, it offers several important advantages. First, the hydrodynamic model naturally accounts for both surface and bulk nonlinear sources, including higher-order multipolar contributions such as electric quadrupole and magnetic dipole modes. Second, because the governing equations are solved numerically over the entire nanostructure volume, the model can be applied to complex geometries without requiring simplified assumptions about the shape [110].

By directly modeling the dynamics of conduction electrons, the hydrodynamic model captures the underlying physical mechanisms responsible for nonlinear generation. Therefore, it provides a more complete and predictive description of second-harmonic generation in plasmonic nanostructures. The details of this model are presented in the following section.

2.5.1 Hydrodynamic Model

The hydrodynamic model describes the collective motion of free electrons under the influence of an external electromagnetic field through the coupled continuity and Euler equations [110], [114], [115]. The continuity equation is given by

$$\nabla \cdot \mathbf{J} + e\frac{\partial n}{\partial t} = 0, \tag{2.43}$$

where the particle current density is defined as $\mathbf{J} = en\mathbf{v}$, and $\mathbf{v}$ represents the velocity distribution of the electron fluid. The corresponding Euler equation is expressed as

$$\frac{\partial \mathbf{v}}{\partial t} + (\mathbf{v} \cdot \nabla)\mathbf{v} + \gamma \mathbf{v} = \frac{e}{m_e^*}(\mathbf{E} + \mathbf{v} \times \mathbf{B}) - \frac{\beta^2}{n}\nabla n, \tag{2.44}$$

where e is the electron charge, γ is the electron collision rate, β is a constant related to the Thomas–Fermi pressure, and $\mathbf{E}$ and $\mathbf{B}$ denote the external electric and magnetic fields, respectively [110], [114], [115].

The convective acceleration term $(\mathbf{v}\cdot\nabla)\mathbf{v}$ gives rise to nonlinear polarizability, the damping term $\gamma\mathbf{v}$ accounts for electron collisions, and the Lorentz-force term $\mathbf{v}\times\mathbf{B}$ couples the hydrodynamic and Maxwell's equations, leading to nonlocal nonlinear effects. The last term, proportional to ∇n, represents the electron gas pressure arising from electron-electron repulsion described by the Thomas–Fermi model [110], [114], [115].

By combining the continuity and Euler equations and expanding all fields perturbatively under time-harmonic excitation, the first- and second-order polarizations $\mathbf{P}_1$ and $\mathbf{P}_2$ satisfy the following inhomogeneous equations [110], [114], [115]:

$$\beta^2\nabla(\nabla\cdot\mathbf{P}_1)+(\omega^2+i\omega\gamma)\mathbf{P}_1=\frac{ne^2}{m_e^*}\mathbf{E}_1, \tag{2.45}$$

$$\beta^2\nabla(\nabla\cdot\mathbf{P}_2)+(\omega^2+i\omega\gamma)\mathbf{P}_2=\frac{ne^2}{m_e^*}\mathbf{E}_2+\mathbf{S}_{\mathrm{NL}}, \tag{2.46}$$

where $\mathbf{S}_{\mathrm{NL}}$ is the nonlinear source term responsible for second-order effects, expressed as

$$\mathbf{S}_{\mathrm{NL}}=-\frac{e}{m_e^*}\left[\mathbf{E}_1(\nabla\cdot\mathbf{P}_1)+\frac{\omega e}{m_e^*}(\mathbf{P}_1\times\mathbf{B}_1)-\frac{\omega^2}{ne}(\nabla\cdot\mathbf{P}_1)\mathbf{P}_1\right]. \tag{2.47}$$

Under the undepleted pump approximation, the first- and second-order polarizations can be written as

$$\mathbf{P}_1=-\frac{ne^2}{m_e^*(\omega+i\gamma)}\mathbf{E}_1, \tag{2.48}$$

$$\mathbf{P}_2 = \frac{ne^2}{m_e^*(2\omega + i\gamma)}\mathbf{E}_2 + \mathbf{P}_{\mathrm{NL}}, \tag{2.49}$$

where $\mathbf{P}_{\mathrm{NL}}$ denotes the nonlinear polarization term, expressed as

$$\begin{aligned}\mathbf{P}_{\mathrm{NL}} = \frac{ne^3}{m_e^{*2}(2\omega + i\gamma)(\omega + i\gamma)} \Bigg[\frac{1}{\omega}\mathbf{E}_1(\nabla \cdot \mathbf{E}_1) + i\mu\, \mathbf{E}_1 \times \mathbf{H}_1 \\ + \frac{1}{(\omega + i\gamma)}(\nabla \cdot \mathbf{E}_1)\mathbf{E}_1.\end{aligned} \tag{2.50}$$

The corresponding nonlinear current density, obtained from the time derivative of $\mathbf{P}_{\mathrm{NL}}$, can be written as

$$\mathbf{J}_{\mathrm{NL}} = -i2\omega\mathbf{P}_{\mathrm{NL}}. \tag{2.51}$$

Here, the first term in $\mathbf{P}_{\mathrm{NL}}$ represents the electrostatic (Coulomb) contribution, the second term corresponds to the magnetic Lorentz force, and the third term originates from the convective nonlocality of the electron motion. These components collectively describe the second-order nonlinear response of the free-electron plasma, providing a comprehensive framework for modeling second-harmonic generation (SHG) and other nonlinear optical effects beyond the Drude model [110], [114], [115].

2.5.2 Nonlinear Scattering Theory

In this model, we use Lorentz reciprocity to determine the nonlinear emission from a nanostructure, which can be a single nanoantenna or a metasurface. The approach relates the nonlinear polarization induced by the incident field to the emitted nonlinear radiation, by exploiting the reciprocity relation between two equivalent electromagnetic systems. Figure 2.8 shows a schematic representation of the nonlinear scattering model and its reciprocal excitation configuration [116].

We consider two current density sources, $\mathbf{J}_1$ and $\mathbf{J}_2$, which generate electric fields $\mathbf{E}_1$ and $\mathbf{E}_2$ in a reciprocal and linear medium. In our case, $\mathbf{J}_1$ corresponds to the nonlinear current density $\mathbf{J}_{\mathrm{NL}}$ induced by the incident pump

field at frequency ω, obtained from the hydrodynamic model. This nonlinear source produces the emitted nonlinear field $\mathbf{E}_1$ in the far field. At the same time, $\mathbf{J}_2$ represents a test current density located at the detector position, modeled as a dipole of length l and polarization direction $\hat{\mathbf{j}}$ [116].

For a reciprocal medium the Lorentz reciprocity theorem gives

$$\int_V \mathbf{J}_2(\mathbf{r},\omega)\cdot\mathbf{E}_1(\mathbf{r},\omega)\,dV = \int_V \mathbf{J}_1(\mathbf{r},\omega)\cdot\mathbf{E}_2(\mathbf{r},\omega)\,dV. \tag{2.52}$$

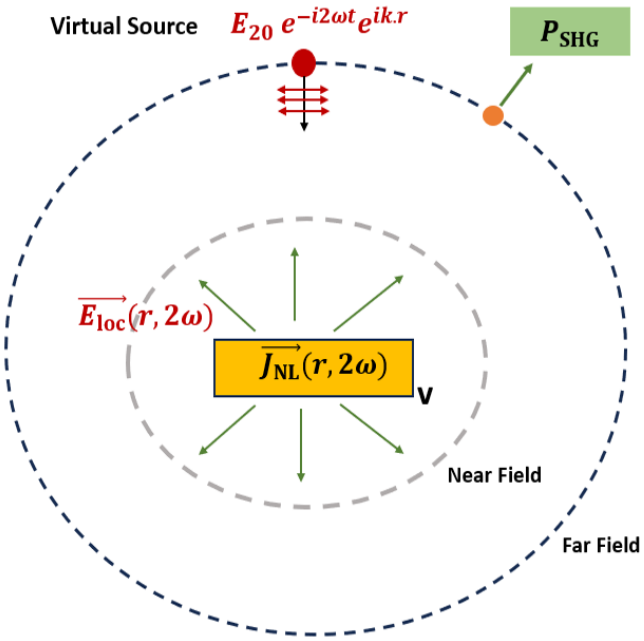

FIGURE 2.8: Lorentz–reciprocity theory application for SHG from a resonant plasmonic meta-atom.

The first current density is associated with the nonlinear polarization induced in the nanostructure,

$$\mathbf{J}_1(\mathbf{r},\omega) = \frac{\partial \mathbf{P}_{\mathrm{NL}}(\mathbf{r},\omega)}{\partial t} = -i\omega\,\mathbf{P}_{\mathrm{NL}}(\mathbf{r},\omega) \tag{2.53}$$

while the second current density corresponds to a localized test dipole at the detector,

$$\mathbf{J}_2(\mathbf{r},\omega) = J_0\,\delta(\mathbf{r}-\mathbf{r}_2)\,e^{i\omega t}\,\hat{\mathbf{j}}. \tag{2.54}$$

Substituting Eqs. (2.53) and (2.54) into Eq. (2.52) gives

$$\int_V \mathbf{E}_1(\mathbf{r},\omega)\cdot J_0\,\delta(\mathbf{r}-\mathbf{r}_2)e^{i\omega t}\hat{\mathbf{j}}\,dV = \int_V i\omega\,\mathbf{P}_{\mathrm{NL}}(\mathbf{r},\omega)\cdot\mathbf{E}_2(\mathbf{r},\omega)\,dV. \tag{2.55}$$

The left-hand side of equation (2.55) represents the projection of the emitted nonlinear field onto the detector's polarization axis,

$$\mathbf{E}_1(\mathbf{r}_2,\omega)\cdot\hat{\mathbf{j}} = \frac{i\omega e^{-i\omega t}}{J_0 l}\int_V \mathbf{P}_{\mathrm{NL}}(\mathbf{r},\omega)\cdot\mathbf{E}_2(\mathbf{r},\omega)\,dV. \tag{2.56}$$

At the second-harmonic frequency 2ω, the nonlinear polarization is given by:

$$\mathbf{P}_{2\omega}(\mathbf{r}) = \varepsilon_0\boldsymbol{\chi}^{(2)}(\mathbf{r}) : \mathbf{E}_\omega(\mathbf{r})\mathbf{E}_\omega(\mathbf{r}), \tag{2.57}$$

and the corresponding nonlinear current density is

$$\mathbf{J}_{2\omega}(\mathbf{r}) = -i2\omega\varepsilon_0\boldsymbol{\chi}^{(2)}(\mathbf{r}) : \mathbf{E}_\omega(\mathbf{r})\mathbf{E}_\omega(\mathbf{r}). \tag{2.58}$$

Using the reciprocity relation and taking $\mathbf{E}_2(\mathbf{r}) = \mathbf{E}^{\mathrm{test}}_{2\omega}(\mathbf{r})$ as the local field distribution inside the structure produced by a plane wave at 2ω, the radiated SH field in the far field can be written as

$$E^{\mathrm{FF}}_{2\omega} = \frac{-i2\omega}{c_0 E^{\mathrm{inc}}_{2\omega} S_{\mathrm{unit}}}\int_{V_{\mathrm{unit}}} \varepsilon_0\chi^{(2)}_{\mathrm{eff}}(\mathbf{r})\,[E_{\omega,z}(\mathbf{r})]^2 E_{2\omega,z}(\mathbf{r})\,dV, \tag{2.59}$$

and the corresponding SHG conversion efficiency, defined as the ratio of radiated SH power to the incident pump power, is

$$\eta_{\mathrm{SHG}} = \left|\frac{i2\omega}{c_0 E^{\mathrm{inc}}_{2\omega} E^{\mathrm{inc}}_{\omega} S_{\mathrm{unit}}}\int_{V_{\mathrm{unit}}} \varepsilon_0\chi^{(2)}_{\mathrm{eff}}(\mathbf{r})\,[E_{\omega,z}(\mathbf{r})]^2 E_{2\omega,z}(\mathbf{r})\,dV\right|^2. \tag{2.60}$$

If the field distributions are nearly uniform within the nonlinear region, the integral can be approximated by constant local field amplitudes, giving a simple analytical expression for the SHG efficiency [116].

2.6 THz and infrared meta-filters

This section provides the theoretical background for multilayer complementary antireflective metamaterials with operating wavelengths in the THz and infrared regions. First, we examine how light interacts with complementary structures by discussing Babinet's principle in optics. We then explain the physical mechanisms underlying the antireflective behavior, including Fabry–Pérot destructive interference and impedance matching. Finally, we present several examples to illustrate these concepts more clearly.

2.6.1 Babinet's Principle

Babinet's principle describes the relationship between a structure and its complementary counterpart, obtained by interchanging the transparent and opaque regions. It states that the diffraction patterns produced by these two complementary structures are directly related and that their combined electromagnetic response is equivalent to the incident field [117].

If the aperture function of the original structure is denoted by $f(u,v)$, the corresponding complementary function $\bar{f}(u,v)$ satisfies

$$f(u,v) + \bar{f}(u,v) = 1, \tag{2.61}$$

indicating that regions transmitting light in one structure block it in the other, and vice versa.

The diffracted fields generated by the original and complementary structures satisfy

$$\psi + \bar{\psi} = \psi_0 \cos(\omega t - kR - \phi), \tag{2.62}$$

where ψ and $\bar{\psi}$ denote the fields diffracted by the original and complementary structures, respectively, and $\psi_0 \cos(\omega t - kR - \phi)$ represents the incident wave. Therefore, the superposition of the two scattered fields reconstructs the incident field. This principle provides the theoretical basis for understanding the electromagnetic response of complementary metallic structures and is widely used in the analysis and design of metasurfaces [96], [117].

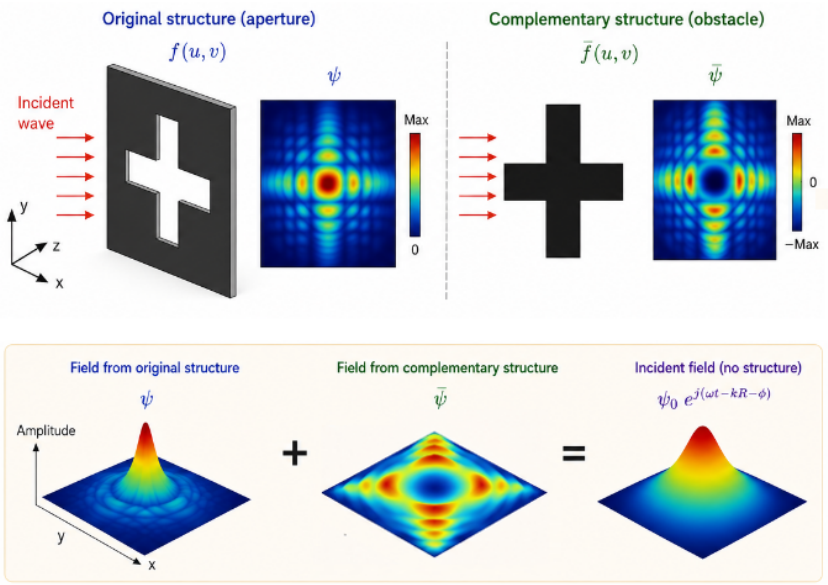

FIGURE 2.9: Complementary structures illustrating Babinet's principle.

Figure 2.9 shows the configurations of the complementary structures and the three dimensional field profiles transmitted through each structure [117].

2.6.2 multilayer complementary metasurfaces

Inspired by this physical rule, metasurfaces have been designed consisting of unit cells with stacked complementary layers separated by a dielectric spacer. Based on Babinet's principle, these types of structures are particularly well-suited for designing bandpass filters. Since layers exhibit complementary electromagnetic responses—one blocking certain wavelengths

while the other transmits them—their combination enables selective transmission within a desired passband while suppressing out-of-band frequencies. For metallic complementary layers, one layer typically behaves as an inductive mesh (low-pass filter), while the other acts as a capacitive mesh (high-pass filter). The combination of these two complementary responses results in a bandpass filtering behavior. Here, we provide a few examples of such structures [97], [99].

One interpretation of the antireflection functionality of these structures is based on Fabry–Pérot resonances. The two complementary metallic layers, separated by a dielectric spacer, form a Fabry–Pérot resonator with an effective refractive index n_{eff}. When the structure is illuminated, part of the incident light is reflected from the first layer, while the remainder enters the resonator and reaches the second layer, where it is partially transmitted and partially reflected back. This process results in waves propagating back and forth within the cavity. If the reflected waves destructively interfere over a certain frequency range, the overall reflectance is suppressed. Meanwhile, constructive interference of the transmitted waves leads to high transmission within the desired passband, producing the antireflection response [97], [99], [100], [118].

For example, Karen Simonyan et al. designed and theoretically studied a bandpass antireflection meta-filter. Their design consists of a silicon cylindrical ring coated with gold on a silicon substrate, while the substrate is covered by a gold cylinder, which serves as the complementary layer [99]. The configuration of this geometry is depicted in Fig. 2.10. The square-shaped transmission spectrum obtained from this design demonstrates a clear bandpass response within the targeted wavelength range [99].

They also provided a step-by-step analysis to explain how partial-wave interference leads to the observed transmission spectrum [99]. First, the Si–air ring layer was represented by a homogeneous slab whose permittivity, ε_{eff}, was determined iteratively by matching its reflection and transmission magnitudes to those of the original patterned layer. The corresponding refractive index was then obtained as $n_{\text{eff}} = \sqrt{\varepsilon_{\text{eff}}}$. Next, assuming illumination from

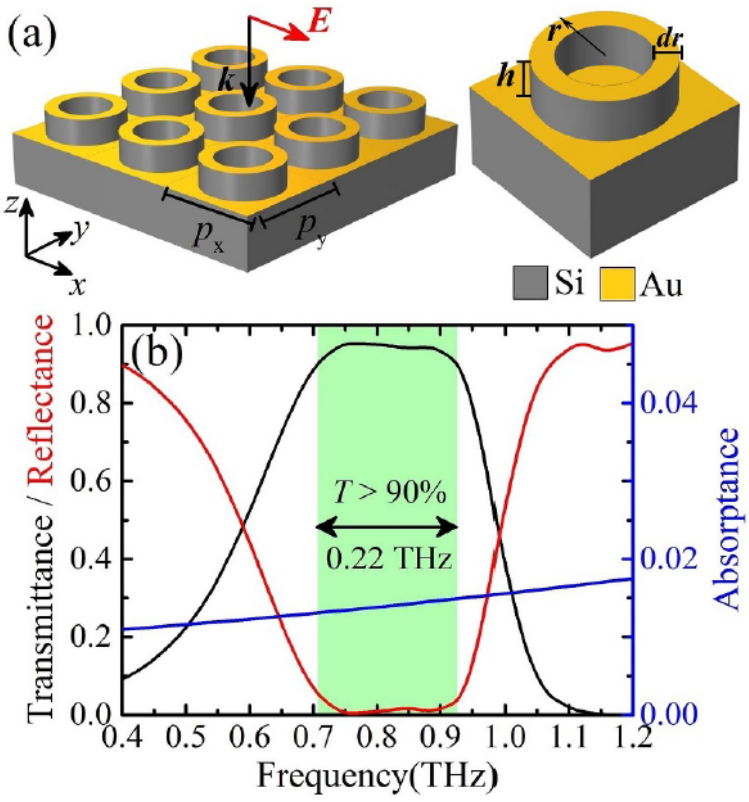

FIGURE 2.10: (a) 3D schematic of the simulated structure. (b) Transmittance (black) and reflectance (red) spectra shown on the left axis, and the absorptance spectrum shown on the right axis, for the metafilter with optimized geometrical parameters: $p_x = p_y = 77$ μm, $h = 25$ μm, $r = 30$ μm, and $dr = 10$ μm. From Ref. [99].

the top, the total reflection coefficient was expressed in terms of the reflection coefficients and phases at the interfaces and the propagation phase through the structure [99]:

$$\tilde{r} = \frac{r_{21}\exp(i\varphi_{12}) - r_{23}\exp\left[i\left(\varphi_{12}+\varphi_{21}+\varphi_{23}+2\beta\right)\right]}{1 - r_{21}r_{23}\exp\left[i\left(\varphi_{21}+\varphi_{23}+2\beta\right)\right]} \tag{2.63}$$

Now, to achieve zero reflection, two conditions must be satisfied: (i) $r_{21} = r_{23}$ and (ii) $\varphi_{21} + \varphi_{23} + \beta = 2\pi m$, where m is an integer. These conditions correspond to destructive interference of the reflected waves and, consequently, constructive interference in transmission, leading to a maximum transmission coefficient. Since the absorptance of the structure is negligible, the transmittance can be calculated from [99]

$$T(f) = 1 - \left|\tilde{r}(f)\right|^2. \tag{2.64}$$

Figure 2.11(c) shows the transmittance calculated using this expression, which agrees well with the numerical simulation. Figure 2.11(b) illustrates the corresponding effective structure, while Fig. 2.11(d) presents the magnitudes and phases of the reflection coefficients as functions of wavelength. By comparing Figs. 2.11(c) and 2.11(d), it can be seen that the high-transmission passband occurs over the spectral range in which the two conditions above are approximately satisfied, confirming the validity of the above conditions [99].

Another method for interpreting the antireflection behavior is based on impedance matching. Since the incident wave propagates from air, which has an impedance of approximately $Z_0 \approx 377\,\Omega$, the reflection vanishes when the effective impedance of the structure matches that of air over a specific wavelength range. In this case, the structure becomes transparent. Figure 2.11(a) shows the relative impedance of the corresponding structure, calculated using the following equation [99]:

$$Z_r = \frac{Z}{Z_0} = \pm\sqrt{\frac{(1+S_{11})^2 - S_{21}^2}{(1-S_{11})^2 - S_{21}^2}} \tag{2.65}$$

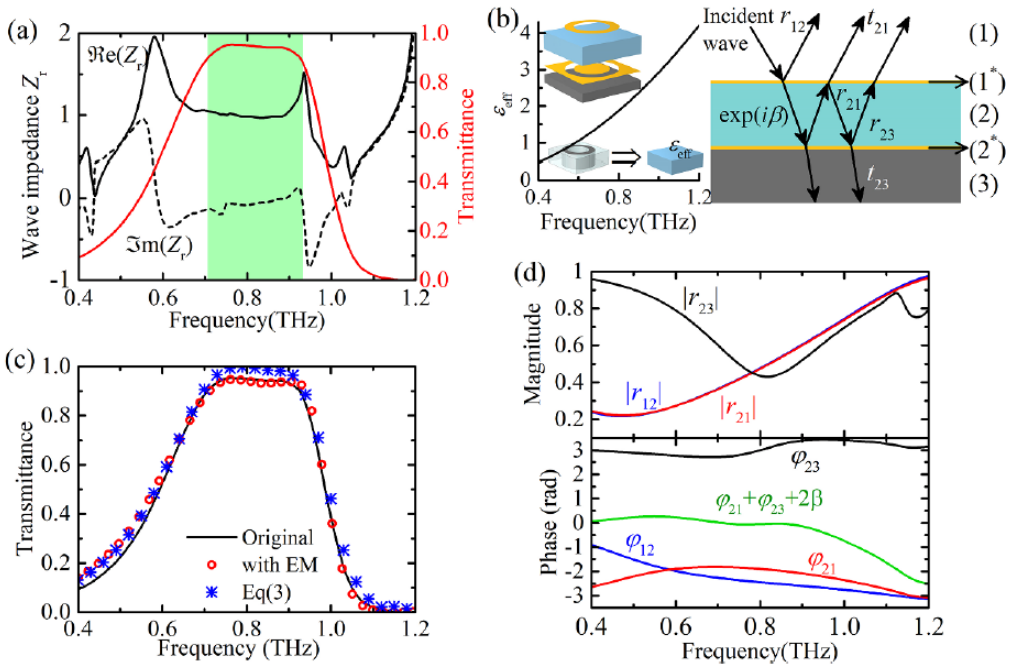

FIGURE 2.11: (a) Relative impedance of the structure compared with the transmission spectrum. (b) Configurations of the original and the effective structure, in which the Si–air ring layer is replaced by a homogeneous dielectric slab. (c) Transmission spectra obtained from the numerical simulation and calculated using Eq. (2.4). (d) Magnitudes and phases of the reflection coefficients at the interfaces between the first and second regions and between the second and third regions. From Ref. [99].

As can be seen in the figure, in the spectral range where the relative impedance Z_r approaches unity corresponding to impedance matching with air—the structure exhibits high transmission and negligible reflection.

In another study, Beheshti Asl et al. employed a similar approach to design an antireflection bandpass filter operating in the low-THz frequency range [97]. The proposed structure consisted of cylindrical dielectric elements combined with two complementary gold layers, as illustrated in Figure 2.12. The corresponding transmission spectrum is also presented in the same figure. By varying the radius of the cylindrical elements, the authors were able to shift the central wavelength of the passband, demonstrating the tunability of the filtering response through geometrical parameters [97].

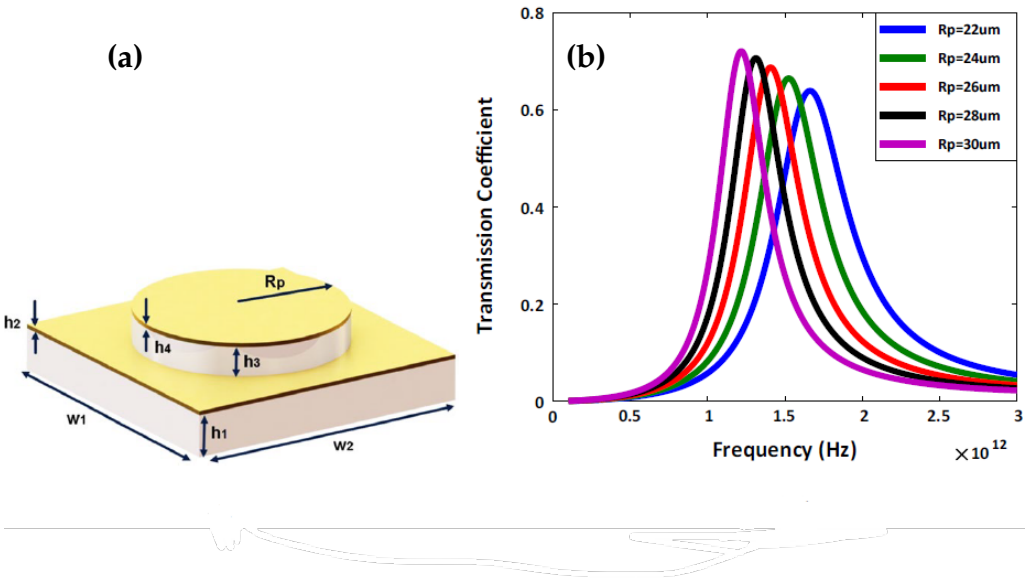

FIGURE 2.12: (a) Unit-cell configuration of the proposed filter. (b) Transmittance spectra of the corresponding structure for different cylinder radii, with the optimized geometrical parameters $w_1 = w_2 = 2.4R_p$, $h_1 = 10$ μm, $h_2 = 0.2$ μm, $h_3 = 8$ μm, and $h_4 = 0.2$ μm. From Ref. [97].

To introduce an additional degree of freedom, the authors further investigated the interaction between neighboring particles within each unit cell. Rather than using a single resonant particle, unit cells containing two, three, and four particles were considered. Since each individual particle supports

its own resonance, incorporating multiple particles gives rise to multiple resonant features in the transmission spectrum. By varying the separation between the particles, the coupling between these resonances can be controlled, leading to their hybridization and interference in the frequency domain. Figure 2.13 shows the configuration and transmission spectrum of a unit cell containing two particles, where two distinct resonances can be clearly observed [97].

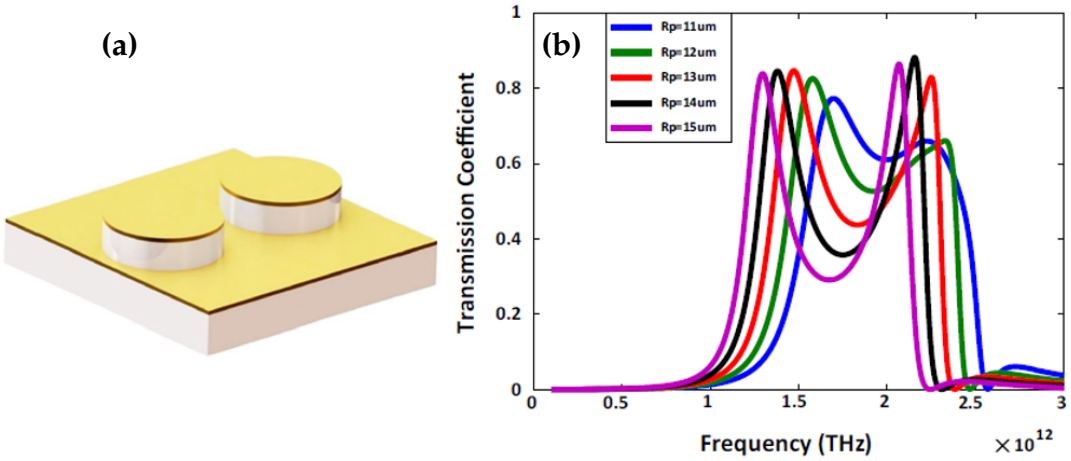

FIGURE 2.13: (a) Unit-cell configuration of the proposed filter. (b) Transmittance spectra of the corresponding structure for different cylinder radii, with the optimized geometrical parameters $w_1 = w_2 = 4.8R_p$, $h_1 = 10$ μm, $h_2 = 0.2$ μm, $h_3 = 8$ μm, and $h_4 = 0.2$ μm.

2.7 Computational Methods

The optical response of the nano- and microstructures investigated in this thesis is modeled using full-wave electromagnetic simulations. The studied structures mainly consist of periodic arrays of meta-atoms composed of dielectric, metallic, or hybrid materials. Throughout these projects, silicon (Si) and silicon dioxide (SiO_2) are used as dielectric materials, while gold (Au) and aluminum (Al) are used as plasmonic materials. The optical properties of all materials are described using experimentally measured, wavelength-dependent refractive index data, thereby accounting for both material dispersion and optical losses.

Since most of the investigated structures are periodic in the x- and y-directions, periodic boundary conditions (PBCs) are applied along these directions to represent an infinitely periodic array. Along the z-direction, which is generally the propagation direction of the incident electromagnetic wave or the surface-normal direction for oblique illumination, perfectly matched layers (PMLs) are placed at the upper and lower boundaries of the computational domain. These layers absorb undesired reflections from the simulation boundaries.

Two numerical methods are employed throughout this thesis depending on the simulation requirements: the finite-difference time-domain (FDTD) method and the finite element method (FEM). The FDTD method solves Maxwell's equations in the time domain using a structured Cartesian grid, making it well suited for broadband electromagnetic simulations. In contrast, the FEM solves Maxwell's equations by discretizing the computational domain into an unstructured finite-element mesh, typically in the frequency domain, providing greater flexibility for modeling complex geometries. The FDTD simulations are performed using Lumerical FDTD Solutions, while the FEM simulations are carried out using COMSOL Multiphysics. In this thesis, Lumerical is used to investigate the linear optical response of the studied structures, while COMSOL is employed to perform both linear and nonlinear electromagnetic simulations.

The nonlinear simulations in COMSOL are carried out in two consecutive frequency-domain studies. In the first study, the fundamental wavelength electromagnetic field is calculated throughout the structure. The resulting local field is then used to evaluate the nonlinear current density based on the hydrodynamic model. In the second study, this nonlinear current density is introduced as the excitation source to calculate the generated second-harmonic field, from which the nonlinear emitted power and intensity distributions are obtained.

2.8 Conclusion

In this chapter, the theoretical foundations of the linear and nonlinear optical response of metasurfaces are presented. We begin by reviewing the optical response of an isolated spherical particle through Mie theory and the corresponding multipole decomposition. These concepts provide the basis for understanding the scattering of the incident electromagnetic field and the contributions of different multipolar modes to the optical response.

The discussion is then extended to the nonlinear regime, where the multipole decomposition framework is applied to nonlinear optical processes, such as second-harmonic generation, to describe the contributions of different multipolar modes to the nonlinear emission. Next, the effects of electromagnetic interactions between neighboring particles are investigated, with particular emphasis on collective phenomena such as lattice resonances and Fano resonances.

The chapter then introduces the theoretical modeling of nonlinear metasurfaces by describing the nonlinear source terms and comparing the different approaches used to model the nonlinear response. This is followed by a discussion of nonlinear scattering theory, which provides the framework for calculating the far-field nonlinear radiation generated by the metasurfaces. Finally, the computational methods employed throughout this thesis are presented, including the numerical techniques used to model both the linear and nonlinear optical responses of the investigated structures.

Overall, this chapter establishes the theoretical and computational framework required to understand, analyze, and model the linear and nonlinear optical properties of the metasurfaces investigated in this thesis.

Chapter 3

THz spectral meta-filter

3.1 Introduction

In this chapter, a collaborative project between our research group and the Iridian Spectral Technologies company is presented. A metasurface-based filter composed of periodically arranged metallized silicon (Si) crosses on a substrate covered by a complementary thin metallic layer is theoretically and numerically investigated as a band-pass filter for terahertz (THz), mid-infrared, and far-infrared radiation. A three-dimensional schematic of the proposed filter is shown in Figure 3.1. The step-by-step design procedure and the physical mechanisms underlying the response are discussed. An efficient antireflection band, with reflectance below 10% over the corresponding spectral range, is achieved. We also showed that the operating band can be shifted to different wavelength ranges by appropriately adjusting the geometrical parameters. Finally, we demonstrated that the proposed filter exhibits a polarization-insensitive response, owing to the two orthogonal arms of the cross-shaped elements.

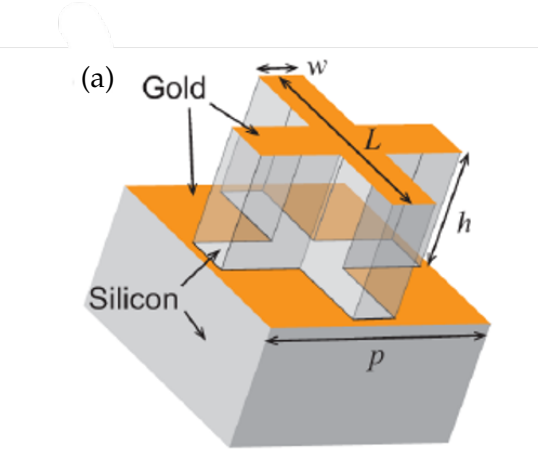

FIGURE 3.1: Three-dimensional schematic of the proposed meta-filter, showing its constituent layers and main geometrical parameters: cross-arm length L, width w, resonator thickness h, and array periodicity p.

3.2 Methodology

To obtain an initial set of geometrical parameters that produces resonances within the desired spectral range, simplified analytical models were used before performing the full-wave optimization. For the dielectric microbar, a first-order estimate can be obtained from the Mie-resonance condition discussed in the previous chapters. For example, the approximate magnetic-dipole resonance of a dielectric sphere satisfies [50]

$$2Rn \approx \lambda_{\text{res}}, \tag{3.1}$$

where R and n are the radius and refractive index of the particle, respectively. Although the considered structure is a rectangular bar rather than a sphere, this relation provides a useful initial estimate [50].

Resonances associated with propagation along the bar can also be approximately described using a Fabry-Pérot model [119]. The corresponding resonance condition is [119]

$$2k_{\text{mode}}L_{\text{eff}} = 2\pi m, \tag{3.2}$$

where k_{mode} is the propagation constant of the supported mode, L_{eff} is the effective resonator length, and m is a positive integer representing the resonance order. For the fundamental longitudinal mode, $m = 1$ [119].

Since the metallic layers can be approximately interpreted as capacitive and inductive filters, their effective circuit parameters can be estimated from their geometrical dimensions. For an elongated metallic nanoprism, the capacitance and inductance can be approximated as [120]

$$C = 2\pi\varepsilon_0\varepsilon_r\frac{h}{2}, \tag{3.3}$$

and

$$L = \frac{\mu_0 l}{2\pi}\ln\left(\frac{4l}{h}\right) + \frac{\mu_0 l c_0^2}{\omega_p^2 wh}, \tag{3.4}$$

where the two terms represent the self- and kinetic inductances, respectively. Here, l, w, and h are the bar length, width, and thickness, while ε_r and ω_p denote the relative permittivity of the surrounding medium and the plasma frequency of the metal, respectively. The resistance of the bar is approximated by [120]

$$R = \rho\frac{l}{wh}, \tag{3.5}$$

where ρ is the metal resistivity. The approximate capacitive and inductive cutoff frequencies are then given by

$$f_{c,C} = \frac{1}{2\pi RC}, \qquad f_{c,L} = \frac{R}{2\pi L}. \tag{3.6}$$

When the capacitive and inductive layers are combined, the approximate band-pass resonance frequency becomes [120]

$$f_0 = \frac{1}{2\pi\sqrt{LC}}, \tag{3.7}$$

with the corresponding resonance wavelength given by $\lambda_0 = c_0/f_0$. These circuit relations provide only initial estimates, while the final response is determined through full-wave simulations.

In addition, Chapter 2 introduces several approaches for understanding the physical mechanisms underlying multilayer metamaterial filters such as effective impedance matching and Fabry–Pérot antireflection modes. These approaches can be applied to the present metamaterial and are discussed further in the Results section.

3.2.1 Computational methods

The optical response of the metafilters was simulated using the three-dimensional finite-difference time-domain (FDTD) method implemented in Ansys Lumerical. Because the metafilters are periodic structures, periodic boundary conditions were applied along the x- and y-directions, while perfectly matched layers (PMLs) were used along the z-direction to absorb outgoing waves and suppress artificial reflections from the simulation boundaries. The structure was illuminated from above by an x-polarized plane wave propagating along the negative z-direction.

During the initial simulations, the transmission monitor was placed at the bottom of the substrate. In the final simulations, the monitor was placed in air to represent a more realistic measurement configuration. To reduce Fresnel reflection at the substrate–air interface, a thin parylene antireflection coating with a refractive index of 1.63 was added to the bottom surface of the substrate. Its thickness was selected according to the quarter-wave condition, $t = \lambda_0/4n$, at the target wavelength.

The structures consisted of gold and silicon, with silicon used for both the substrate and the dielectric microparticles. Silicon was modeled using a refractive index of 3.417 and negligible absorption, making it a suitable high-index dielectric in the mid- and far-infrared spectral ranges considered in this study. Three factors help explain this behavior. First, at wavelengths longer than approximately 1.1 μm, photon energies are below the silicon

bandgap (1.12 eV), so single-photon interband absorption is strongly suppressed. However, multiphoton absorption, a nonlinear process in which two or more photons together provide enough energy to bridge the bandgap, can still contribute. For example, two-photon absorption can occur at incident wavelengths shorter than approximately 2.2 µm. However, multiphoton absorption is a nonlinear process whose rate scales with higher powers of the electric-field amplitude. It can become significant at high optical intensities and is usually weak at typical field strengths. Second, because silicon is nonpolar, it lacks the strong single-phonon infrared absorption bands found in polar semiconductors such as GaAs and InSb, although multiphonon absorption can still occur in the mid-infrared. Third, the relatively wide bandgap limits the intrinsic carrier concentration to approximately $10^{10}\,\mathrm{cm}^{-3}$ at room temperature. This low carrier concentration suppresses free-carrier absorption, which can otherwise be a major source of loss at terahertz frequencies. Consequently, high-resistivity silicon behaves as a nearly lossless dielectric over much of the near-infrared and terahertz regions.

In the simulations, silicon was modeled using its standard refractive index, with material absorption treated as negligible. The transmission monitor was placed at the end of the $200\,\mu$m-thick substrate, so the recorded power had propagated through the full substrate thickness. At an incident wavelength of $60\,\mu$m, the simulations show that most of the power entering the substrate reaches the monitor under this material assumption.

In a real silicon wafer, residual impurities can introduce free carriers even when the wafer is not intentionally doped. To estimate their effect, we consider only free-carrier absorption (FCA) and neglect multiphonon absorption. The fraction of power lost to FCA during a single pass through the substrate is $1 - \exp(-\alpha_{\mathrm{FCA}} d)$, where α_{FCA} is the free-carrier absorption coefficient at the incident wavelength and d is the substrate thickness. For $d = 200\,\mu\mathrm{m} = 0.020\,\mathrm{cm}$, keeping the FCA-induced transmission drop below 1% relative to the lossless case requires

$$\alpha_{\mathrm{FCA}} < \frac{-\ln(0.99)}{d} \approx 0.50\,\mathrm{cm}^{-1}.$$

In the weak-absorption limit, the Drude model relates the free-carrier absorption coefficient to the carrier density N through

$$\alpha_{\mathrm{FCA}} \simeq \frac{Ne\mu}{n_{\mathrm{Si}}\varepsilon_0 c[1+(\omega\tau)^2]}, \qquad \tau = \frac{\mu m^*}{e}, \qquad \omega = \frac{2\pi c}{\lambda},$$

where μ is the carrier mobility, m^* is the effective mass, and n_{Si} is the refractive index of silicon. The equation is evaluated in SI units, with N in m^{-3}, μ in $\mathrm{m}^2\,\mathrm{V}^{-1}\,\mathrm{s}^{-1}$, and α_{FCA} in m^{-1}. The calculation uses $n_{\mathrm{Si}} = 3.42$, $\mu_e = 1400\,\mathrm{cm}^2\,\mathrm{V}^{-1}\,\mathrm{s}^{-1}$ and $m_e^* = 0.26m_0$ for electrons, and $\mu_h = 450\,\mathrm{cm}^2\,\mathrm{V}^{-1}\,\mathrm{s}^{-1}$ and $m_h^* = 0.37m_0$ for holes, where m_0 is the free-electron mass. At $\lambda = 60\,\mu\mathrm{m}$, the absorption coefficient of $0.50\,\mathrm{cm}^{-1}$ corresponds to an estimated carrier density of $9 \times 10^{14}\,\mathrm{cm}^{-3}$ when electrons dominate or $6 \times 10^{14}\,\mathrm{cm}^{-3}$ when holes dominate. Thus, below the corresponding carrier-density limit, FCA reduces single-pass transmission through the substrate by less than 1%.

The complex refractive index of gold was obtained from the Ordal et al. [121] dataset. Figure 3.2 shows the three-dimensional simulation configuration and the corresponding layer, source, and monitor arrangement. The source is positioned above the structure and illuminates the cross from the top, while the transmitted light propagates into the substrate and is recorded by the transmission monitor, shown in yellow and positioned within the substrate.

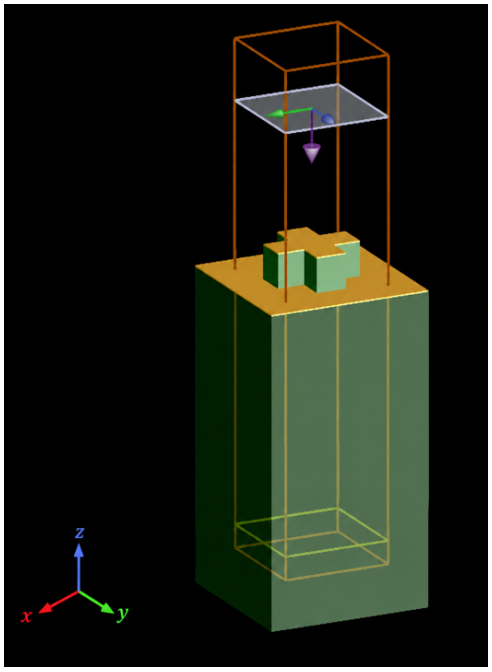

FIGURE 3.2: Three-dimensional CAD view of the simulated metafilter configuration, showing the layer arrangement and the positions of the incident source and transmission monitor.

The transmission spectrum was calculated using 1000 frequency points over the wavelength range from 10 to 120 μm. A sufficiently fine mesh relative to the structural dimensions and target wavelengths was employed. The main computational challenge was achieving a balance between numerical accuracy and a reasonable simulation time, which was typically a few hours for each simulation. A mesh-convergence analysis was also performed by progressively reducing the minimum mesh-element size and monitoring the corresponding changes in the transmission spectrum. This process was continued until further mesh refinement produced negligible changes in the calculated spectrum.

3.3 Results

Because the final structure consists of a complex multilayer building block, we first examine each component separately to determine its contribution to the overall optical response. We begin with a unit cell containing a single silicon bar periodically arranged on a silicon substrate. figure 3.3(a) shows the

unit-cell configuration and the corresponding transmission spectrum. A pronounced transmission peak appears near $(20\ \mu\mathrm{m})$, while the structure maintains a lower but still significant transmission at other wavelengths, because of the absence of an antireflection layer.

The silicon bar acts as a dielectric resonator and supports Mie-type modes near $(20\ \mu\mathrm{m})$. These modes depend on the bar's length, width, and height. Since the incident wavevector is directed along the height of the bar, its vertical dimension affects the phase accumulation, optical path length, and internal reflections, potentially producing Fabry-Perot-like longitudinal modes. In contrast, the lateral dimensions determine the transverse confinement and the distributions of the electric and magnetic dipolar or higher-order modes.

When the bar is rotated by (90°) and aligned with the x-direction, as shown in Fig. 3.3(b), the x-polarized incident field couples to its longer lateral dimension. The increased transverse optical path shifts the fundamental resonance toward a longer wavelength and allows additional higher-order modes to appear within the investigated spectral range. In Fig. 3.3(c), two perpendicular bars are combined to form a cross-shaped resonator. As expected, its transmission spectrum contains the resonances associated with both bar orientations, thereby covering the resonant responses of the two individual structures. Near-field coupling between the perpendicular bars further hybridizes these modes and broadens the resulting resonances.

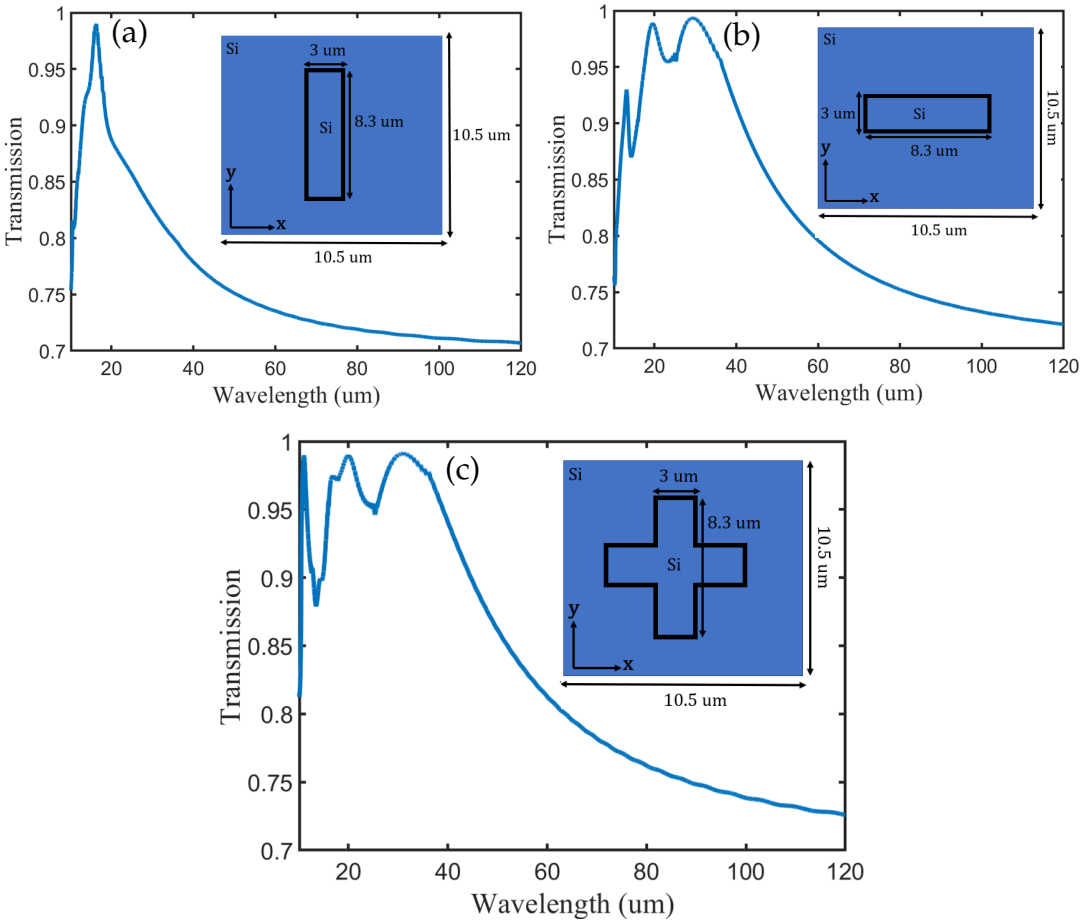

FIGURE 3.3: (a)-(c) Transmission spectra and corresponding unit-cell configurations of metasurfaces consisting of (a) a Si bar oriented along the y-direction, (b) a Si bar oriented along the x-direction, and (c) a Si cross. In all three configurations, the resonators are placed on a Si substrate and have a thickness of 4.6 μm.

In the next step, we simulate the transmission spectra of the structures presented in the previous section after coating the top surfaces of the bars and cross-shaped resonator with a 200-nm-thick gold layer. As is well known, the incident electric field causes opposite charges to accumulate at the edges of metallic strips. This charge accumulation concentrates the electric field and stores electrostatic energy, producing an effective capacitive response [100]. Consequently, the patterned gold layer exhibits low-pass behavior in the frequency domain, corresponding to long-pass behavior in the wavelength domain: wavelengths above a specific cutoff are transmitted, whereas shorter

wavelengths are suppressed. As shown in Figs. 3.4(a)-(c), this long-pass transmission behavior is clearly observed. In figure 3.4(a), the bar is oriented parallel to the incident polarization, resulting in a longer interaction length along the polarization direction and, consequently, a cutoff at a longer wavelength [44]. In figure 3.4(b), the bar is oriented perpendicular to the incident polarization; therefore, the shorter interaction length shifts the cutoff toward shorter wavelengths. In figure 3.4(c), the two perpendicular bars are combined to form a cross. Consequently, the cutoff is primarily determined by the bar with the longer cutoff wavelength, while the overall spectrum reflects the responses of both bars and their hybridization.

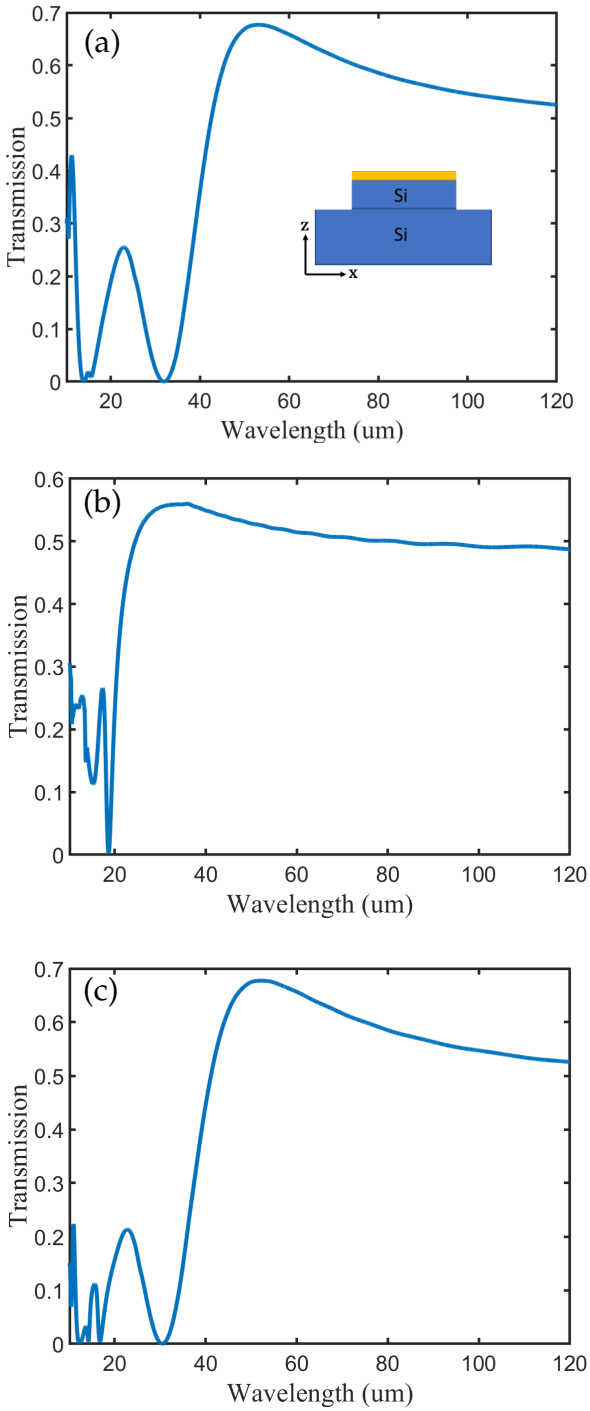

FIGURE 3.4: (a)-(c) Transmission spectra and corresponding unit-cell configurations of metasurfaces consisting of (a) a Si bar oriented along the x-direction, (b) a Si bar oriented along the y-direction, and (c) a Si cross. In all three configurations, the Si resonators are placed on a Si substrate, have a thickness of 4.6 μm, and are covered with a 200 nm-thick Au layer.

In this step, we consider a periodic array of silicon bars placed on a silicon substrate coated with a 200-nm-thick gold layer containing bar-shaped apertures. This patterned gold film is complementary to the metallic layer described in the previous section. In this configuration, the top surface of each silicon bar remains uncoated.

Figures 3.5 (a)-(c) show the unit-cell configurations and their corresponding transmission spectra. In Fig. 3.5(a), transmission is suppressed at longer wavelengths, whereas shorter wavelengths are transmitted, although the passband is not uniform. By contrast, Figs. 3.5(b) and 3.5(c) exhibit predominantly band-pass responses, indicating that these structures cannot be described as purely inductive layers. The presence of the Si substrate and the Si bar or cross introduces additional resonant and coupling effects, particularly at shorter wavelengths. Nevertheless, the spectrum of the cross-shaped structure retains spectral features associated with the responses of its two perpendicular bars.

the question is how the response changes when these structures are combined such that a Si bar or cross is sandwiched between two complementary metallic layers. Conceptually, stacking the layers can be regarded as an "AND" operation because only the wavelength range transmitted by both layers is expected to pass through the complete structure. In the absence of strong coupling and multiple-reflection effects, the resulting transmission may be approximated by the product of the individual transmission spectra. However, vertical coupling between the two metallic layers and the Si resonator can introduce additional spectral features and significantly modify the overall response [122], [123]. Since the cross-shaped configuration provides more geometrical degrees of freedom and exhibits lower transmission within the stopband, it is selected as the final proposed design [118].

In the preceding sections, the responses of the different components of the multilayer structure were examined separately. We now combine these components to investigate the response of the complete structure. It should be noted that extensive optimization was performed for both the individual

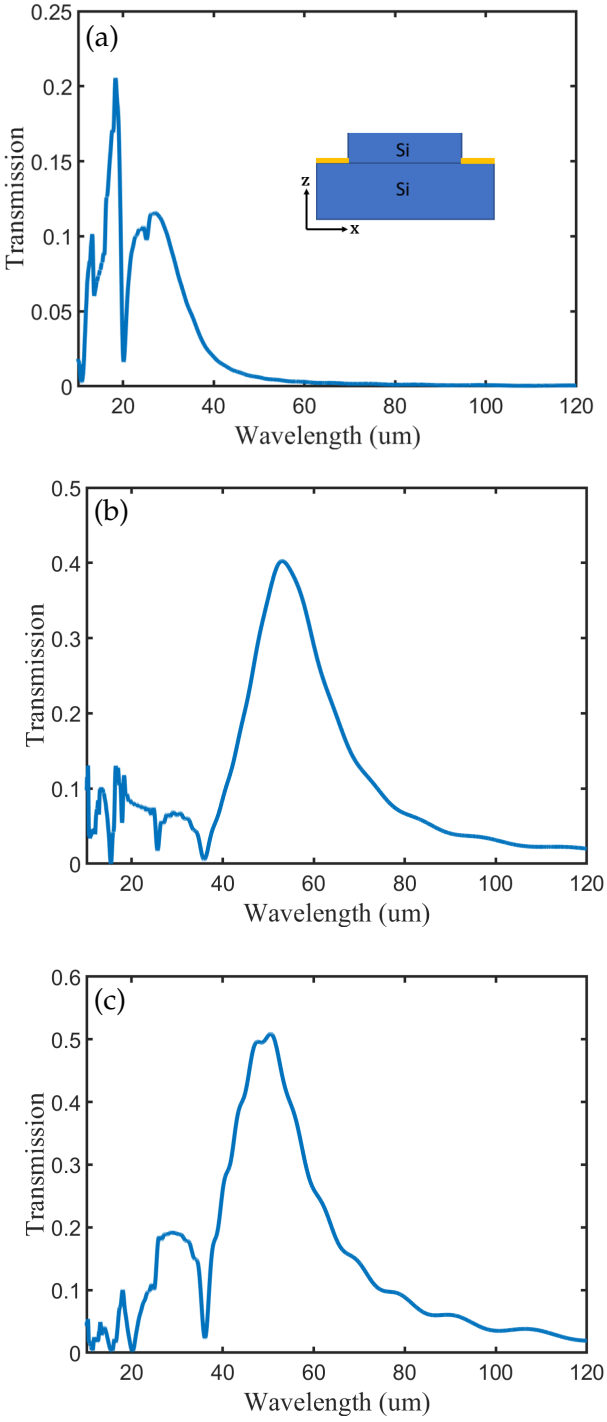

FIGURE 3.5: (a)-(c) Transmission spectra and corresponding unit-cell configurations of metasurfaces consisting of a Si substrate, a 200 nm-thick Au layer patterned with complementary apertures, and 4.6 μm-thick Si resonators positioned within the apertures and directly on the substrate. The Si resonators consist of (a) a bar oriented along the x-direction, (b) a bar oriented along the y-direction, and (c) a cross.

components, including the Si bars, Si crosses, and patterned Au layers, and the final multilayer configuration. The results presented so far correspond to the relevant optimized individual components used to construct the final design.

We now introduce the proposed design, as shown in Figure 3.1. The structure consists of a periodic arrangement of Si crosses covered by gold crosses on a Si substrate. The substrate is also coated with a gold layer containing cross-shaped apertures, forming the complementary metallic layers discussed in the previous sections. The response of the complete stacked structure is consistent with the preceding discussion of combining low-pass and high-pass filtering responses together with vertical coupling between the layers. The transmission spectrum of the complete structure is shown in Figure 3.6. Cascading the two metallic layers produces a cleaner transmission spectrum with stronger stopband suppression and sharper band edges. The vertical coupling, which is strongly influenced by the cross height, is optimized to suppress the sidelobes, enhance the passband transmission, and broaden the bandwidth within the desired spectral range.

As discussed earlier in this chapter and in the theoretical framework presented in Chapter 2, the antireflective response of such multilayer structures can be interpreted in several ways. One interpretation is based on a Fabry-Perot cavity model, in which the two metallic layers act as partially reflecting interfaces, while the region containing the Si cross serves as the cavity medium. At the passband wavelengths, the waves partially reflected from the interfaces interfere destructively, reducing the overall reflection, while the transmitted waves interfere constructively and enhance the transmission. Outside this range, the interference conditions are no longer satisfied, resulting in the desired filtering response [97], [99], [100], [118].

Alternatively, the complete metamaterial may be approximated as an effective medium with an effective impedance Z_{eff}. Within the passband, Z_{eff} approaches the impedance of the incident medium, thereby reducing the impedance mismatch and suppressing reflection. If the impedance is normalized to that of free space, this matching condition can be expressed as

$Z_{\text{eff}} \approx 1$ [99].

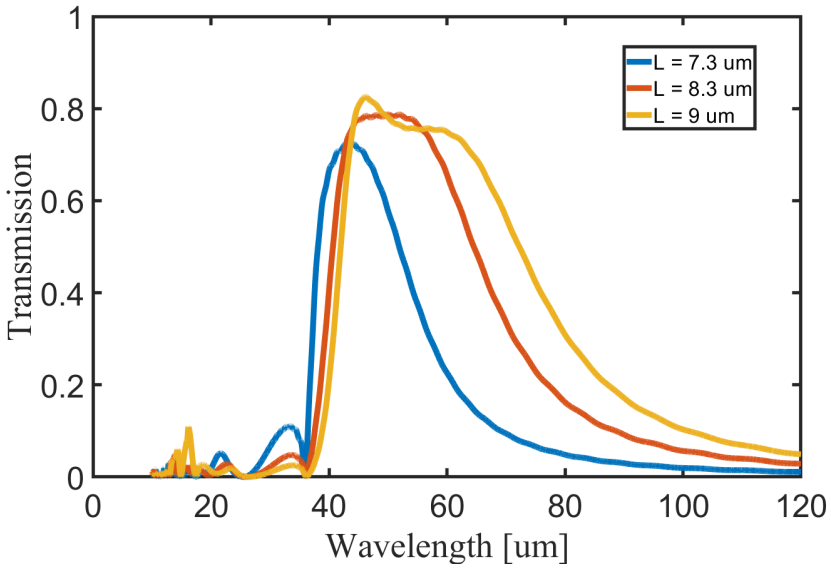

FIGURE 3.6: Transmission spectra of the configuration shown in Figure 3.1 for different cross lengths. The incident wave is x-polarized and propagates along the -z direction, illuminating the structure from the top. The fixed geometrical parameters are $p_x = p_y = 10.5$ μm and $w = 3$ μm, with $h = 4.6$ μm.

Figure 3.6 shows the transmission spectra as a function of wavelength for different values of the cross-arm length respectively. Variations in the geometrical parameters modify the effective Fabry-Perot cavity formed within the complete stacked structure. Changing the length and width alters the reflection coefficients at the interfaces, whereas changing the resonator height modifies the optical path length and the phase accumulated by the light along the propagation direction. Consequently, these variations shift the central wavelength of the transmission band.

In the simulations, a quarter-wavelength parylene layer was also added at the bottom of the substrate to reduce the refractive-index contrast between Si and air and thereby enhance the transmission.

To further demonstrate the tunability of the proposed filter through variation

of its geometrical parameters, the structure was reoptimized to exhibit the antireflection/bandpass response at wavelengths of approximately 30 μm and 80 μm. The corresponding transmission spectra are shown in Figures 3.7(a) and 3.7(b), respectively. In particular, Achieving a clear bandpass response around 30 μm is also notable, considering the increased design sensitivity at shorter wavelengths. These results demonstrate the ability of the proposed design to maintain its filtering functionality over a broad range of operating wavelengths.

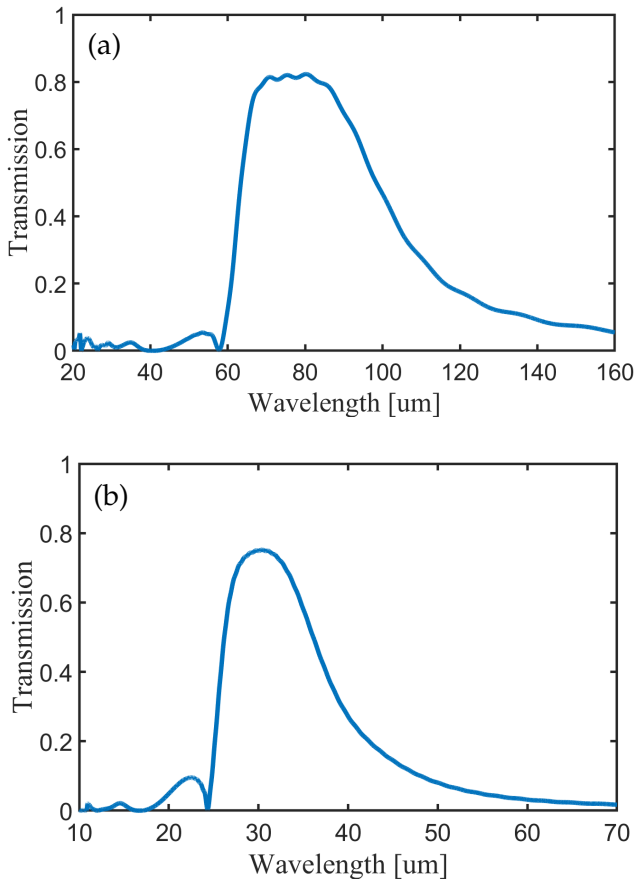

FIGURE 3.7: Transmission spectra as a function of wavelength for filters designed around central wavelengths of (a) 80 μm and (b) 30 μm. The incident wave is x-polarized, propagates along the $-z$ direction, and illuminates the structure from the top. The optimized geometrical parameters are (a) $p_x = p_y = 16.8$ μm, $l = 13.2$ μm, $h = 7$ μm, and $w = 4.5$ μm; and (b) $p_x = p_y = 7.1$ μm, $l = 5.1$ μm, $h = 3$ μm, and $w = 2$ μm.

For all three filters, the short-wavelength edge rises more sharply than the

long-wavelength edge falls. The two edges are governed by different filtering responses. The capacitive responses sets the short-wavelength edge, while the inductive responses sets the long-wavelength edge. For each filter, the reported design gave the best balance we obtained in simulation between edge sharpness and the desired passband response. Further optimization could sharpen the long-wavelength edge, but doing so may come at the expense of other passband characteristics, such as bandwidth or peak transmission.

figure 3.8 presents the transmission spectra of the optimized structure without an antireflection coating for different polarization angles. The overlapping spectra confirm its polarization-insensitive response, which arises from the two perpendicular arms. Each arm interacts with the corresponding orthogonal component of the incident electric field; therefore, any linear polarization can be decomposed into these two components and experiences the same overall transmission [122].

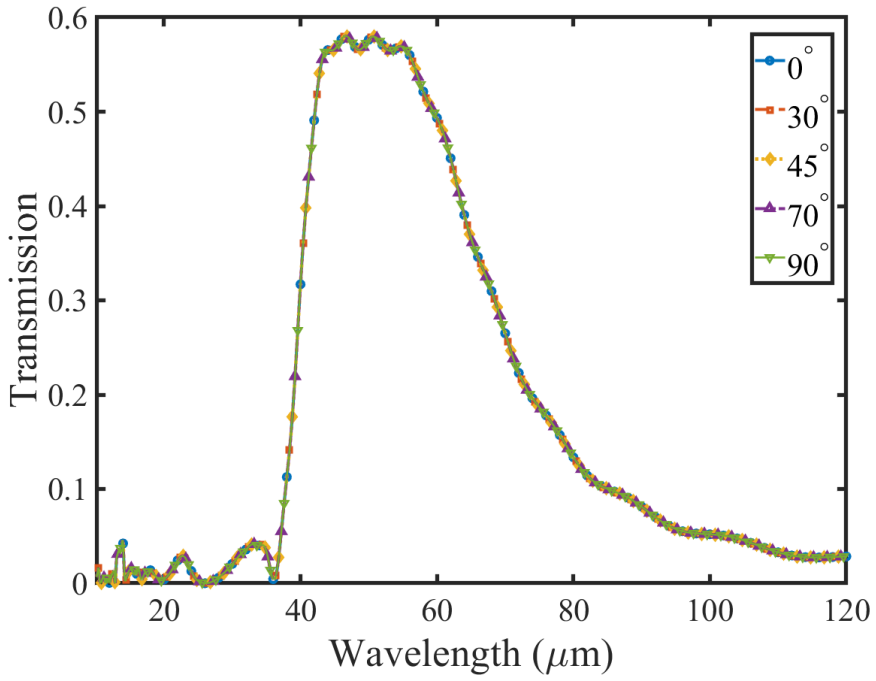

FIGURE 3.8: Transmission spectra of the optimized structure for different incident polarization angles.

3.4 Conclusion

In this chapter, we proposed a metasurface consisting of periodically arranged metalized silicon (Si) crosses on a dielectric substrate coated with a thin metallic film with cross holes. The patterned crosses and the metallic film form two complementary layers separated by a dielectric spacer. By optimizing the geometrical parameters, the proposed structure was shown to operate as a broadband bandpass filter with optimized performance around the central wavelengths of 30 μm, 55 μm, and 80 μm.

We explained the design process step by step. We began by analyzing the spectral responses of the silicon bars and crosses, and then coated them with a gold bar layer. In the next step, we removed the gold coating and instead deposited a gold layer with complementary bar-shaped apertures on top of the substrate. The results revealed the characteristic signatures of high-pass and low-pass filtering behavior for each of the complementary layers. These two layers were then combined to achieve a bandpass response. We also interpreted the results using alternative approaches, including a Fabry–Pérot cavity model and effective impedance matching. Finally, we demonstrated that the proposed optimized filter is insensitive to the polarization of the incident light.

Overall, this work demonstrates that complementary plasmonic metasurfaces provide an effective platform for realizing high-performance bandpass filters in the mid- and far-infrared spectral regions. The proposed design combines high transmission within the passband, strong suppression in the stopband, sharp spectral roll-off and a simple structural design, making it a promising candidate for applications in astronomy and medicine.

Chapter 4

Orientation-Resolved SHG Imaging: The Role of Near-Field Interactions

The core concept of this project was jointly developed during regular collaborative meetings between our group and Prof. Lora Ramunno's group and was further refined through ongoing discussions and feedback.

The modelling and design of the metasurfaces were carried out by Dr. Sina Aghili and me using commercial software, including Lumerical and COMSOL, under the supervision of Prof. Dolgaleva. I was responsible for performing the numerical simulations, developing and optimizing the designs, and analyzing the results with Prof. Dolgaleva and Dr. Aghili. The theoretical analysis and numerical validation were performed by Prof. Ramunno's group using a homemade hydrodynamic-model code. The corresponding samples were fabricated by Dr. Lais Fujii dos Santos, a former postdoctoral fellow in our group, and Athulya Thulaseedharan, a PhD student in our group. The nonlinear imaging setup was provided by the imaging laboratory of Prof. François Légaré at INRS, and the nonlinear measurements were conducted there by Dr. Arash Aghigh, a postdoctoral fellow in Prof. Légaré's laboratory. In the experimental work, Dr. Aghili and I contributed to the linear and nonlinear measurements. My specific contributions to the experimental work included aligning the linear optical setup in our laboratory at the University of Ottawa, performing the linear measurements, and assisting with the nonlinear measurements at INRS. The manuscript reporting the results described in this chapter, entitled "Orientation-Resolved SHG Imaging:

The Role of Near-Field Interactions," has been submitted to the *Journal of the Optical Society of America B*. Related work on a random plasmonic metasurface for enhanced SHG was published in the proceedings of Photonics North 2026 [124]. Related work on proximity effect correction in the fabrication of plasmonic metasurfaces was published in the *Journal of the Optical Society of America B* [125].

4.1 Introduction

Microtubules (MTs) are key components of the neuronal cytoskeleton, providing structural support and tracks for intracellular transport [126]. They play a central role in maintaining neuronal polarity, which is essential for nervous system function [126]. This polarity arises from the geometric asymmetry of MTs [127], a feature that has traditionally been difficult to observe in living tissue [128].

Second-harmonic generation (SHG) microscopy, being sensitive to noncentrosymmetric molecules [129], such as microtubules (MTs) [130], offers a powerful means to visualize molecular structure [131]. It further enables probing of MTs polarity through detection of their axial orientation, which is important for understanding neuronal organization and function.

Plasmonic nanostructures, by supporting LSPRs, provide a versatile platform for manipulating light at the nanoscale [43] and enabling functionalities that are otherwise difficult to achieve with conventional optical systems, while maintaining compact configurations that avoid the need for bulky optical components [132]. By concentrating electromagnetic energy into subwavelength regions, they generate intense and highly localized fields [45]. This confinement reduces the effective probing volume and enhances interactions with nearby molecules, making such platforms particularly attractive for single molecule detection with high temporal resolution [133], [134].

Recent advances have shown that integrating SHG microscopy with plasmonic nanostructures can significantly improve signal strength from biological samples [123]. When the resonance wavelength of the nanostructure matches the excitation wavelength, the resulting amplification of the local electromagnetic field increases the SHG response from nearby structures [88], [135], which improves the sensitivity of SHG microscopy [136], enabling more precise visualization of microtubule polarity in complex biological environments.

In this work, we investigate arrays of gold nanoparticles with noncentrosymmetric geometries and varied spatial orientations as a model platform for polar biomolecular networks. The nanoparticle dimensions were designed such that their plasmonic resonances match the pump wavelength. Using numerical simulations, we examine how particle orientation influences the nonlinear response of isolated nanoantennas under different excitation polarizations. We then extend the analysis to multi-particle unit cells, which more closely resemble realistic systems and enable the investigation of near-field interactions between neighboring particles. Finally, we fabricate and characterize both uniform and columnar metasurfaces and use near-field SHG images to estimate particle orientation. Overall, this work introduces a metasurface platform for emulating dense assemblies of polar biomolecules with an enhanced, polarization-independent, and phase-matching-free nonlinear optical response, and demonstrates the use of near-field SHG intensity distributions to infer the geometrical properties of meta-molecules, including their polarity and orientation.

4.2 Methodology

The nonlinear optical response of the gold nanoparticles is modeled within the hydrodynamic framework, which captures the collective motion of free electrons under an external electromagnetic field through the coupled continuity and Euler equations [115], [137]. Under time-harmonic excitation, the electron dynamics can be treated perturbatively, leading to a nonlinear source responsible for second-harmonic generation. Under the undepleted pump approximation, the resulting nonlinear polarization is expressed as

$$\mathbf{P}_{\mathrm{NL}} = \frac{ne^3}{m_e^{*2}(2\omega + i\gamma)(\omega + i\gamma)} \left[\frac{1}{\omega} \mathbf{E}_1 (\nabla \cdot \mathbf{E}_1) + i\mu \mathbf{E}_1 \times \mathbf{H}_1 + \frac{1}{\omega + i\gamma} (\nabla \cdot \mathbf{E}_1) \mathbf{E}_1 \right], \tag{4.1}$$

where the first term represents the electrostatic (Coulomb) contribution, the second term corresponds to the magnetic Lorentz-force, and the third term originates from the convective nonlocality of the electron motion [115]. The corresponding nonlinear current density is given by

$$\mathbf{J}_{\mathrm{NL}} = -i2\omega \mathbf{P}_{\mathrm{NL}}, \tag{4.2}$$

which acts as the source term for the second-harmonic emission.

The second-harmonic field is evaluated using nonlinear scattering theory (NST), which, based on Lorentz reciprocity, relates the far-field radiation at 2ω to the overlap integral between the nonlinear polarization induced by the incident field and the field radiated by a test dipole placed in the far field [116]. The far-field second-harmonic emission can be written as

$$E_{\mathrm{FF},2\omega} \propto \int_V P_{\mathrm{NL}}(\mathbf{r}, 2\omega) \cdot E_{2\omega}(\mathbf{r})\, dV, \tag{4.3}$$

where $P_{\mathrm{NL}}(\mathbf{r}, 2\omega)$ is the nonlinear polarization at the harmonic frequency. For a second-order process, this polarization can be written as [138]:

$$P_{\mathrm{NL}}(\mathbf{r}, 2\omega) = \varepsilon_0 \chi^{(2)}_{\mathrm{eff}}(\mathbf{r}) \left[E_\omega(\mathbf{r}) \right]^2. \tag{4.4}$$

Substituting this expression into Eq. (4.3) gives

$$E_{\mathrm{FF},2\omega} \propto \int_V \varepsilon_0 \chi^{(2)}_{\mathrm{eff}}(\mathbf{r}) \left[E_\omega(\mathbf{r}) \right]^2 E_{2\omega}(\mathbf{r})\, dV, \tag{4.5}$$

indicating that the SHG emission is governed by the spatial overlap between the fundamental field, the nonlinear polarization, and the harmonic field distribution.

The above formulation is implemented numerically to evaluate the nonlinear response of the metasurface. The structure is modeled in COMSOL Multiphysics using periodic boundary conditions along the x- and y-directions and perfectly matched layers (PMLs) along the z-direction. A silica substrate with a refractive index of 1.44 is included. The nonlinear response was evaluated using a two-step approach in COMSOL Multiphysics. First, a linear study was performed at the fundamental wavelength to calculate the electric-field distribution throughout the simulation domain. Input and output ports were defined, and the incident power at the input port was set to match the experimental power measured before the focusing objective. This power was chosen to produce a detectable second-harmonic signal while keeping the intensity at the focus below the sample damage threshold. The resulting local electric field was then used to calculate the nonlinear current density at the second-harmonic frequency within the hydrodynamic framework. In the second study, this current density was introduced as a source term to calculate the far-field response at the second-harmonic wavelength.

4.3 Design

The proposed structure is shown in figure 4.1. The dimensions are optimized such that the nanoparticle exhibits an LSPRs at the pump wavelength (1100 nm) [120], [123]. Owing to the anisotropic nature of this geometry, the resonance is observed only under x-polarized and 45°-polarized excitation (the resonance characteristics, including the quality factor and spectral linewidth, differ for these two polarizations).

To accurately examine the linear response and investigate the influence of rotation on the resonance, we analyzed several periodic arrays with a period of 2 μm, each designed such that every unit cell contains a single nanoparticle with a fixed orientation. The periodicity was chosen to ensure that the nanoparticles remain sufficiently separated to prevent interactions.

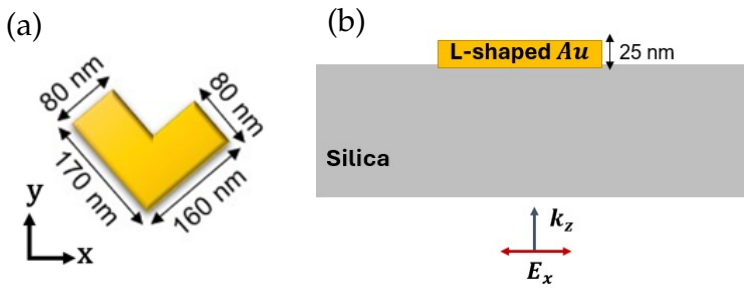

FIGURE 4.1: (a) Unit cell geometry of the metasurface design composed of a single asymmetric V-shaped nanoparticle. (b) Overall metasurface configuration. The Au nanoparticle is 25 nm thick, with a 3 nm-thick chromium adhesion layer between the Au and the silica substrate.

figure 4.2 presents the simulated transmission spectra of the arrays under x-, y-, and 45°-polarized excitation. The spectra show that the V-shaped particle supports a resonance near 1100 nm under x- and 45°-polarized excitation, whereas no resonance is observed at this wavelength for y polarization. In contrast, near 800 nm, the behavior is reversed, with resonances appearing under y- and 45°-polarized excitation but absent for x polarization. This behavior is consistent with the scaling of the plasmonic resonance wavelength with the effective optical path length experienced by the incident electric field vector [45]. When the V-shaped particle is excited with x-polarized light, the larger effective interaction length produces a resonance at 1100 nm, whereas y-polarized excitation, associated with a shorter interaction length, shifts the resonance to around 800 nm. Under 45° polarization, the incident field decomposes into equal x and y components, each carrying half of the incident intensity. Consequently, resonant behaviour emerges at both wavelengths; however, the weaker coupling to each eigenmode results in lower-quality resonances compared with purely x- or y-polarized excitation [139].

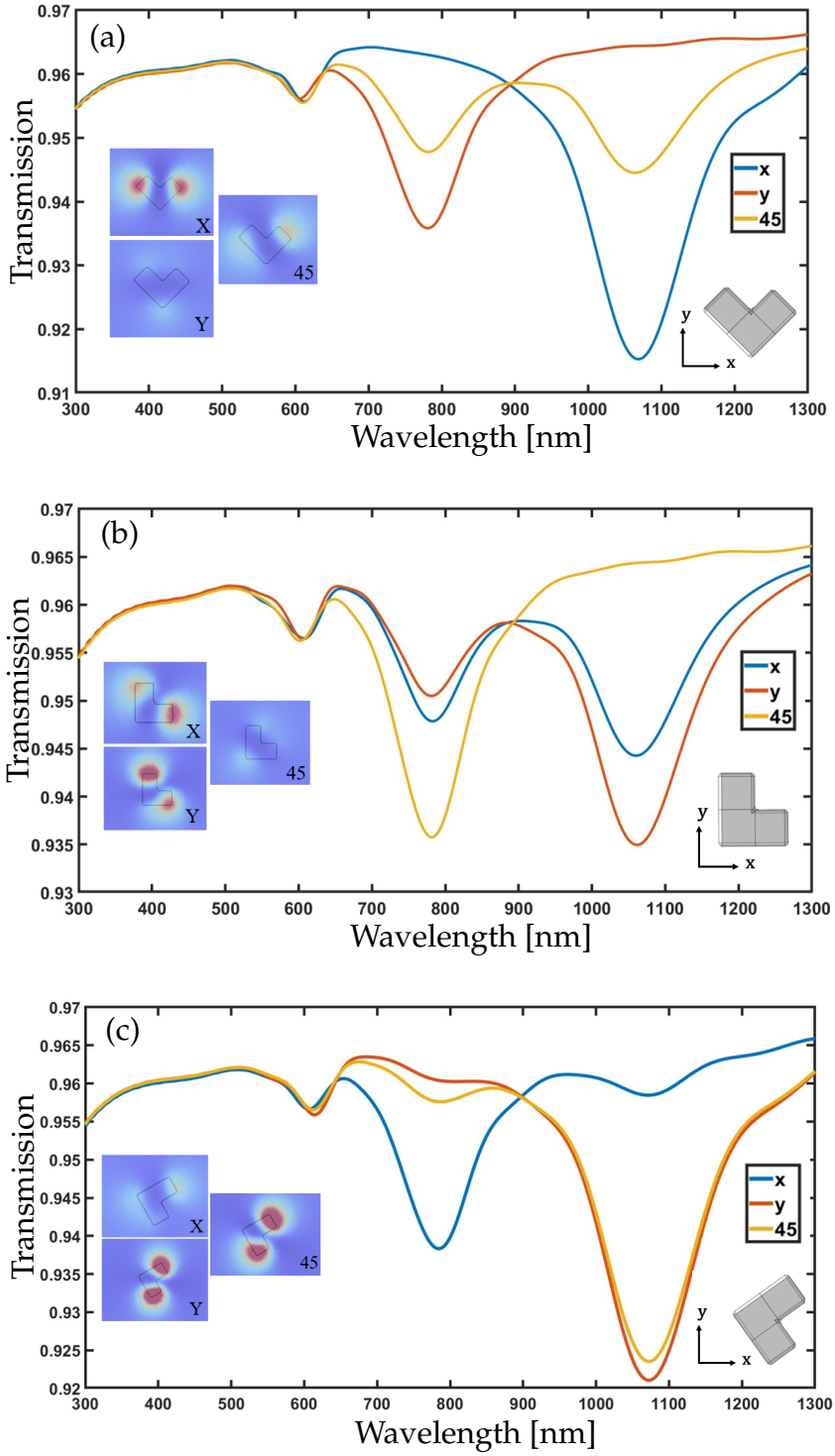

FIGURE 4.2: (a) Simulated transmission spectra of the metasurface and corresponding hotspot images (at a wavelength of 1100 nm), for a unit cell containing a V-shaped particle under *x*-, *y*-, and 45° polarizations. (b) Corresponding results for an L-shaped particle. (c) Corresponding results for a particle with a −60° orientation.

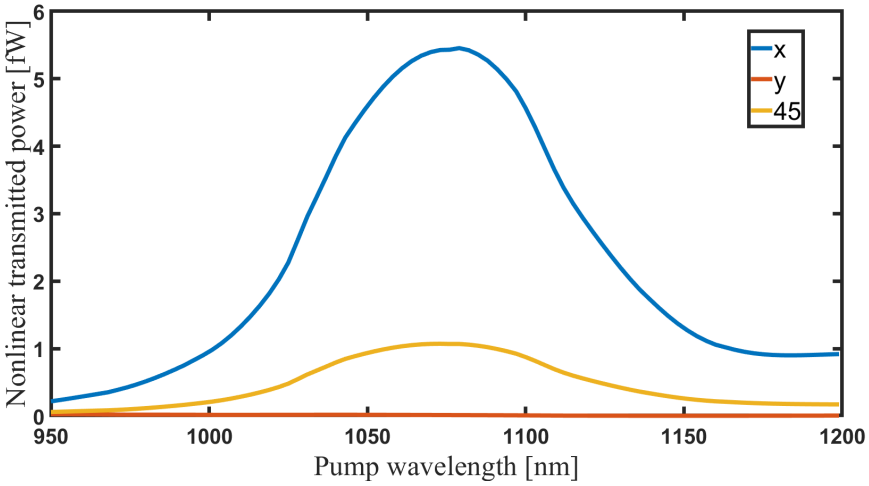

FIGURE 4.3: Simulated nonlinear transmitted power per unit cell of the metasurface with a unit cell consisting of a V-shaped particle (2 μm periodicity) as a function of pump wavelength. under x-, y-, and 45°-polarized excitation.

Similarly, plasmonic resonances near 1100 nm are observed for the L-shaped particle when excited with x- and y-polarized light, and for the particle with a rotation angle of $-60°$ when excited with y- and 45°-polarized light, respectively. This behavior is consistent with the fact that the key parameter is the relative angle between the incident polarization and the nanoparticle orientation. For example, the V-shaped particle under y polarization is effectively equivalent to the L-shaped particle under 45° polarization.

A clear SHG emission peak corresponding to a pump wavelength of 1100 nm (SHG wavelength at 550 nm) is observed in Fig. 4.3 and Fig. 4.4 for x and 45° polarizations, while no significant SHG signal appears under y polarization. These results confirm that efficient SHG occurs only for polarizations that excite a plasmonic resonance at the fundamental wavelength (1100 nm). The noncentrosymmetric geometry of the L-shaped meta-atoms gives rise to a nonzero second-order susceptibility tensor, while the supported LSPR enhances the electric field intensity at the pump wavelength, leading to a strong nonlinear emission [140], [141], [142]. The hotspot images in Fig. 4.2 further reveal dipolar field distributions for the resonant orientations, which govern the spatial profile and efficiency of the SHG response [143].

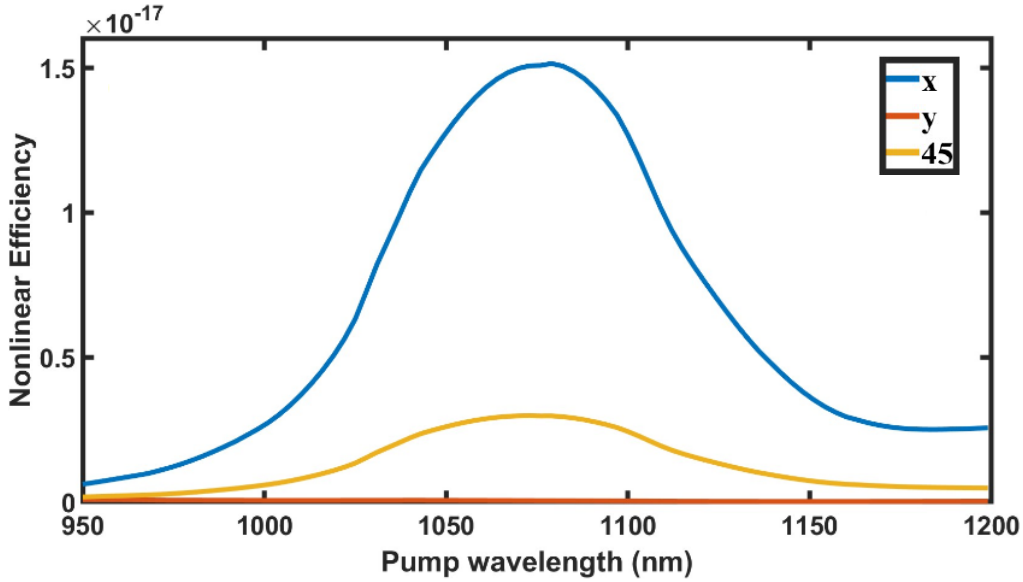

FIGURE 4.4: Simulated nonlinear conversion efficiency of the metasurface with a unit cell consisting of a V-shaped particle (2 μm periodicity) as a function of pump wavelength under x-, y-, and 45°-polarized excitation.

After analyzing the optical response of a unit cell containing an isolated metamolecule (MT), we extend our study to arrays composed of unit cells with multiple MTs of different orientations, providing a closer approximation to realistic systems. This approach enables us to investigate how particles with varying orientations interact and how such interactions can be exploited to enhance or suppress the overall nonlinear signal. An important advantage of this configuration is that at least one particle is favorably aligned with any given incident polarization. As a result, a plasmonic resonance at the fundamental wavelength can always be excited, leading to efficient polarization-insensitive SHG emission.

To explore this concept, we numerically investigate periodic arrays in which each unit cell contains four nanoparticles with distinct rotation angles and positions, as illustrated in figure 4.5. The arrays have a lattice constant of 2 μm, with an internal spacing of approximately 1 μm between neighboring particles.

The spatial field distributions in Fig. 4.5 agree well with the single-particle behavior shown in Fig. 4.2. Under y-polarized excitation, the field is only

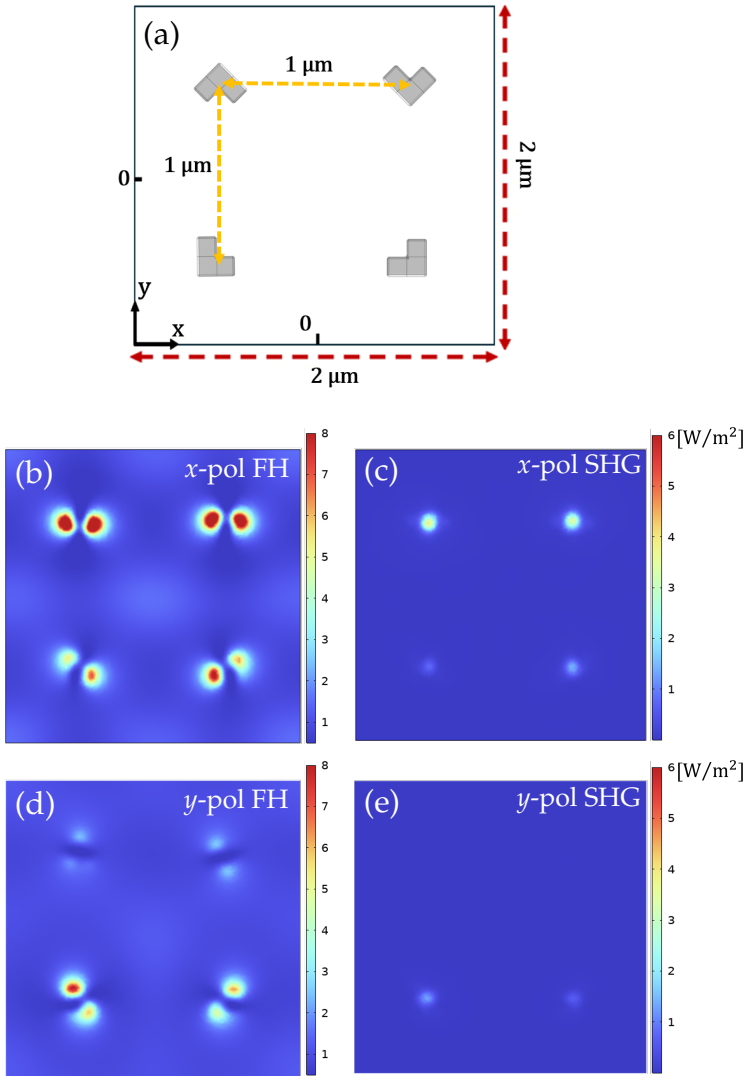

FIGURE 4.5: Simulated geometry and field distributions. (a) Geometry and particle arrangement within the unit cell. (b) and (d) Normalized linear near-field intensity distributions evaluated 50 nm above the particle surface at the pump wavelength (1100 nm) under x- and y-polarized illumination, respectively. (c) and (e) Corresponding nonlinear near-field intensity distributions at the second-harmonic wavelength (550 nm) under x- and y-polarized excitation, respectively.

weakly localized around the L-shaped particles, whereas under x polarization the V-shaped particles dominate the hotspot formation, with weaker enhancement also observed near the L-shaped structures. Because the left- and right-handed L-shaped particles are related by a 90° rotation rather than

mirror symmetry, each orientation couples differently to the incident polarization. Consequently, the nonlinear response at 550 nm is strongest for the structures resonant at the fundamental wavelength, highlighting the dominant role of the LSPR in the SHG process [142].

Finally, as evident from the intensity maps, the overall response can be interpreted as the superposition of individual nanoparticle contributions, with coupling remaining weak. This behavior is mainly attributed to the 1 μm separation and the variation in orientations.

In addition, the nonlinear fields emitted by differently oriented particles can be used to engineer the far-field nonlinear phase front [144]. However, this aspect is beyond the scope of the present work and is not investigated here.

We now introduce an additional nanoparticle at the center of the unit cell, with its distance to the surrounding structures reduced to below 1 μm, as shown in figure 4.6. This configuration allows us to investigate how closer spacing can enhance and control particle interactions within the unit cell, providing a useful model for studying interacting, randomly oriented MTs.

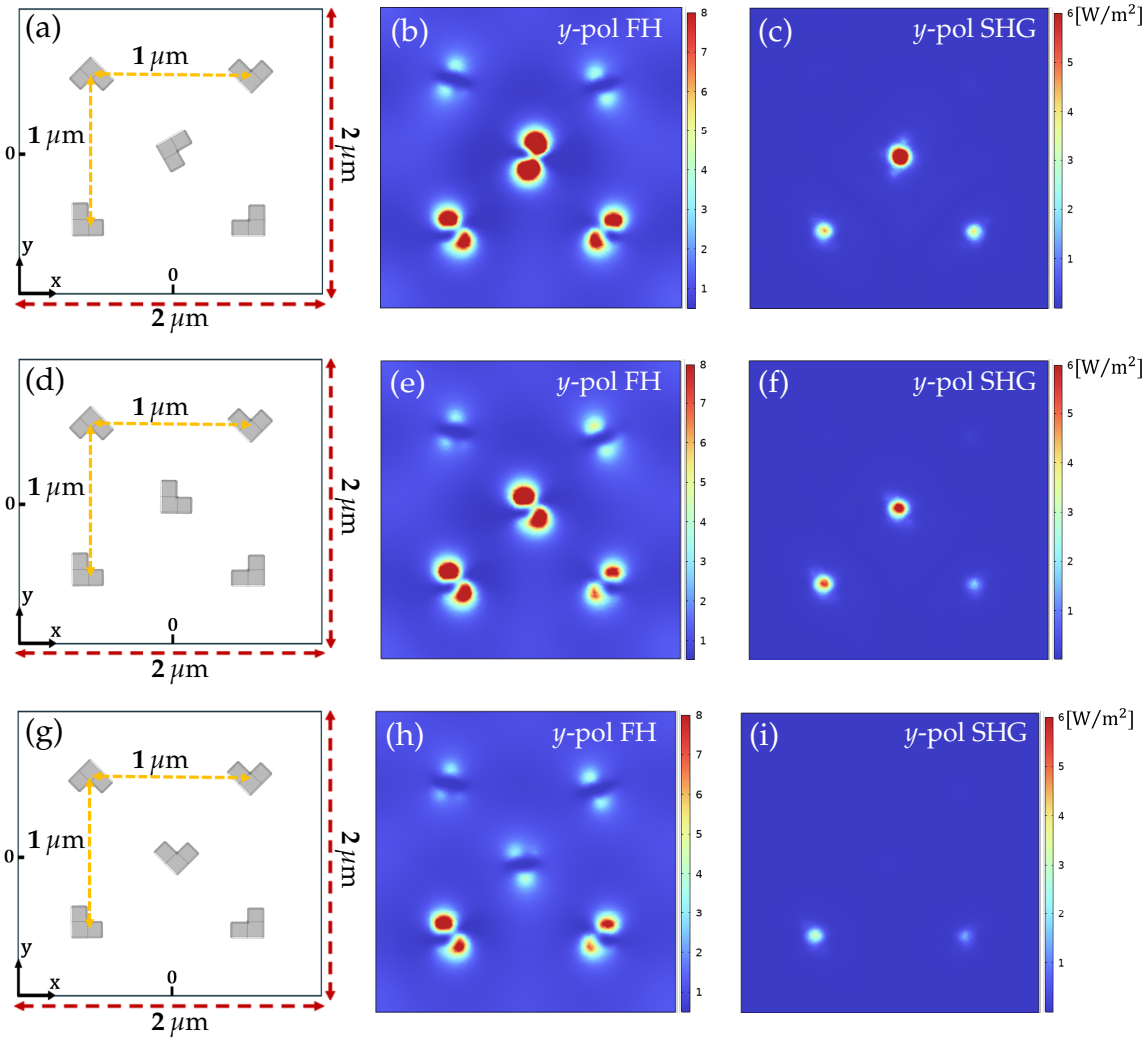

FIGURE 4.6: Simulated geometries and near-field distributions. (a), (d), and (g) show the geometries and particle arrangements within the unit cell. (b), (e), and (h) show the normalized linear near-field intensity distributions, evaluated 50 nm above the particle surface at the pump wavelength (1100 nm), for the unit cells with the middle particle oriented at -60°, L-shaped, and V-shaped, respectively, under *y*-polarized illumination. (c), (f), and (i) show the corresponding nonlinear near-field intensity distributions for the same unit cells.

Comparison of Fig. 4.6(h, i) with Fig. 4.5(d, e) reveals that, under *y*-polarized excitation, the presence of the central V-shaped element increases the field intensity around the lower L-shaped particles. Although the V-shaped particle exhibits negligible excitation under *y* polarization, it can still interact with

neighboring structures because of the small separation between them. However, this interaction remains relatively weak because this orientation does not strongly couple to y-polarized excitation.

For the L-shaped central particle, the field intensity is significantly enhanced around the lower right-handed L, whereas only a slight change is observed at the position of the left-handed L compared with the four-particle unit cell. This behavior indicates stronger coupling between structures with the same orientation, while the interaction between the orthogonally oriented particles remains weak.

For -60° oriented middle particle, a strong central hotspot is observed under y-polarized excitation, which enhances the field intensity at the positions of the two lower L-shaped particles.

Based on these results, field enhancement is governed by the interplay between the polarization, particle orientation, and spacing. When the incident polarization selectively excites two nearby particles with similar orientations, they can interact constructively, leading to enhanced local fields at their respective positions [145]. The maximum enhancement occurs when the particles have the same orientation, resulting in coherent coupling.

This behavior can be understood by modeling the gold nanoparticles as electric dipoles. In this picture, the local field at each particle is the superposition of the incident field and the fields radiated by neighboring dipoles. In this context, the coupling strength between two particles depends on the relative orientation of their effective dipole moments [146] and their separation distance.

In general, within the simplest dipole model, the coupling between two dipoles is stronger when they are aligned and weaker when they are perpendicular. As the angle between the dipole moments increases, the overlap of their induced fields decreases. Under such conditions, each particle supports a resonant field for a different incident polarization, which reduces the coupling between them [146]. This approximation is most accurate for elongated

nanoparticles with a large aspect ratio. As the particle width becomes comparable to its length, this simple dependence breaks down, and both geometry and distance play a more significant role.

The distance is also critical in determining the interaction [147]. For sufficiently small separations, even particles with orthogonal orientations can exhibit noticeable coupling [148].

4.4 Fabrication

Commercially available Fused Silica (JGS2) was used as the substrate for the fabrication of the metasurface presented in this work. After standard cleaning in acetone and IPA, the samples were dried on a hotplate at 180° C for 5 minutes. A bilayer of positive-tone electron beam resists—MMA (MMA EL6) and PMMA (PMMA A3) was applied, with MMA spun first, followed immediately by a 3-minute bake at 180 °C. PMMA was then coated on top, followed immediately by a 5-minute bake at 180°C to remove solvent and solidify the film. A layer of Electra 92 was spun on top of the MMA-PMMA bilayer to improve charge dissipation. Patterning of the bilayer resist was performed using a 100 kV (JEOL) electron beam lithography system. Post-exposure, the Electra layer was removed in a water bath and the substrate was developed in MIBK for 30 seconds and rinsed with IPA for 30 seconds. Subsequently, 3 nm of chromium and 25 nm of gold were deposited, with the chromium layer enhancing gold adhesion to the glass substrate. Lastly, the sample was left in an acetone bath for approximately 5 h, followed by light ultrasonic agitation for 2-min to remove the undeveloped resist.

The exposure was performed with a base dose of 1000 μC/cm^2; the right- and left-handed L-shaped particles were exposed with a dose factor in the range 1.6 to 1.8, while the remaining antennae required slightly higher dose (1.7-1.9) [125].

Examples of the fabricated shapes are shown in Fig. 4.7.

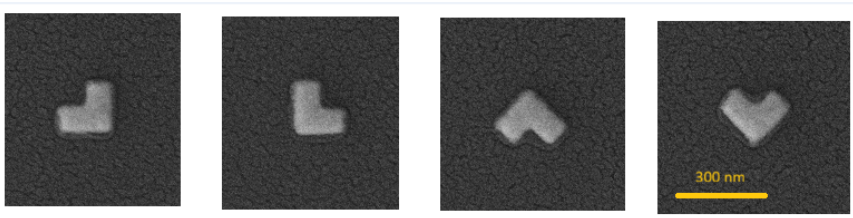

FIGURE 4.7: SEM images of fabricated L-shaped gold nanoparticles with different orientations.

4.5 Experimental Setup

The experimental setup consists of two parts: linear and nonlinear measurements.

4.5.1 Linear Measurement Setup

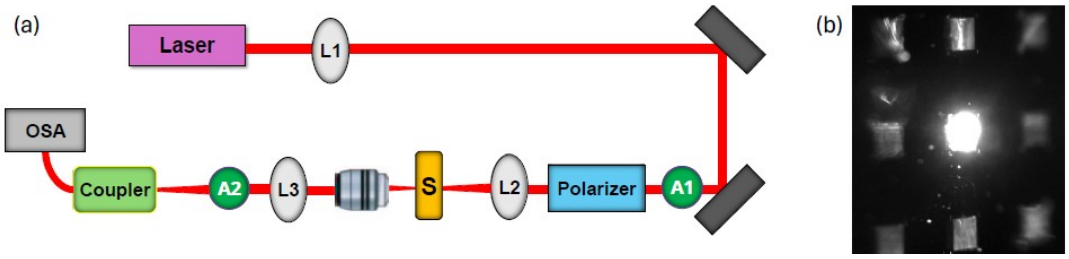

FIGURE 4.8: (a) Schematic of the linear experimental setup used to measure the transmission spectrum. (b) Focused light on the fabricated sample at the fundamental wavelength.

The schematic of the linear setup is shown in fig. 4.8. A broadband supercontinuum laser source was used to measure the transmission resonances of the sample. The diverging light from the source was first collimated using lens L1, and then directed along the main optical axis using two mirrors (M1 and M2). A polarizer was placed after the mirrors to fix the polarization state of the incident light. Two apertures (A1 and A2) were used to ensure that the beam propagated precisely along a straight path.

The collimated beam was then focused onto the sample using lens L2 with a focal length of 5 cm, ensuring that the light covered the entire sample area

and provided a high signal-to-noise ratio. The transmitted light was subsequently collected and collimated by a microscope objective with a focal length of 1.7 cm. Finally, the collimated transmitted light was coupled into a fiber coupler and directed to an optical spectrum analyzer (OSA) to record the transmission spectrum.

4.5.2 Nonlinear Microscopy Setup

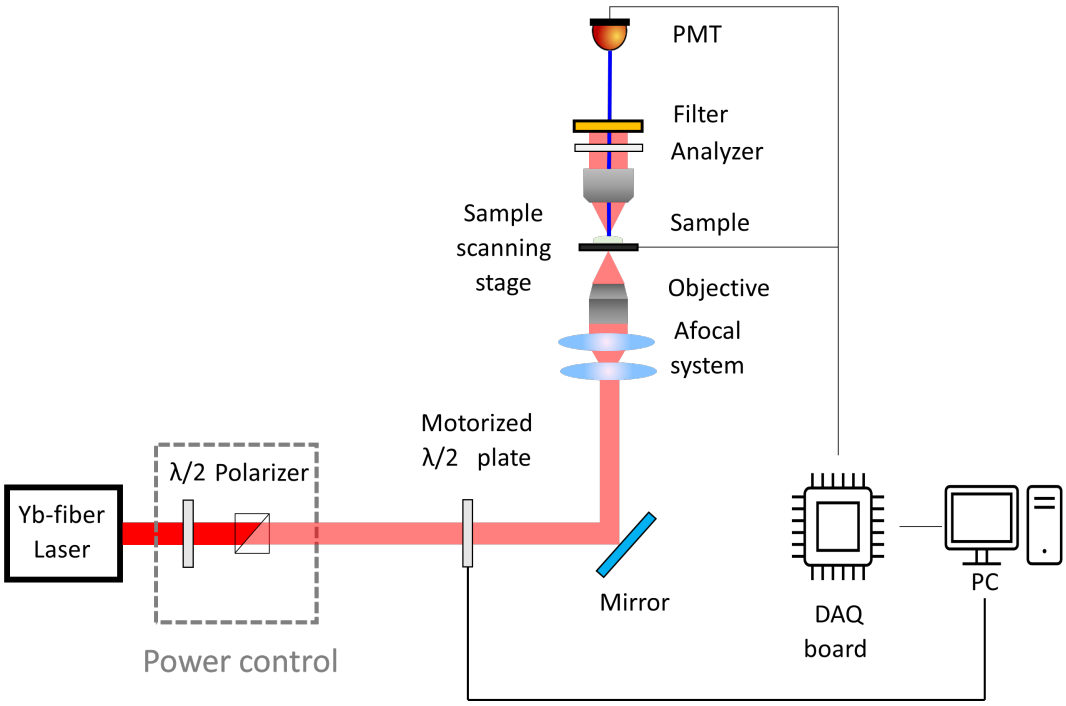

FIGURE 4.9: The imaging setup for the SHG microscopy.

The home-built SHG microscope used to capture the SHG signal from the samples (fig. 4.9) consists of a Yb fiber laser source (MPB Communications Inc., Montréal, CA) with a 125 fs pulse duration, 1030 nm wavelength, and 25 MHz repetition rate, producing average powers of up to 3 W. Furthermore, a power control unit combining a half-wave plate and Glan-Thompson polarizer regulated the average output power to prevent sample damage. A power range of 30 mW (1.2 nJ pulse energy, respectively) was used at the objective focus. A 40× objective (UplanSApo, Olympus, Japan) with a 1.0 NA was used to illuminate the sample. The sample was stacked on a high-speed motorized XY stage (MLS203; Newton, NJ, USA) to scan an average area of $600 \times 600\ \mu m^2$.

To optimize the focus of the sample, the distance from the objective was varied along the z-axis using mechanical and piezoelectric motors (PI Nano-Z, USA) for coarse and fine adjustment. The fundamental and SHG signals from the sample were collected using a 0.5 NA condenser. The collected SHG signal was isolated using a multi-stage filtration process, including two short-pass filters (Semrock, 720 nm blocking edge, short-pass filter out the fundamental laser light) and a band-pass filter (Semrock, 515/30 nm band-pass filter). Image acquisition was synchronized using a multichannel I/O board and photomultiplier tube (R6357, Hamamatsu Photonics).

To investigate the polarization dependence of the SHG signal, a motorized half-wave plate (HWP) was inserted into the laser path (fig. 4.9). The SHG images were acquired at distinct linear polarization orientations (S-polarization, P-polarization) by rotating the HWP accordingly.

The custom Python program provided a user interface for adjusting the imaging area and pixel size. The acquired images were analyzed and compared using the Fiji-ImageJ software.

4.5.3 Experimental conditions

The columnar and uniform metasurfaces each had a patterned area of 400 μm $\times$ 400 μm and contained 228,000 and 200,000 nanoparticles, respectively. The linear transmission measurements probed the full patterned area, while each position in the SHG scan probed a small region of the array. The estimated focal spot diameter in the SHG measurements was 1.3 μm. The average pump power was set to 30 mW before the focusing objective to obtain a detectable SHG signal while avoiding sample damage during scanning.

4.5.4 Experimental repeatability and sample variation

Measurements were repeated under the same experimental conditions for each configuration and were also performed on independently fabricated

samples of each metasurface design. Comparing repeated measurements allowed us to assess the consistency of the measurement procedure, while comparing samples of the same design allowed us to examine how reproducibly the spectral response was obtained across fabricated samples. In both comparisons, we looked for recurring patterns in the spectra, with particular attention to the resonance wavelength, quality factor, and transmission amplitude.

The spectra showed good agreement across repeated measurements and across samples of the same design, with minor differences in these quantities. The shifts in resonance wavelength were small relative to the linewidth of the broad plasmonic resonance. The pump wavelength therefore remained within the resonance band, where the local field enhancement supports second-harmonic generation. A larger shift would warrant checking the measurement conditions and inspecting the sample for possible damage, particularly if the shift moved the resonance away from the pump wavelength. The agreement across measurements and samples supports the reproducibility of the spectral features used to interpret the nonlinear response.

4.5.5 Data processing

In the nonlinear measurements, the transmitted second-harmonic signal was recorded as the focused beam scanned the sample line by line. The resulting maps included both the metasurface and the surrounding silica substrate, allowing the signals from the two regions to be compared within the same scan. The maps were processed in Fiji to reduce noise, normalize the image intensities, and improve contrast between the metasurface and substrate regions. The substrate region served as a reference for evaluating the background signal in the SHG maps.

In the linear measurements, spectra were acquired through the metasurface region, through air with the sample removed, and through an unpatterned region of the same silica substrate. We compared the results obtained with air and substrate references to examine how the choice of reference affected the transmission spectrum. With air as the reference, the normalized spectrum

includes the optical response of the silica substrate. Using the substrate as the reference accounts for its contribution and can reduce artifacts from dust or other unwanted scattering when their effects are common to both measurements. The substrate-normalized transmission was therefore calculated at each wavelength by dividing the signal measured through the metasurface region by the signal measured through the substrate region. This ratio gives the transmission of the patterned region relative to that of the substrate.

4.6 Results

In fig. 4.10, the transmission spectrum of the metasurface with the central particle oriented at -60° exhibits a pronounced dip at 1100 nm (FH), with distinct spectral features under x- and y-polarized excitation, while a corresponding peak is observed in the nonlinear transmitted power spectrum.

Comparison of the nonlinear transmitted powers in Fig. 4.10 and Fig. 4.3 reveals that, for both x- and y-polarized excitation, the five-particle metasurface exhibits an SHG enhancement exceeding a factor of 3.3 relative to the single-particle configuration. For each of the two pump polarizations, a simulated enhancement factor of 3.3 was obtained at a pump wavelength of 1.1 μm by dividing the transmitted second-harmonic power per unit cell of the five-particle metasurface by that of the reference metasurface with one particle per unit cell. This pronounced increase arises from two main mechanisms. First, incorporating multiple nanoantennas within each unit cell increases the number of active nonlinear emitters contributing to the SHG process. Under x-polarized excitation, two particles are strongly excited within each period, which alone would be expected to yield an enhancement approaching a factor of two compared with the single-particle case. Second, near-field coupling between neighboring particles further enhances the local electric field, driving the nonlinear response well beyond this value.

A similar trend is observed under y-polarized excitation, where the central particle oriented at -60° acts as the dominant nonlinear emitter. Although only one particle contributes strongly to the emission in this case, near-field coupling within the unit cell substantially increases the local field intensity,

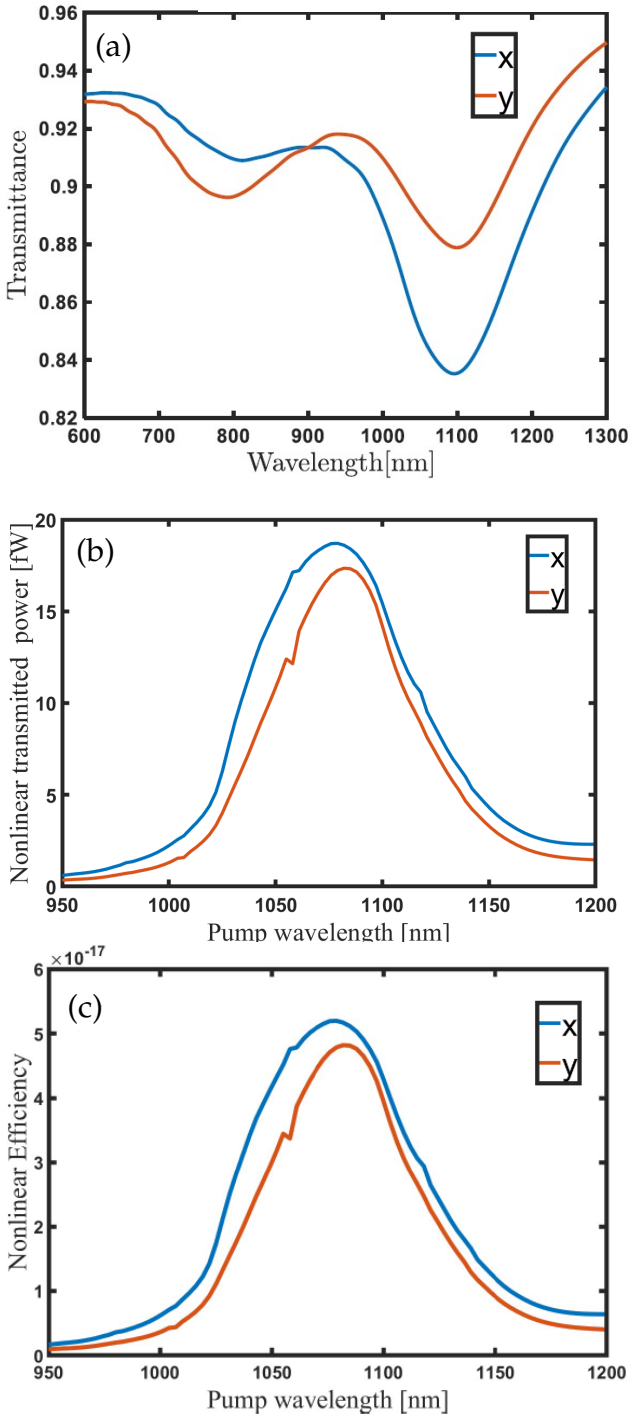

FIGURE 4.10: (a) Simulated transmission spectra under x- and y-polarized excitation for the sample with a middle particle oriented at $-60°$. (b) Corresponding simulated far-field transmitted second-harmonic (SHG) power for both polarizations. (c) Corresponding simulated nonlinear conversion efficiency for both polarizations.

resulting in an overall SHG enhancement greater than 3.3 relative to the single-particle metasurface.

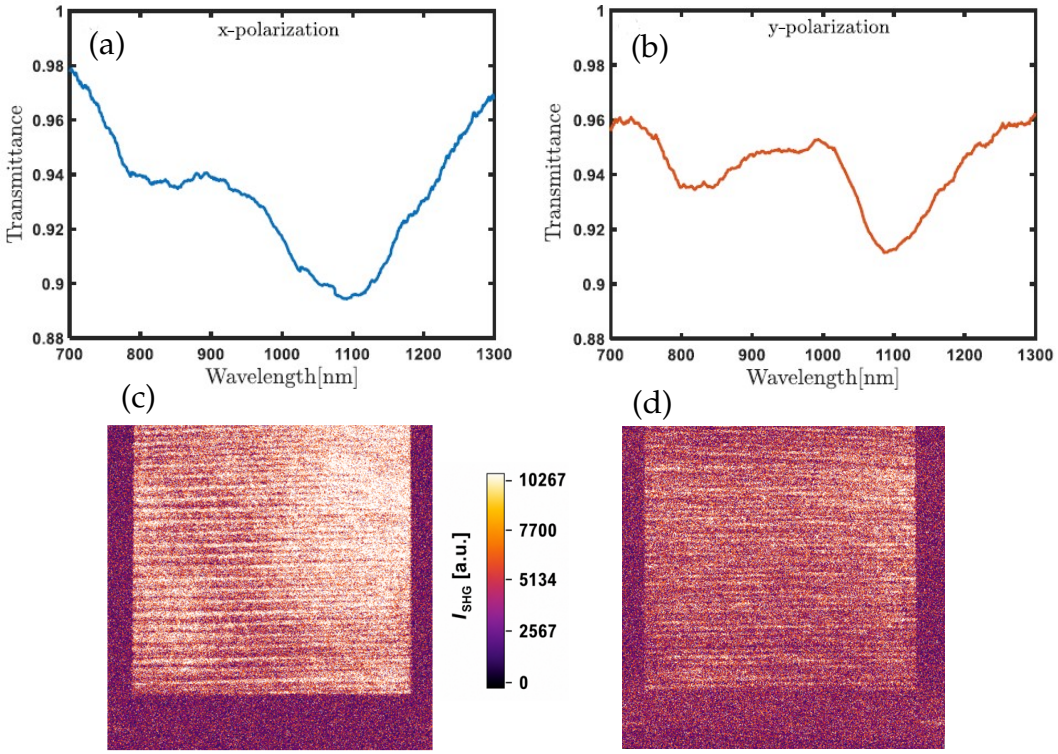

FIGURE 4.11: (a) and (b) Experimental transmission spectra for x- and y-polarized excitations, respectively. (c) and (d) near-field SHG image acquired experimentally at 515 nm wavelength under x- and y-polarized excitation, respectively.

The good agreement between the measured transmission spectrum figure 4.11 and the numerical simulation figure 4.10 further confirms the validity of the theoretical model. The SHG image obtained under x-polarized excitation is brighter than that under y polarization, in agreement with the simulation results. Moreover, the simulation results enable estimation of the dominant nanoparticle orientation under each excitation polarization: the V-shaped particle under x polarization, with a weaker contribution from the left-handed L-shaped particle due to near-field interactions, and the 60°-oriented particle under y polarization, with a weaker contribution from the right-handed L-shaped particle due to near-field interactions.

In figure 4.11, the fabricated sample is a metasurface in which each unit cell consists of five gold nanoparticles, with the middle particle oriented at -60° on a silica substrate. The metasurface has dimensions of 400 μm × 400 μm.

The SHG images exhibits an almost spatially uniform intensity distribution for both x- and y-polarized excitation, as expected for a large-area periodic structure consisting of approximately 40000 identical unit cells. Since each unit cell contains at least one nanoparticle contributing to the nonlinear response, a nearly uniform SHG emission across the sample surface is expected. As shown in figure 4.11 (c) and (d), the darker regions correspond to the glass substrate, while the brighter regions correspond to the fabricated sample, which emits SHG over its entire area.

For x-polarized excitation, some regions of the sample appear slightly brighter than others. However, this spatial variation is weak and can be considered negligible. It is most likely associated with unavoidable fabrication errors and experimental imperfections, rather than an intrinsic difference in the optical response.

In addition, thin dark strips are visible in the SHG images for both polarizations. These features are attributed to the measurement process rather than the intrinsic properties of the sample. The microscope objective used in the experiment had a numerical aperture (NA) of 1, which, at the pump wavelength of 1030 nm, produces a focused spot size of approximately 1.3 μm on the sample surface. This spot size is smaller than the unit-cell dimensions.

During the measurement, the focused beam was scanned line by line across the sample, first along the horizontal direction and then incrementally shifted along the vertical axis. Because this displacement along the y-direction is not perfectly continuous, small uncovered gaps may remain between adjacent scan lines, leading to the appearance of the thin dark strips observed in the SHG images.

We now introduce a second sample that allows for better experimental visualization of these behaviors. In this design, the structure is periodic only

along the x-direction, while the particle orientation remains unchanged along y. Specifically, each period consists of 25 columns and 480 rows, and there are 19 periods along the x-direction, as shown in figure 4.14. Each group of five columns corresponds to a different particle orientation. For example, the first five columns correspond to right-handed L-shaped particles. As a result, a nonuniform pattern is expected in the corresponding SHG image, making it more suitable for validation.

In simulation, modeling the full structure is nearly impossible because it is non-periodic and contains approximately 228000 particles. Therefore, we simplified the model by considering only five rows and five columns (each orientation one columns). In the fabricated sample, the spacing between adjacent particles is 1 μm along both x and y. In the simulations, we examined spacings of 1 μm and 2 μm to investigate the effect of particle separation.

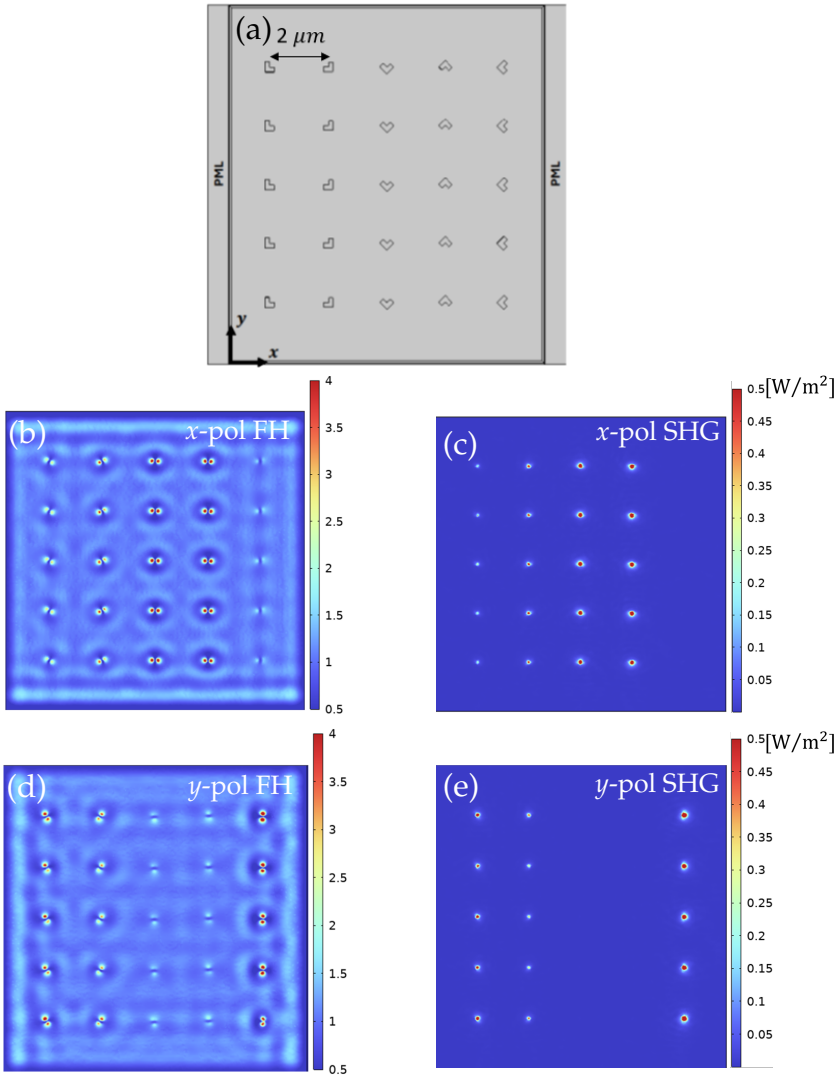

FIGURE 4.12: (a) Geometry of the simulated structure. (b) and (d) show the corresponding simulated linear intensity distributions at a height of 50 nm above the surface for x- and y-polarized excitation, respectively. (c) and (e) show the corresponding simulated nonlinear intensity distributions for x- and y-polarized excitation, respectively.

Figure 4.12 shows the simulated array and the corresponding intensity distributions. In this configuration, a separation of 2 μm suppresses near-field coupling, leading to emission from isolated particles.

When the interparticle spacing is reduced to 1 μm, the overall spatial intensity distribution remains qualitatively unchanged, with the columns aligned with the incident polarization continuing to dominate the response, as shown

in figure 4.13. However, a pronounced enhancement of the local field intensity is observed at the particle locations as the periodicity decreases, indicating the onset of constructive near-field coupling within each column [145]. Therefore, reducing the spacing to 1 μm promotes constructive interactions among particles within the same column and improves the spatial resolution compared with the 2 μm spacing case.

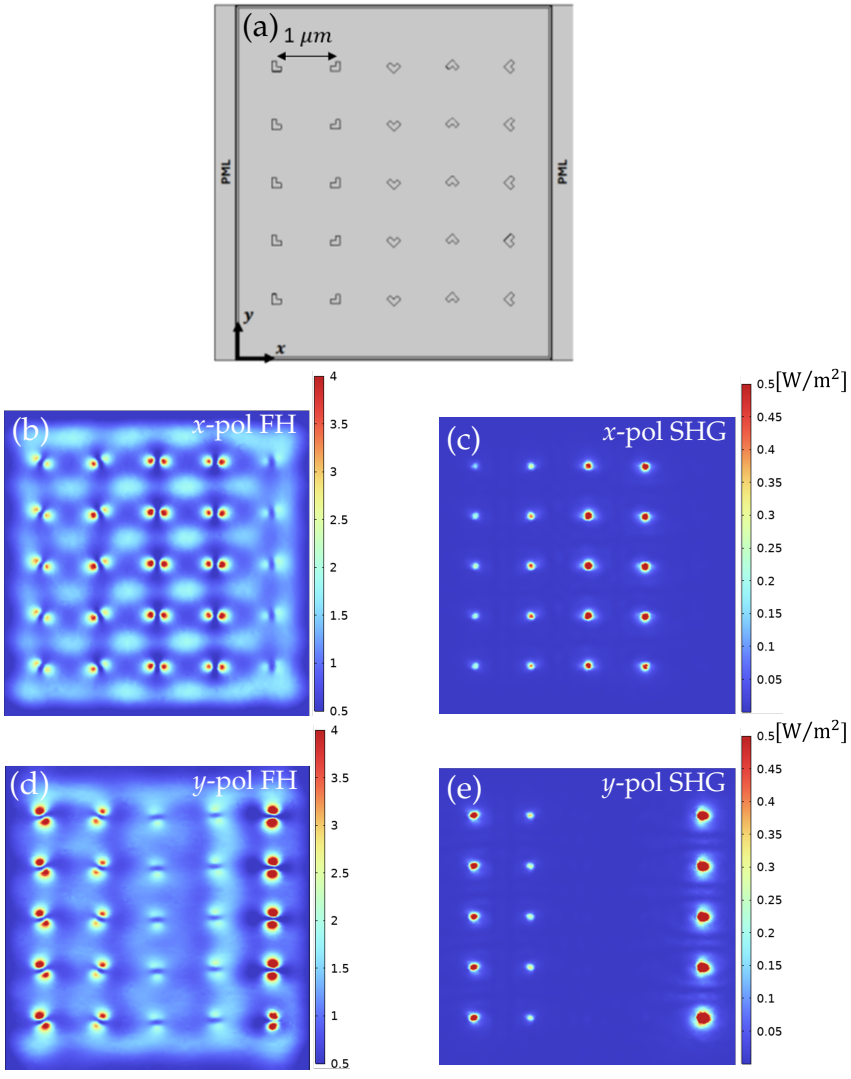

FIGURE 4.13: (a) Geometry of the simulated structure. (b) and (d) show the corresponding simulated linear intensity distributions at a height of 50 nm above the surface for x- and y-polarized excitation, respectively. (c) and (e) show the corresponding simulated nonlinear intensity distributions for x- and y-polarized excitation, respectively.

For both spacings, the brightness is nonuniform and strongly depends on the correlation between particle orientation and the incident polarization. Some columns appear bright, others less intense, and some remain nearly dark. For x-polarized excitation, only the particles oriented at -45° (the last column) remain effectively unexcited, while the V-shaped structures exhibit significant interactions. In contrast, for y-polarized excitation, the upward- and downward-oriented V-shaped columns are largely suppressed, while the L-shaped structures remain active and the -45° particles exhibit the strongest response, appearing as the brightest regions. As a result, the x-polarized case produces a narrower dark strip, with the brightness of the adjacent bright regions gradually decreasing from the center toward the corners, whereas the y-polarized case shows a wider dark strip.

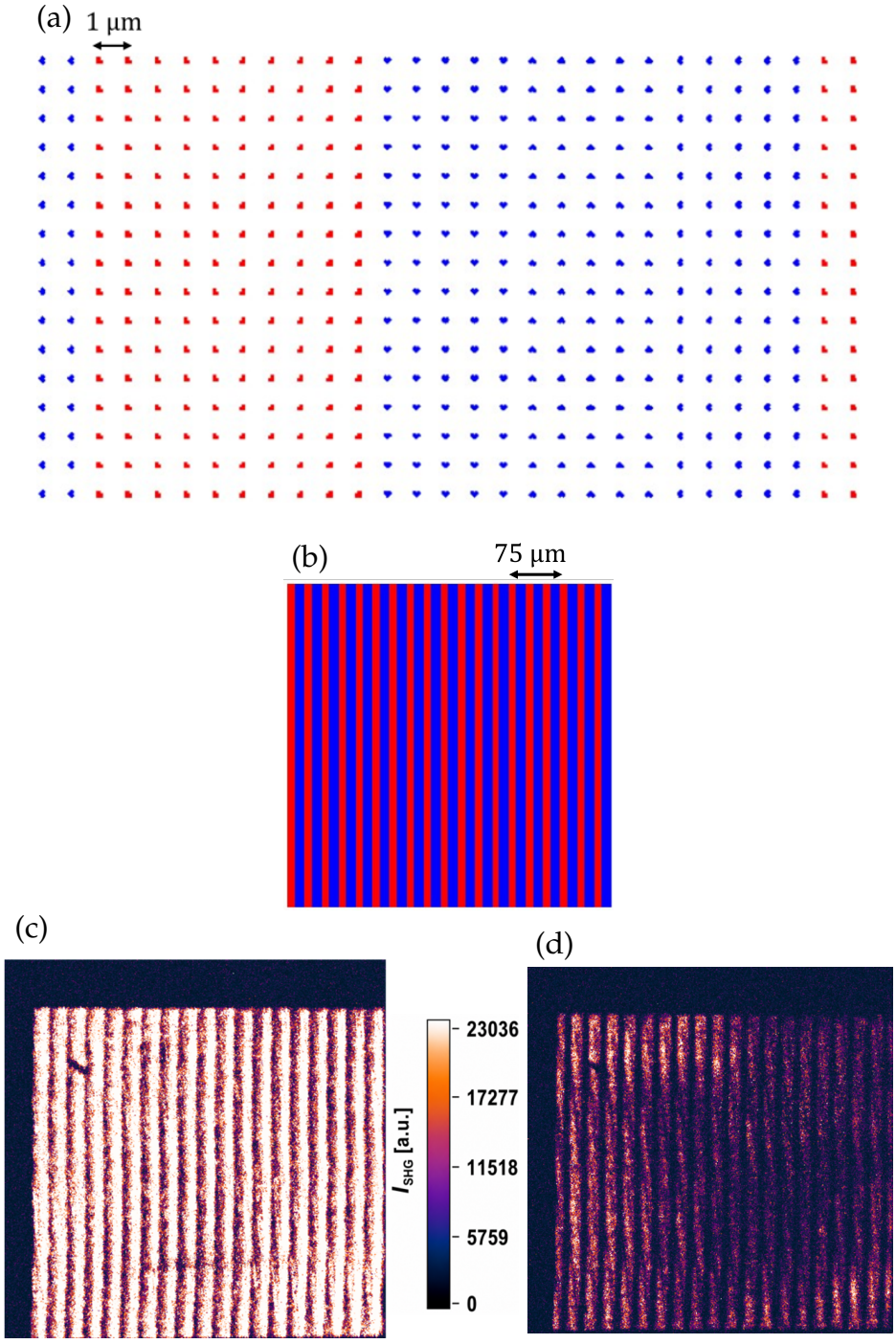

FIGURE 4.14: (a) and (b) show the fabricated sample with a spacing of 1 μm. (c) and (d) show the corresponding experimentally measured SHG images at the wavelength of 515 nm under x- and y-polarized excitation, respectively.

Distinct bright and dark strip patterns are clearly visible in Fig. 4.14 (c, d). Unlike the previous sample containing five particles per unit cell, which exhibited a nearly uniform intensity distribution, this structure displays a pronounced striped pattern. Moreover, the overall pattern and differences observed between x- and y-polarized excitation are in good agreement with the simulation results and the physical interpretation discussed above. For example, the image obtained under x-polarized excitation exhibits narrower dark regions and wider bright regions, where the intensity gradually decreases from the center toward the edges of each strip. In contrast, the image under y polarization shows wider dark regions and a sharper transition from bright to dark areas. In addition, both x- and y-polarized images display 19 strips, consistent with the fabricated structure. This agreement also enables estimation of the dominant orientation within each column. Under x-polarized excitation, the brightest columns correspond to V-shaped particle orientations, whereas the darkest columns correspond to particles oriented at -45°. Under y-polarized excitation, this trend is reversed, with the -45° orientation producing the brightest columns and the V-shaped orientation producing the darkest.

4.7 Conclusions

In this work, we exploit localized surface plasmon resonances (LSPRs) to model the nonlinear response of artificial biomolecules, which is sensitive to their spatial arrangement and geometrical properties. This capability is demonstrated using a columnar metasurface, where the orientation of the columns can be identified from the near-field SHG intensity distribution. Building on our understanding of the nonlinear response of a single L-shaped particle for different excitation polarizations and orientations, we extend the design to unit cells containing five differently oriented particles. This enables the study of interacting polar biomolecules with greater structural complexity while simultaneously increasing the number of active nonlinear emitters and investigating the effect of near-field coupling on the local field distribution. As a result, the overall nonlinear response exhibits an enhancement exceeding 3.3× compared with the single-particle metasurface. Together, these

findings highlight the potential of plasmonic metasurfaces, through LSPR-assisted field confinement and constructive near-field interactions to enable enhanced, polarization-independent SHG imaging and the retrieval of structural information, including the polarity and orientation of biomolecules, in complex biological networks.

Beyond this work, nonlinear phase-front analysis in the far field could provide a powerful route for extracting the orientation and density of biomolecules. Since each particle orientation imparts a distinct nonlinear geometric phase to the generated harmonic field, the collective emission encodes this information in the spatial phase profile of the wavefront, providing direct insight into the underlying structural organization.

Moreover, although the particles in this work predominantly exhibit an electric dipolar response, nanostructures in general can support higher-order modes, such as magnetic dipoles and electric quadrupoles, depending on their size, geometry and excitation wavelength. Incorporating these multipolar contributions in the design introduces additional degrees of freedom for engineering the nonlinear response, potentially enabling further improvements in imaging resolution.

Funding

Natural Science and Engineering Research Council of Canada, Discovery and Alliance funding programs, the Canada Research Chairs program.

Acknowledgments

The authors gratefully acknowledge the use of the University of Waterloo's QNFCF facility and the University of Ottawa's NanoFab facility in support of this work. This infrastructure would not be possible without the significant contributions of CFREF-TQT, CFI, ISED, the Ontario Ministry of Research & Innovation and Mike & Ophelia Lazaridis.

Chapter 5

Bi-Layered Stack Plasmonic Metasurface for High-Resolution Near-Field SHG Microscopy Applications

5.1 Introduction

In previous chapters, we first modeled the natural polar arrangement of biomolecular structures using asymmetric plasmonic meta-atoms periodically or randomly distributed in an array, and then employed the second-harmonic field to track their polarity and resolve their geometrical features. Although we were able to model the biomolecular arrays, successfully detect the SHG signal, and use it for our purposes, the relatively low photon count and weak signal strength remain important limitations. This is particularly relevant when modeling biological structures, as many biomolecular systems exhibit weak, although detectable, nonlinear optical responses when excited in the visible and near-infrared spectral ranges [149], [150]. In this context, metasurfaces could serve as artificial platforms for modeling the optical response of such natural structures. However, beyond their ability to model natural systems, one of the main applications of metasurfaces is their capability to enhance both linear and nonlinear optical emissions [151], [152]. For this purpose, various designs have been explored to enhance the forward emission and near-field resolution of SHG in plasmonic metasurfaces under excitation in the visible and near-infrared spectral ranges [26], [153], [154], [155].

One common approach for enhancing SHG is to employ periodic or random arrays of non-centrosymmetric plasmonic nanostructures engineered to support localized surface plasmon resonances (LSPRs) at the fundamental wavelength. The resulting local-field enhancement can significantly strengthen the nonlinear response, since, under the perturbative and undepleted-pump approximations, the nonlinear polarization depends on powers of the local fundamental field. Various geometries, including L-, T-, U-, and G-shaped plasmonic nanoparticles, have been investigated for this purpose [26], [120], [147], [156]. However, LSPR-based metasurfaces generally exhibit relatively low quality factors due to intrinsic Ohmic and radiative losses, limiting energy accumulation and consequently the SH emission intensity.

Another approach is to employ surface lattice resonance (SLR)-based metasurfaces. As discussed in the previous section, SLRs can be achieved through an appropriate choice of array periodicity and engineering of the lattice interactions. These collective resonances typically exhibit high quality factors and relatively low losses, resulting in strong local-field enhancement at the fundamental wavelength and, consequently, enhanced nonlinear field generation [139], [157], [158], [159]. However, maintaining a high-Q SLR generally requires a thick, index-matched dielectric cladding. Such an environment can confine a significant portion of the generated SH wavevector components within or along the metasurface plane, thereby limiting their coupling to free-space radiation channels. Consequently, despite the enhanced nonlinear generation, the forward-emitted SHG signal can remain moderate. More importantly for microscopy applications, this confinement can degrade the near-field spatial resolution and obscure local polarity variations that are essential for resolving subwavelength features [154].

Other design strategies combine multiple resonance mechanisms to achieve stronger field enhancement, such as doubly resonant structures, in which resonances are simultaneously supported at the fundamental and second-harmonic wavelengths, leading to a substantial enhancement of the nonlinear signal [160], [161], [162]. Although these approaches are highly effective in boosting nonlinear field generation, additional considerations arise when they are employed for microscopy applications. For example, the near-field

dynamics around adjacent nanostructures must preserve the spatial distribution of the nonlinear field so that subwavelength geometrical features and local variations can still be resolved. Furthermore, efficient detection requires that the enhanced nonlinear field not remain solely confined near the nanostructures, but instead couple efficiently to radiative modes and propagate into the far field.

In this chapter, we aim to address this challenge by proposing an approach to enhance the generation and far-field coupling of the nonlinear field while preserving the local spatial resolution and dipolar field distribution at resonance. To demonstrate the evolution of the design, we begin with a metasurface composed of unit cells containing a single asymmetric V-shaped gold antenna supporting an LSPR at a wavelength of approximately 1050 nm. Similar to the structures considered in the previous chapters, this metasurface represents an artificial model for the concentration of biomolecules. In the next step, we consider a V-shaped metasurface with the same antenna geometry but embedded within a thick cladding layer, allowing it to support a surface lattice resonance (SLR) at the pump wavelength. We then investigate how the SLR affects the far-field emission and near-field resolution at the SHG wavelength.

Considering the limitations of these designs, we propose a new configuration aimed at significantly improving the microscopy process. This configuration consists of a stacked metasurface incorporating an SLR-supporting metasurface that contributes only to the linear optical response, coupled to an LSPR-based metasurface that acts as the biomolecular layer. We investigate the optical response of each layer separately, as well as that of the complete stacked configuration. This work provides a practical approach for simultaneously enhancing the near-field spatial distribution and far-field signal strength, while also providing a fundamental study of the trade-off between field enhancement and far-field coupling.

This project was conducted through a collaboration between our group, the Nonlinear Photonics Group, and Prof. Lora Ramunno's group at the University of Ottawa. The main idea was proposed by Dr. Sina Aghili, a former

PhD student in our group, during a joint meeting between the two groups. He proposed improving the resolution of the microscopy platform presented in the previous chapter and performed the initial simulations to identify suitable design configurations. My specific contributions included assisting with the extensive simulations and optimization under the supervision of Professor Dolgaleva and through discussions with Dr. Aghili, particularly in designing the SLR-based metasurfaces and optimizing the separation between the two layers. I also contributed to writing the corresponding paper [123] and preparing responses to the reviewers' comments.

5.2 Methodology

The numerical analysis of these structures can be divided into two main parts, as discussed in the previous section. First, linear simulations are performed using the finite-difference time-domain (FDTD) method implemented in Lumerical. These simulations are used to characterize the resonant behavior of the metasurface, obtain its transmission spectrum and quality factor, and helps us to identify the nature of the resonances, such as LSPR, SLR, and Fano.

The nonlinear response is investigated using a combination of the hydrodynamic model, nonlinear scattering theory, and COMSOL simulations. As described in detail in Chapter 2, the local field at the fundamental wavelength is first obtained using COMSOL. This field is then used in the hydrodynamic model to determine the induced nonlinear current density. Finally, the generated nonlinear emission is evaluated using either nonlinear scattering theory or COMSOL.

5.3 Design and Results

The constituent element of the nonlinear metasurface, which represents an array of biomolecular structures, is chosen to be an asymmetric V-shaped gold nanoantenna. The non-centrosymmetric geometry allows a nonzero SHG response, while the two-arm configuration provides additional degrees of freedom for geometrical optimization and enables the excitation of LSPRs

over a broad range of wavelengths and incident polarizations [162], [163]. The dimensions of the V-shaped nanoantenna are therefore optimized such that the metasurface supports an LSPR within the near-infrared wavelength range.

The geometry of the optimized nanoantenna, together with its scattering cross section (SCS) under x- and y-polarization, is shown in Fig. 5.1. The multipolar decomposition of the SCS indicates a dominant electric-dipole contribution at both the pump and SHG wavelengths with the resonance occurring at approximately 750 nm for both incident polarizations. Additional multipolar contributions are also observed in the visible range for both polarizations, including a magnetic-dipole response associated with the bent geometry of the V-shaped antenna.

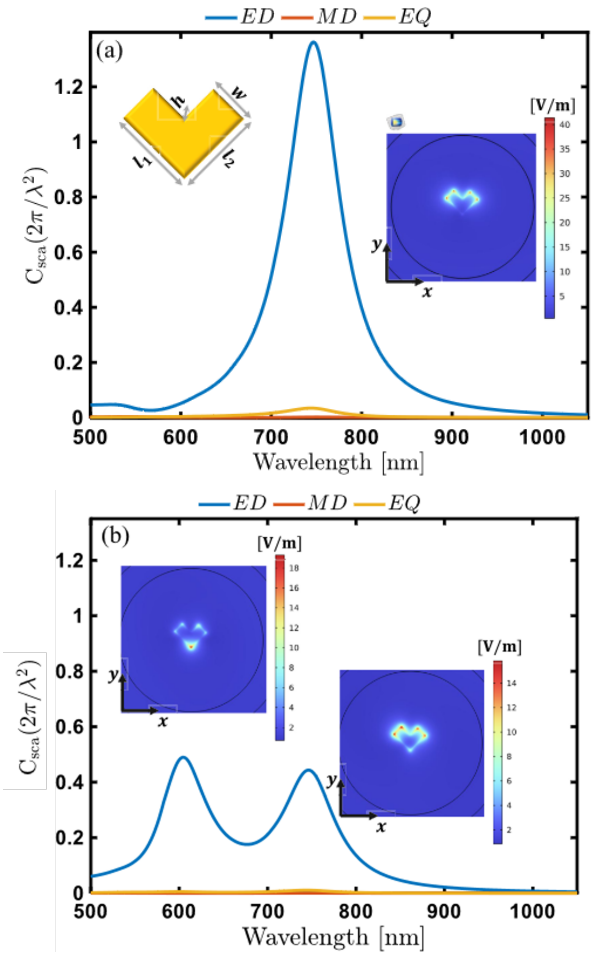

FIGURE 5.1: Particle configuration with dimensions $l_1 = 125$ nm, $l_2 = 115$ nm, $h = 30$ nm, and $w = 60$ nm, with an opening angle of 75°, together with the corresponding SCS and near-field profiles at the resonant wavelengths under (a) x- and (b) y-polarized illumination.

The first platform is a metasurface composed of the nanoantennas shown in Fig. 5.1. The LSPR can localize and enhance the electromagnetic field in the vicinity of the nanostructures, which can consequently enhance the nonlinear forward emission. The metasurface configuration and its transmission spectrum are shown in Fig. 5.2(a) and (b), respectively. The nanoantennas are periodically arranged on a silica substrate with lattice constants of $a_x = 600$ nm and $a_y = 800$ nm. These values are chosen to ensure that the interactions between neighboring particles in the lattice remain negligible. Silica with a refractive index of 1.45 is used as the substrate. The structure is illuminated with an x-polarized incident wave propagating along the z-direction.

The transmission spectrum exhibits a resonance at approximately 1050 nm, which is redshifted compared with the resonance of the single-particle configuration shown in Fig. 5.1 due to the presence of the substrate. The corresponding linear near-field distribution at the resonant wavelength is also shown in Fig. 5.2(b). Figure 5.2(c) presents the normalized forward-emitted SHG intensity, which exhibits a peak at the SHG wavelength, together with the corresponding nonlinear near-field distribution. Both the linear and nonlinear near-field profiles exhibit strongly enhanced and localized dipolar field distributions around the nanoantenna. This LSPR-based configuration is therefore used as the reference platform for comparison with the subsequent designs.

The next platform is an SLR-supported metasurface, in which we aim to couple the LSPR of the individual nanoantenna to the lattice resonance, thereby significantly increasing the Q factor and enhancing the local field. The SLR wavelength associated with the $(i, 0)$ diffraction order is given by [164]

$$\lambda_{\mathrm{SLR}}^{(i,0)} = a_y \left(\frac{n}{|i|} - \frac{\sin(\theta)}{i} \right), \tag{5.1}$$

where $i = 1$ corresponds to the first-order lattice resonance along the x-direction, n is the refractive index of the surrounding medium, and θ is the angle of incidence, which is set to zero in this study. To properly support the excitation and propagation of the lattice mode across the metasurface, a thick silica cladding layer with a thickness of 1 μm is also introduced.

Figure 5.3(a) shows the SLR-based metasurface. The nanoparticle geometry and lattice dimensions are identical to those of the LSPR-based structure presented in the previous section; however, in this configuration, the metasurface is embedded in a high index dielectric. Figure 5.3(b) presents the transmission spectrum, where multiple resonances appear due to the excitation of Fabry–Pérot modes within the thick cladding layer [165], [166]. Among these resonances, we focus on the narrow resonance near 1050 nm, which is close to the wavelength of interest and exhibits a quality factor of approximately 90. The corresponding near-field distribution shows strong field confinement around the antenna, arising from the excitation of the SLR.

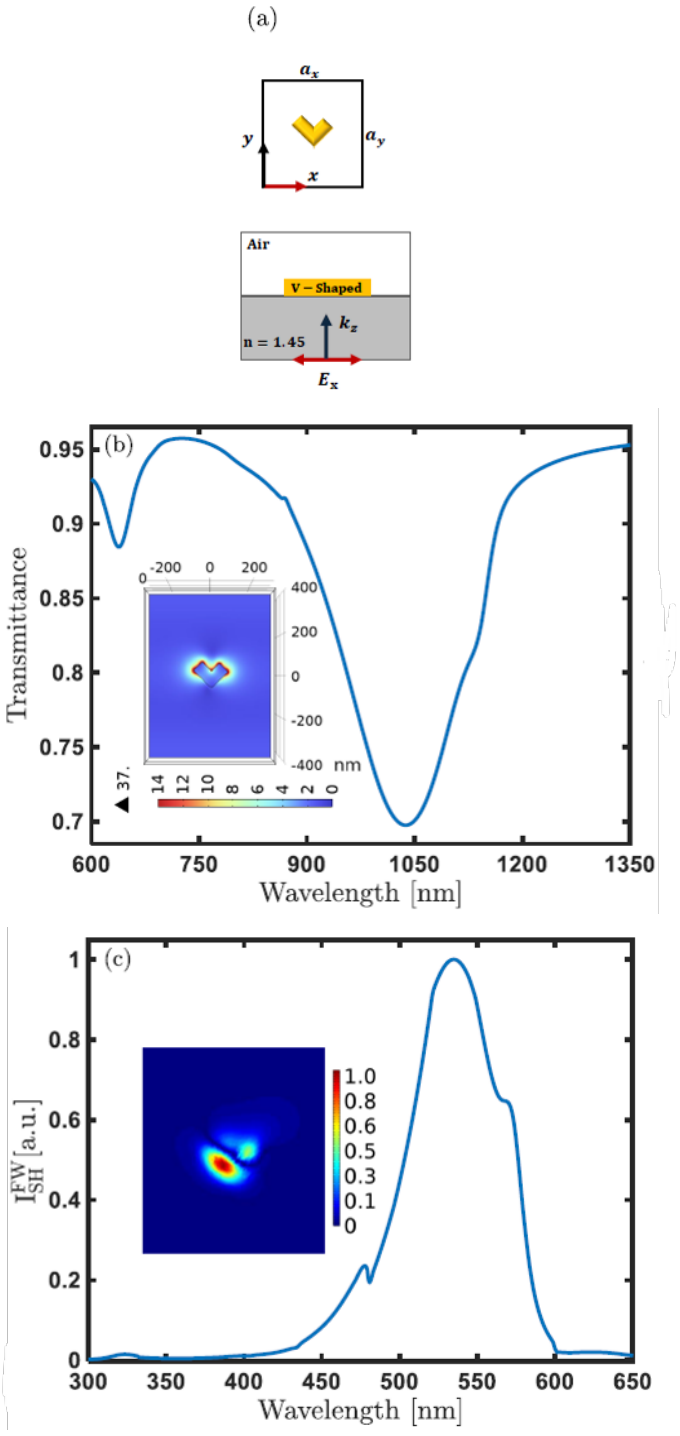

FIGURE 5.2: (a) Metasurface configuration. (b) Transmission spectrum together with the corresponding near-field distribution at the pump wavelength. (c) Forward-emitted nonlinear intensity together with the corresponding near-field distribution at the SHG wavelength.

The forward-emitted SHG spectrum is shown in Figure 5.3(c), where multiple peaks associated with the Fabry–Pérot resonances are also observed. Compared with the LSPR-based metasurface, the SHG peak intensity is enhanced by approximately a factor of 20, which can be attributed to the constructive lattice interaction at the SH wavelength of 525 nm. Despite this enhancement, the nonlinear near-field distribution reveals an important limitation of this configuration. Due to multiple reflections and propagation of the generated field within the cladd, the localized dipolar field distribution associated with individual nanoparticles is no longer preserved. Consequently, the subwavelength geometrical features of the metasurface become blurred, limiting its suitability for applications requiring high spatial resolution.

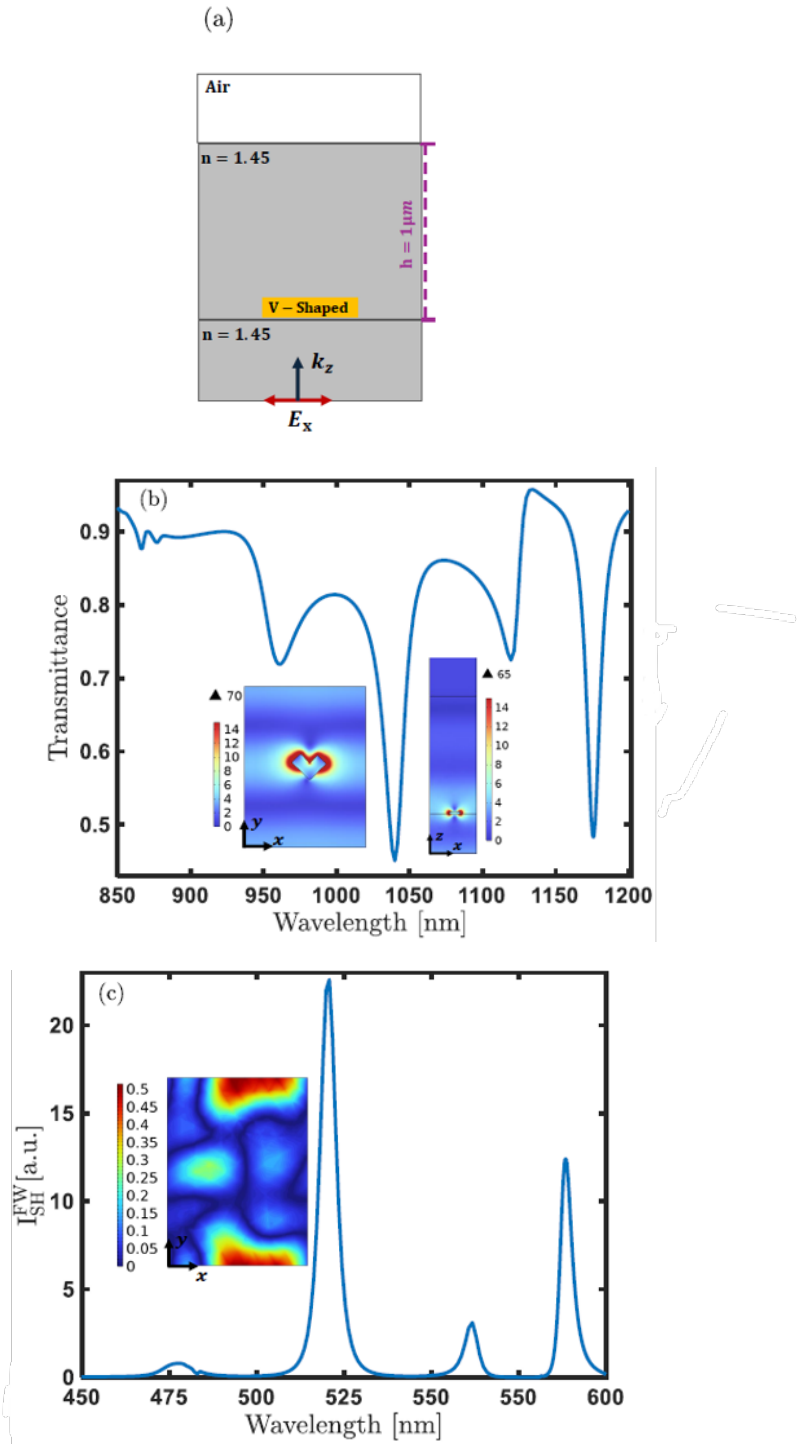

FIGURE 5.3: (a) Metasurface configuration. (b) Transmission spectrum together with the corresponding near-field distribution at the pump wavelength of 1050 nm. (c) Forward-emitted nonlinear intensity together with the corresponding near-field distribution at the SHG wavelength of 525 nm.

We now introduce the proposed stacked configuration by first examining each metasurface layer separately. The first layer is a linear SLR-supporting metasurface composed of rectangular gold nanobars. Owing to their centrosymmetric geometry, these nanobars do not contribute to the second-order nonlinear response. Instead, this passive metasurface serves as a linear field amplifier, supporting a collective resonance that significantly enhances the local electromagnetic field in the vicinity of the layer.

Figure 5.4(a) shows the configuration of this metasurface, with the same lattice constants as those used in the previous designs. Figure 5.4(b) presents the scattering cross section (SCS) of an individual nanobar, showing a dipolar resonance near 800 nm, together with the corresponding enhanced local-field distribution for an x-polarized incident wave propagating along the z-direction. When arranged periodically, the nanobars support an SLR at the pump wavelength, as observed in the transmission spectrum in Figure 5.4(c), with a quality factor of approximately 100. The associated near-field profile demonstrates the strong field enhancement produced by constructive lattice interactions.

The x-z veiw of field distribution in Figure 5.4(c) further allows us to estimate the spatial extent of the enhanced field away from the metasurface. Since the second layer must be positioned within this region to efficiently experience the enhanced field generated by the SLR layer, the interlayer separation should be maintained below approximately 350 nm.

We now combine the linear SLR layer with the LSPR-based V-shaped gold nanoantenna layer introduced in Figure 5.1, which represents the biomolecular layer. Their coupling is optimized by varying the silica spacer thickness, d, while maintaining the same excitation conditions as in the previous sections. As shown in Figure 5.5(a), the spacer simultaneously acts as the cladding for the SLR layer and the substrate for the V-shaped antennas.

Figure 5.5(b) presents the transmission spectra for $d = 200$ nm and 300 nm. Coupling between the two layers produces a Fano-type resonance in the near-infrared region, while the corresponding x-z field profile confirms strong

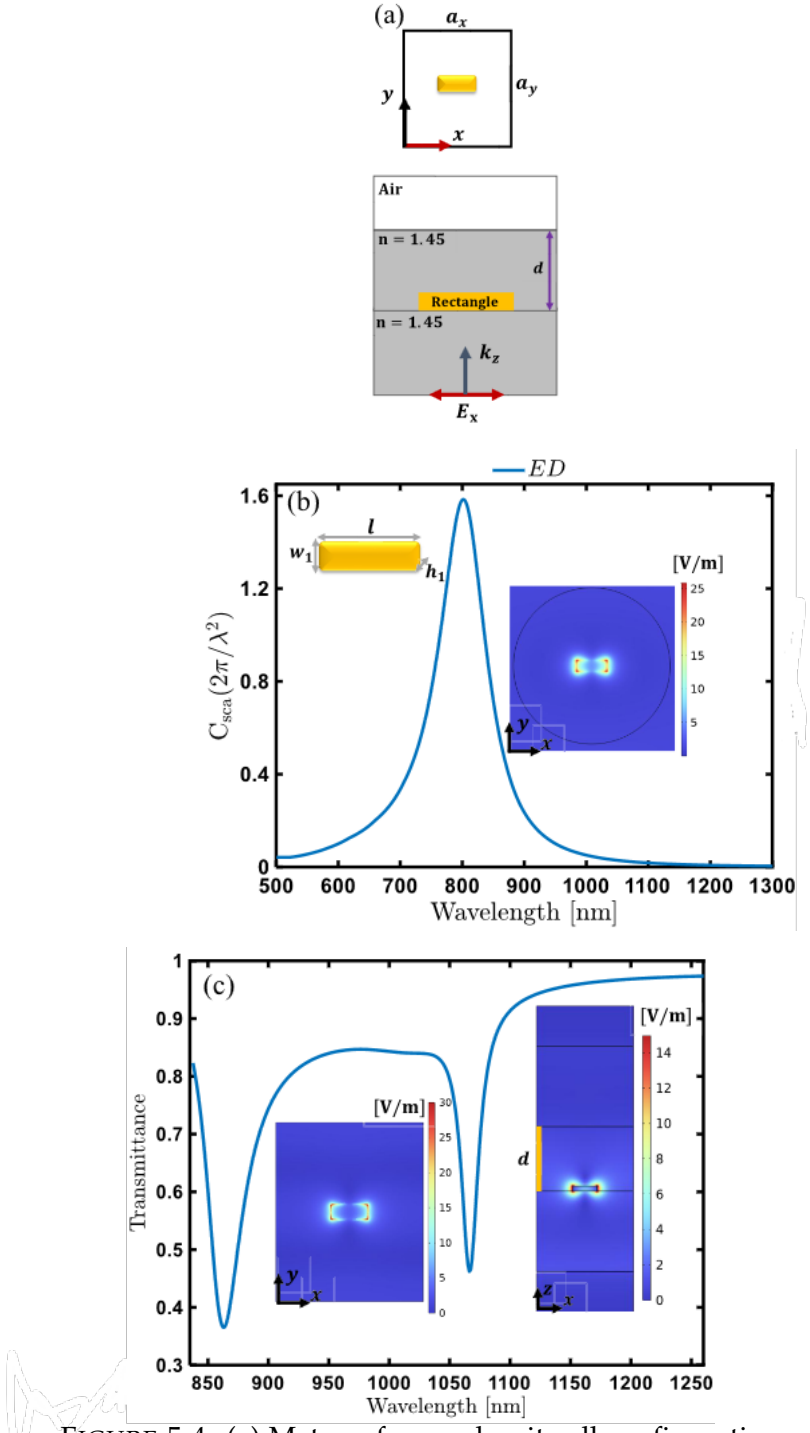

FIGURE 5.4: (a) Metasurface and unit-cell configurations, with nanobar dimensions of $l = 150$ nm, $h_1 = 30$ nm, and $w_1 = 60$ nm. (b) Corresponding scattering cross section (SCS) and near-field distribution at the resonant wavelength under x-polarized illumination. (c) Transmission spectrum and corresponding near-field distributions in the x-y and x-z planes at the pump wavelength of 1050 nm.

field localization across the structure. The forward-emitted SHG spectra in Figure 5.5(c) exhibit a peak at a pump wavelength of approximately 1100 nm for both separation distances. The response is considerably stronger for $d = 200$ nm, indicating more efficient coupling at this separation and resulting in an approximately 200-fold enhancement relative to the LSPR-based metasurface alone. More importantly, the nonlinear near-field profile retains the spatial field pattern of the V-shaped artificial molecule, allowing its subwavelength features to remain distinguishable despite the substantial increase in the SHG signal.

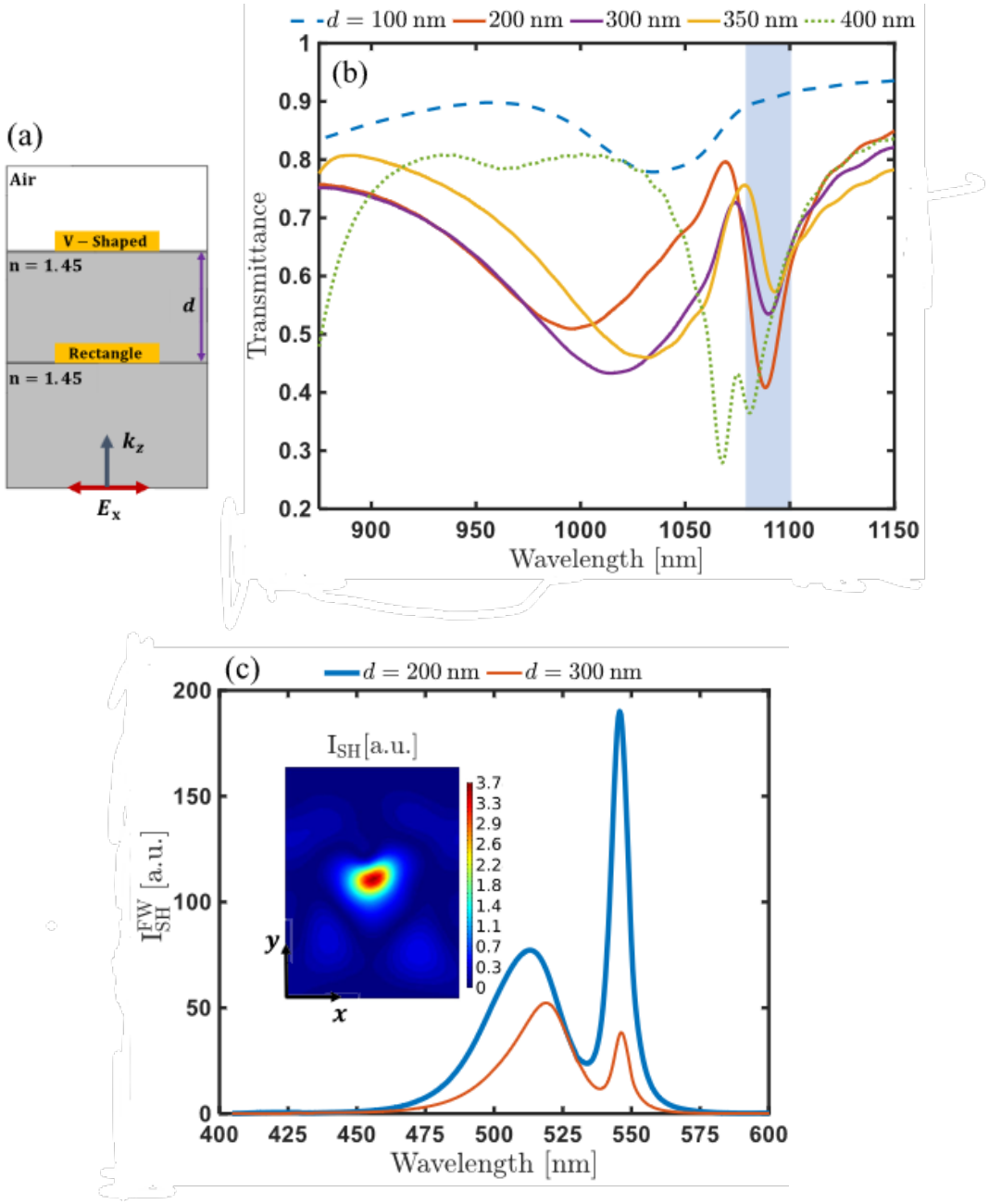

FIGURE 5.5: (a) Metasurface configuration. (b) Transmission spectra for $d = 200$ nm and 300 nm, together with the near-field distribution at the pump wavelength of 1100 nm for $d = 200$ nm. (c) Forward-emitted SHG intensity for $d = 200$ nm and 300 nm, together with the corresponding nonlinear near-field distribution at the SHG wavelength of 525 nm for $d = 200$ nm.

5.3.1 Lateral misalignment between the layers

Although the proposed bilayer device has only been studied numerically, alignment between the two layers is an important consideration for fabrication. To assess the effect of unintended lateral offsets, we performed a series of simulations in which the relative alignment of the layers was varied along the x and y directions. For the offsets tested, constructive coupling between the layers was maintained for displacements of up to 40 nm along either direction, and the forward SHG enhancement remained above a factor of 100. Larger offsets weakened the interlayer coupling and altered the SHG emission pattern.

5.3.2 Second-harmonic current density in the V-shaped nanoantenna

The enhanced nonlinear emission originates from the nonlinear current density induced at the surface of the V-shaped nanoantenna. To further investigate the contribution of the nonlinear current density to the SHG response, its individual components are plotted in Figure 5.6. The peak magnitudes of $|J_x^{\mathrm{SH}}|$, $|J_y^{\mathrm{SH}}|$, and $|J_z^{\mathrm{SH}}|$ are approximately 0.9, 1.8, and 1.2 a.u., respectively. Thus, the y-component has the largest amplitude, followed by the z-component, while the x-component has the smallest amplitude. The y- and z-components are mainly localized near the inner vertex of the V-shaped antenna, whereas the x-component is distributed primarily along its inner edges. These results indicate that the y-component is dominant in the induced nonlinear current density.

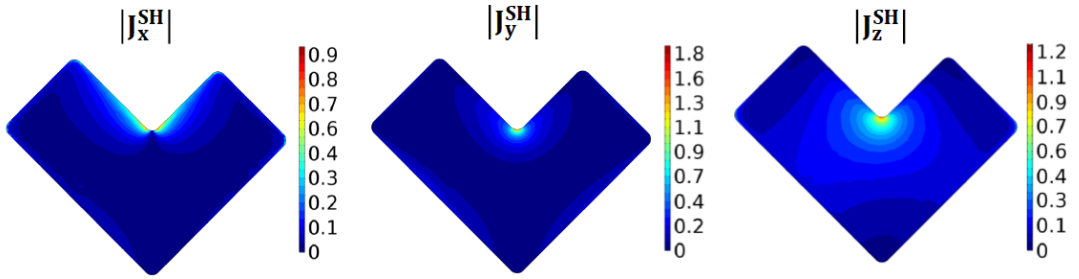

FIGURE 5.6: Different components of the current-density distribution across the V-shaped nanoantenna.

5.4 Conclusion

In this chapter, we compared three metasurface platforms for near-field SHG microscopy, aiming to enhance forward SH emission while retaining sensitivity to the subwavelength geometry of the nanoparticles. The first platform consisted of asymmetric V-shaped gold nanoparticles supporting an LSPR. Although this configuration produced only moderate forward emission, it maintained the characteristic near-field distribution of the nanoparticles.

We then investigated the same geometry under SLR conditions by introducing a thick dielectric cladding layer to support the Rayleigh anomaly and associated trapped surface waves. This configuration increased the forward SH emission by approximately 20 times. However, the cladding layer also behaved as a Fabry–Pérot cavity along the propagation direction, and multiple reflections within the layer distorted the spatial information of the nanoparticles, preventing clear recovery of their dipolar field distribution.

To overcome this limitation, we introduced a vertically stacked structure combining an LSPR-based metasurface, representing the biomolecular structure, with a linear SLR-based metasurface. Optimization of the separation between the two layers resulted in an approximately 200-fold enhancement of the forward SH emission while retaining the subwavelength geometrical information. The stacked configuration therefore provides an effective balance between nonlinear field generation, far-field coupling, and spatial resolution. Furthermore, analysis of the induced nonlinear current revealed that J_y dominates over J_x and J_z, providing insight into the origin of the SH response.

Overall, the proposed stacked architecture addresses the main limitations of the individual LSPR- and SLR-based platforms and provides a promising approach for high resolution near field SHG microscopy.

Chapter 6

Probing Geometry-Dependent Hyperpolarizability of Plasmonic Nanoparticles via SHG Spectroscopy

In the previous sections, we estimated the orientation of L- and V-shaped geometries with known optical responses and demonstrated that adding an external linear metasurface layer enhances forward emission, thereby improving microscopy resolution [123]. While this represents significant progress and highlights the capabilities of SHG microscopy and spectroscopy, the analysis has so far been restricted to structures with predefined geometries and well-characterized optical responses. A more general and practically relevant challenge is to determine whether the measured SHG response can be used to extract information about an unknown structure such as its geometry, orientation, or local symmetry [167].

One approach to addressing this challenge is to determine the hyperpolarizability tensor of the corresponding nanostructure, which represents the second-order nonlinear coefficient relating the induced nonlinear dipole moment to the square of the incident electric field [70]. Since the hyperpolarizability tensor is constrained by the symmetry of the particle, identifying its dominant components can provide useful information about the structural features of an unknown sample. This connection can be understood through

Neumann's principle, which states that the symmetry elements of any physical property of a crystal must include the symmetry elements of the crystal's point group [168]. In other words, a physical property must possess at least the same symmetry as the underlying structure, such that any symmetry operation of the structure leaves the corresponding physical property unchanged.

Inspired by this concept, we extended our study to a broader framework involving artificial molecular systems with more complex geometries. These structures were designed to exhibit LSPR in the visible spectral range, resembling the spectral region in which many chemical and biological molecules exhibit their characteristic optical responses. We numerically investigated their SHG emission and estimated the dominant elements of their hyperpolarizability tensors. Experimental characterization is planned to validate the numerical results. This study therefore establishes a connection between nanoscale structural characteristics and their nonlinear optical responses, providing a framework for probing the symmetry and subwavelength features of nanostructures through SHG measurements.

This project was conducted through a collaboration among our group, the Nonlinear Photonics Group; the Computational Nanophotonics Laboratory at the University of Ottawa, led by Professor Lora Ramunno; and the Joint Attosecond Science Laboratory (JASLab) at the National Research Council of Canada (NRC), led by Professor André Staudte. Our group contributed to the design and numerical analysis of the metasurfaces using commercial software, including Lumerical and COMSOL, as well as to their fabrication and linear and nonlinear characterization. The Computational Nanophotonics Laboratory contributed to the theoretical analysis and refinement of the designs and validated the numerical results using a homemade hydrodynamic-model code. The corresponding samples were fabricated by Dr. Lais Fujii dos Santos, a former postdoctoral fellow in our group, and Athulya Thulaseedharan, a PhD student in our group. JASLab provided the laboratory facilities, technical guidance, and assistance required for the nonlinear characterization. My specific contributions included designing and optimizing several

metasurfaces through numerical simulations under the supervision of Professor Dolgaleva. The designs were further developed through regular meetings with her and discussions with Professor Ramunno and Dr. Sina Aghili. Together with Dr. Aghili, I also contributed to the linear characterization in our laboratory at the University of Ottawa and to building and aligning the nonlinear experimental setup at JASLab with assistance from its researchers. The results presented in this chapter form the basis of a manuscript currently in preparation entitled "Probing Geometry-Dependent Hyperpolarizability of Plasmonic Nanoparticles via SHG Spectroscopy."

6.1 Methodology

6.1.1 Hyperpolarizability Calculation

To extract the hyperpolarizability of a particle from the nonlinear far-field power obtained either numerically or experimentally, we first assume that the optical response is dominated by a pure electric dipole. The magnitude of the effective nonlinear electric dipole moment can then be calculated as [120], [169]

$$|p|^2 = \frac{12\pi P_{\mathrm{NL}}}{n c_0^2 Z_0 k_0^4}, \tag{6.1}$$

where $|p|$ is the magnitude of the nonlinear electric dipole moment, P_{NL} is the far field nonlinear power, c_0 is the speed of light in vacuum, k_0 is the vacuum wavenumber at the second-harmonic frequency, Z_0 is the vacuum impedance, and n is the refractive index of the surrounding medium. The corresponding hyperpolarizability can then be obtained using [120]

$$\mathbf{p} = \varepsilon_0 \boldsymbol{\alpha} \mathbf{E}_{\mathrm{inc}} + \varepsilon_0 \boldsymbol{\beta} \mathbf{E}_{\mathrm{inc}}^2, \tag{6.2}$$

where the second term represents the nonlinear dipole contribution.

If the lattice constant is sufficiently large compared with the particle dimensions and the fundamental and SHG wavelengths, the inter-particle interaction and corresponding lattice-sum contribution discussed in Section 2 can

be neglected. The metasurface can therefore be approximated as an array of isolated electric dipoles. The effective hyperpolarizability of an individual particle can then be obtained from the total array response by accounting for the number of illuminated particles, which is equivalent to the number of illuminated unit cells [120]:

$$\beta_{\text{eff}}^{\text{single}} = \frac{\beta_{\text{eff}}^{\text{total}}}{N}. \tag{6.3}$$

In this situation, the lattice constant is larger than the wavelength, allowing higher-order diffraction modes to propagate. The in-plane wavevector and diffraction angle corresponding to the (m, n)th diffraction order are given by [46], [169]

$$k_{\parallel} = G_{mn} = \left| \frac{2\pi m}{d_x}\hat{\mathbf{i}} + \frac{2\pi n}{d_y}\hat{\mathbf{j}} \right|, \tag{6.4}$$

and

$$\sin\theta_{mn} = \frac{k_{\parallel}}{k_0} = \lambda\sqrt{\frac{m^2}{d_x^2} + \frac{n^2}{d_y^2}}. \tag{6.5}$$

In the simulations, the power monitor extends effectively infinitely in the x–y plane due to the periodic boundary conditions, allowing all propagating diffraction orders to be included in the calculated transmitted power. Similarly, in the experiment, a high-numerical-aperture objective placed after the sample enables the collection of the diffracted waves within its collection angle. Thus, the transmitted nonlinear response includes all the propagating diffraction orders collected in both the simulations and experiments.

To examine more closely the parameters that determine the hyperpolarizability tensor at the single-particle level, we consider an isolated particle with arbitrary geometry and material composition, whose center is located at the origin. The nonlinear dipole moment along the i-direction can be obtained by integrating the local second-order nonlinear polarization over the particle

volume The nonlinear dipole moment and effective hyperpolarizability can be defined as [70], [120],

$$p_i^{(2\omega)} = \varepsilon_0 \int_V \sum_{lm} \chi_{ilm}^{(2)}(\mathbf{r}) E_l(\mathbf{r},\omega) E_m(\mathbf{r},\omega)\, dV, \tag{6.6}$$

Defining the effective hyperpolarizability with respect to the incident field as [70], [120]

$$p_i^{(2\omega)} = \varepsilon_0 \sum_{jk} \beta_{ijk}^{\text{eff}} E_{\text{inc},j} E_{\text{inc},k}, \tag{6.7}$$

the corresponding tensor component can be expressed as [70], [120]

$$\beta_{ijk}^{\text{eff}}(\omega) = \frac{\int_V \sum_{lm} \chi_{ilm}^{(2)}(\mathbf{r}) E_l(\mathbf{r},\omega) E_m(\mathbf{r},\omega)\, dV}{E_{\text{inc},j} E_{\text{inc},k}}. \tag{6.8}$$

Eq. (6.8) shows that the hyperpolarizability is determined by the local-field strength, the local $\chi^{(2)}$ tensor, and their spatial distributions across the particle. Therefore, by comparing the linear response, such as the transmission or SCS spectra, with the nonlinear response, we can obtain valuable information about the relative contributions of local-field enhancement and the effective $\chi^{(2)}$ to the hyperpolarizability.

6.1.2 Computational Methods

The transmission spectra were calculated using the finite-difference time-domain (FDTD) method. Periodic boundary conditions were applied along x- and y-directions, while perfectly matched layers (PMLs) were used along z-direction, corresponding to the propagation direction. The finite-element method (FEM), implemented in COMSOL Multiphysics, was used to calculate the scattering cross sections associated with different multipolar modes of the nanoparticles.

For the nonlinear simulations, the structure was modeled in COMSOL using periodic boundary conditions along x- and y-directions and PMLs along z-direction. The nonlinear response was calculated through two consecutive studies. In the first study, the local linear electromagnetic field at the fundamental frequency was calculated and subsequently used to determine the nonlinear current density using the hydrodynamic model described in detail in Chapter 2. In the second study, the calculated nonlinear current density was introduced as a source distributed over the particle surface, from which the nonlinear far-field power and corresponding conversion efficiency were obtained.

To improve the numerical accuracy, progressively finer meshes and smaller frequency steps were considered. The mesh size and frequency resolution were refined until further refinement produced negligible changes in the calculated results, ensuring numerical convergence while avoiding unnecessary computational cost.

6.2 Design and results

We begin by considering four different geometries. Figures 6.1 (a)-(d) show their scattering cross-section spectra as a function of wavelength. all of the geometries exhibit a dominant electric-dipole response. Therefore, the corresponding periodic structures can be considered as arrays of electric dipoles characterized by different polarizability and hyperpolarizability tensors.

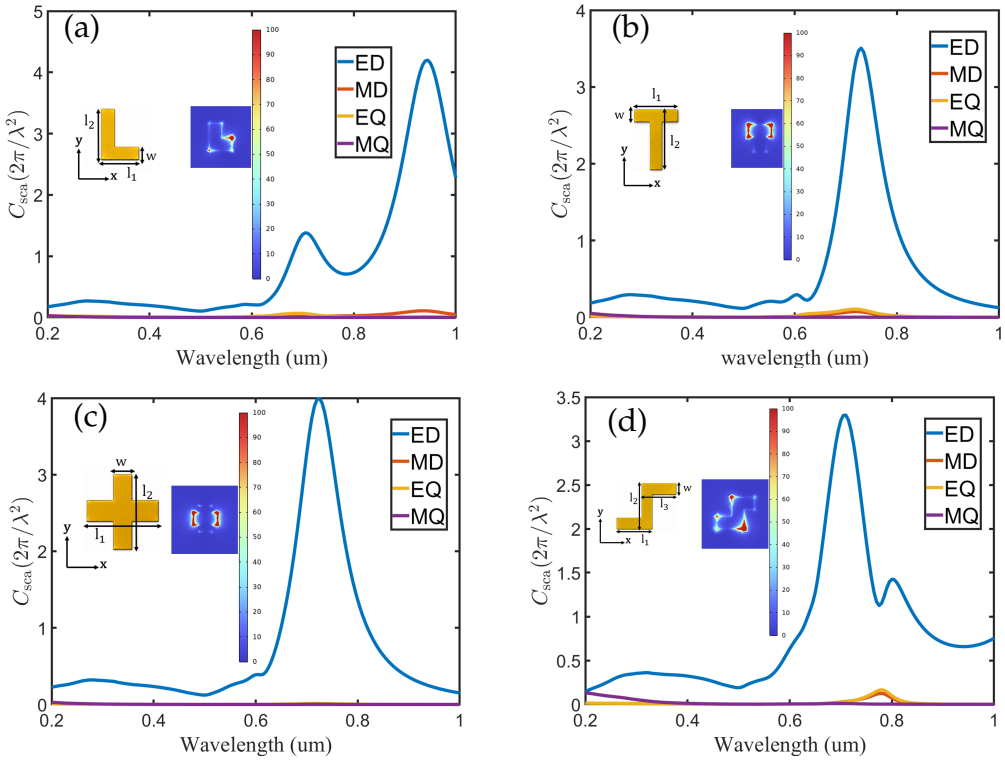

FIGURE 6.1: (a)–(d) Particle geometries, simulated scattering cross-section (SCS) spectra decomposed into different multipolar contributions, and normalized near-field intensity distributions. The L-shaped particle in (a) is shown under y-polarized excitation, while the T-, cross-, and gammadion-shaped particles in (b)-(d) are shown under x-polarized excitation. The L-, T-, and cross-shaped particles in (a)-(c) have dimensions $l_1 = 150$ nm and $l_2 = 180$ nm. The gammadion-shaped particle in (d) has dimensions $l_1 = 180$ nm, $l_2 = 210$ nm, and $l_3 = 150$ nm. The height h and width w are fixed for all geometries at 25 nm and 80 nm, respectively. The same colour scale is used for all particles.

In the next step, we consider periodic arrangements of each of the particles shown in figs. 6.2 (a)-(d) placed on a silica substrate with a refractive index of 1.45, and calculate their transmission spectra for the incident polarization that excites the corresponding plasmonic resonances identified in Fig. 6.1 (y-polarized excitation for the L-shaped particle and x-polarized excitation for the T-, cross-, and gammadion-shaped particles). As shown in fig. 6.2, the transmission spectra of all four geometries exhibit a resonance near 800 nm,

which is the wavelength of interest in this study. Compared with the scattering cross-section spectra of the individual particles shown in fig. 6.1, the resonances are shifted due to the presence of the substrate [123]. The periodicity of the metasurface is chosen to be 2 μm to ensure negligible coupling between neighboring particles [123].

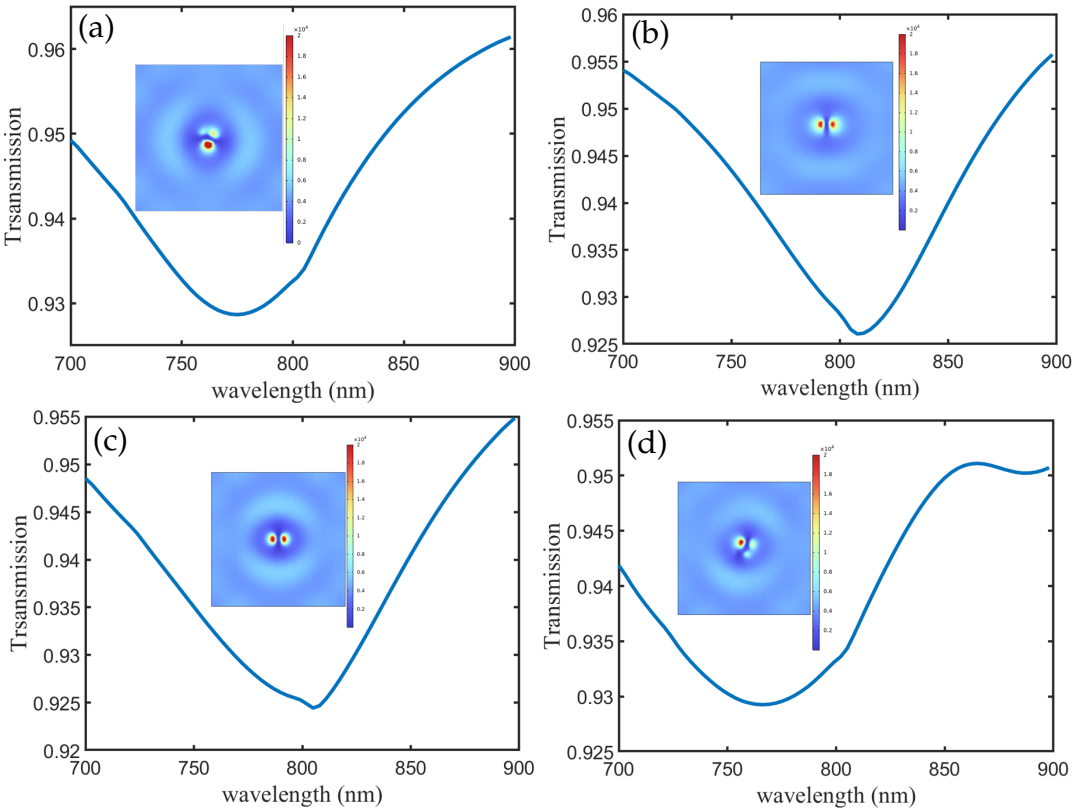

FIGURE 6.2: (a)-(d) Simulated transmission spectra and the corresponding normalized linear near-field intensity distributions 50 nm above the surface at a wavelength of 800 nm for the L-shaped, T-shaped, cross-shaped, and gammadion-shaped particles, respectively. The same colour scale is used for all particles.

Figures 6.3 (a)-(d) show the corresponding far-field nonlinear efficiency obtained from the simulations, with a clear peak near 800 nm associated with the LSPR. As discussed above, the LSPR is excited for a specific incident polarization, which also produces the maximum far-field nonlinear emission and therefore corresponds to the dominant element of the hyperpolarizability tensor, which is calculated using Eq. (6.8).

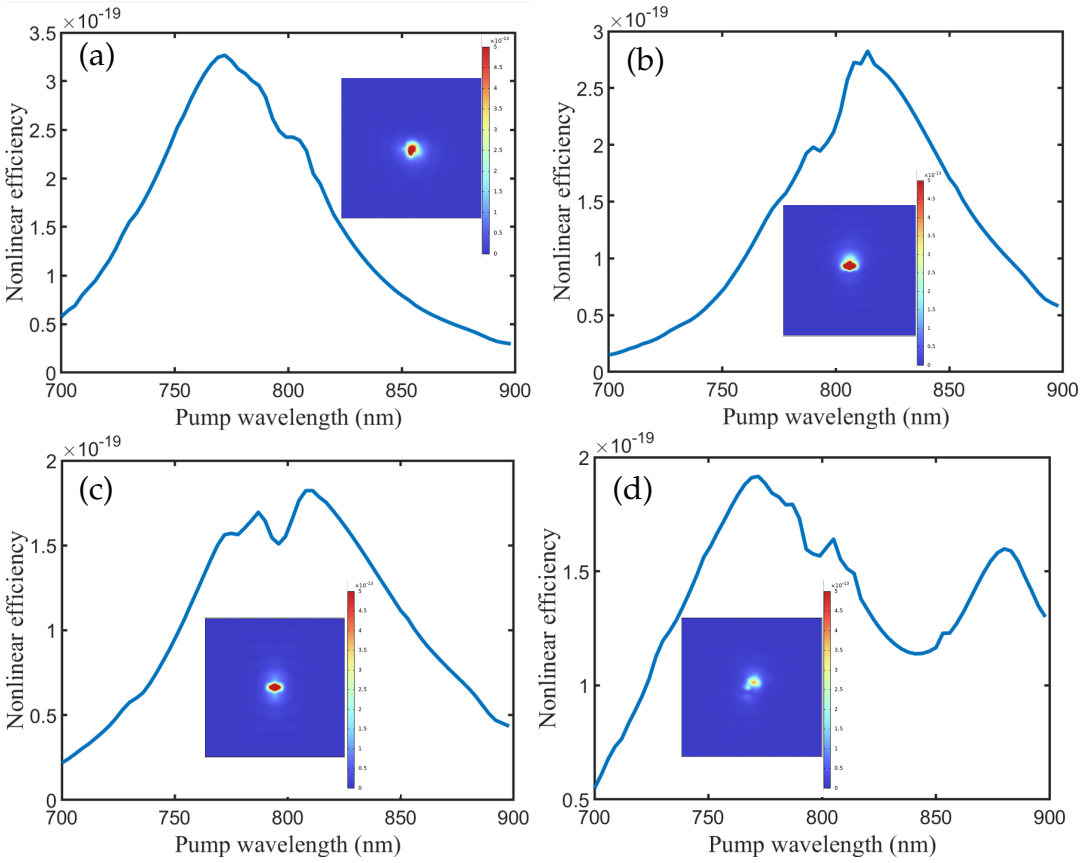

FIGURE 6.3: (a)-(d) Simulated nonlinear conversion efficiency spectra and the corresponding normalized nonlinear near-field intensity distributions 50 nm above the surface at a wavelength of 400 nm for the L-shaped, T-shaped, cross-shaped, and gammadion-shaped particles, respectively. The same colour scale is used for all particles.

As discussed in the Methodology section, the local $\chi^{(2)}$ and electric-field distribution are two main factors determining the hyperpolarizability. The local $\chi^{(2)}$, including both bulk and surface contributions, is governed by the material and geometrical symmetries and determines the allowed hyperpolarizability tensor components, while its magnitude contributes to their strength. On the other hand, the linear optical response, governed by the plasmonic resonance and the associated field enhancement, influences the magnitude of the nonlinear response and determines which components are stronger for a given incident polarization. Therefore, by comparing the transmission and hyperpolarizability spectra for each particle and across different geometries, we can evaluate how field enhancement and nonlinear susceptibility

contribute to the hyperpolarizability.

Figure 6.4 shows the calculated hyperpolarizability spectra of the four particles as a function of the pump wavelength.

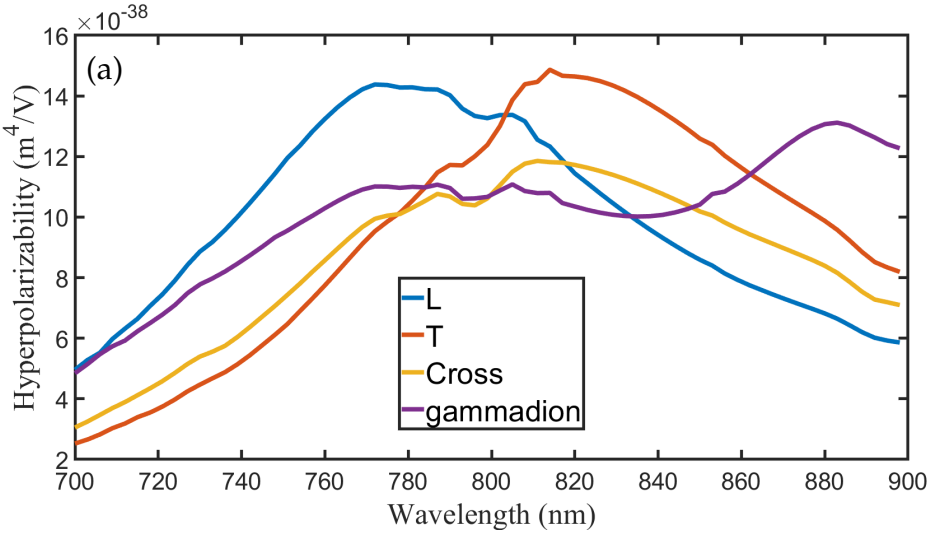

FIGURE 6.4: Simulated hyperpolarizability spectra as a function of wavelength for the L-shaped, T-shaped, cross-shaped, and gammadion-shaped particles.

Comparing the four particles, we observe that although all geometries exhibit linear and nonlinear responses of a similar order of magnitude, the L-shaped particle stands out. It shows the strongest linear response, with a larger scattering cross-section, a more pronounced resonance, and deeper transmission dips, as well as the highest nonlinear emission and more efficient far-field coupling. In contrast, the gammadion-shaped particle exhibits the weakest response in both the linear and nonlinear regimes. These differences can be attributed to the geometry-dependent plasmonic modes, which lead to variations in the strength and spatial distribution of the local fields among the geometries. These variations, in turn, influence the nonlinear emission and the resulting hyperpolarizability at 800 nm.

When comparing the cross- and T-shaped particles, we observe very similar linear responses. At resonance, the cross-shaped particle exhibits a larger

scattering cross-section than the T-shaped particle, although their scattering and transmission spectra have similar shapes, with a single resonance near 800 nm. The nonlinear near-field intensity distributions shown in fig. 6.3 are also comparable for the two particles. However, the cross-shaped particle exhibits a lower peak nonlinear conversion efficiency, suggesting that its generated SHG couples less efficiently to the far field. Consequently, the effective hyperpolarizability extracted from the far-field response is lower for the cross-shaped particle than for the T-shaped particle at a pump wavelength of 800 nm.

6.3 Experimental setup

To experimentally characterize the nonlinear optical response of the designed metasurfaces, we developed the setup shown in Figure 6.5 and described in detail in this section. A high-power femtosecond laser with a repetition rate of 10 kHz, a pulse duration of 35 fs, and a central wavelength of 800 nm was used as the excitation source. The average incident power was limited to 10 mW to avoid damaging the sample. two pinholes were used to align the beam along the optical path. followed by neutral-density (ND) filters to reduce the incident power. A half-wave plate (HWP) combined with a polarizing beam splitter (PBS) was used for continuous control of the incident power, while a second HWP was used to adjust the polarization state.

The beam was then tightly focused onto the sample using a microscope objective. The transmitted nonlinear signal was collected and collimated by a lens with a focal length of 4 cm. At the same time, the sample was illuminated with white light. The light reflected from the sample, together with the focused laser spot, was directed back toward the window and reflected toward a Thorlabs camera, allowing the laser position on the sample to be monitored. A focusing lens focused the reflected white light onto the camera, while an ND filter placed in front of the camera prevented saturation. After the collimating lens (L2), a set of UV filters was used to suppress the fundamental light at 800 nm while transmitting the SHG signal at 400 nm.

Finally, the SHG signal was focused onto a photomultiplier tube (PMT) coupled to a photon-counting system, which was used to measure the number of detected photons at the second-harmonic wavelength.

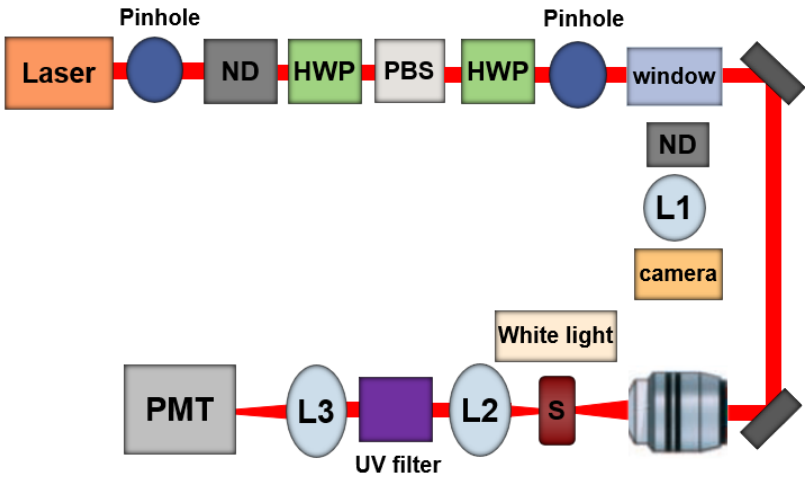

FIGURE 6.5: Nonlinear optical setup for measuring the photon count at the SHG wavelength.

The experimental measurements and further analysis of the role of geometrical symmetry in the nonlinear response are still in progress and are therefore not included in this chapter. The initial designs used the same particle geometries and dimensions as the optimized structures presented here but differed in their particle arrangements and array periodicities. These differences resulted in non-negligible interactions between neighboring particles, whereas the optimized designs suppress such interactions. Samples corresponding to all the initial designs were fabricated by Athulya Thulaseedharan, a PhD student in our group, and Lais Fujii dos Santos, a former postdoctoral fellow in our group. The fabrication of the optimized designs and the remaining experimental work, including data collection and more detailed theoretical analysis, will be continued by Mohammad Amin Hemmatian, a PhD student in our group.

6.4 Conclusion

In this work, we designed and characterized complex gold nanoparticles, including L-, cross-, T-shaped and gammadion geometries, to investigate how

structural asymmetry influences their nonlinear optical behavior. The dominant hyperpolarizability components were extracted and compared among the different particles. To distinguish the role of plasmonic enhancement from that of the effective $\chi^{(2)}$ distribution, the corresponding linear and nonlinear spectra were analyzed together.

Overall, this work provides a fundamental framework for probing geometry-dependent hyperpolarizability and relating the resulting tensor to particle symmetry. Establishing this connection could ultimately enable subwavelength structural information about unknown particles to be inferred through SHG spectroscopy and microscopy, particularly for biological and medical imaging applications.

Chapter 7

Conclusion

The ability to control the interaction of light with matter is central to the development of modern optical technologies. Increasing demands for compact, efficient, and multifunctional photonic systems have motivated the investigation of nanophotonic structures that can manipulate light at deeply subwavelength scales. Among these structures, metasurfaces have attracted considerable interest because they enable precise control over various properties of light, including its amplitude, phase, polarization, and frequency. Conventional optical components are often bulky and may suffer from material losses, limited functionality, and challenges in integration with compact photonic systems. Metasurfaces provide a versatile platform for performing linear and nonlinear optical operations within ultrathin structures, including functionalities that are difficult to achieve using conventional bulk components. In this thesis, their capabilities for optical filtering, nonlinear imaging, sensing, and frequency conversion were studied using theoretical, numerical, and experimental approaches. These studies addressed important challenges using metasurface platforms, including the low nonlinear conversion efficiency that limits the sensitivity and resolution of nonlinear microscopy. Several approaches to overcoming this limitation were investigated throughout the thesis. We also addressed fundamental challenges in plasmonic nonlinear optics, such as balancing the enhancement of the harmonic near field with efficient coupling to the far field. In addition, we investigated efficient and controllable spectral filtering using multilayer metal–dielectric platforms that combine the beneficial properties of both plasmonic and dielectric materials.

Chapters 1 and 2 first establish the background required for these investigations by introducing the fundamental concepts of metasurfaces and presenting the theoretical models used to describe their linear and nonlinear optical responses. Specifically, we described the interaction of light with a spherical particle using Mie theory and calculated the corresponding multipolar coefficients and scattering and absorption cross sections. Although the calculations were presented for a sphere, the multipolar approach can also be applied to other geometries, such as bars and crosses. We then modelled the coupling between multiple particles using the coupled-dipole approximation and studied two important collective effects: surface-lattice and Fano resonances. This framework was used to describe the linear optical response of interacting meta-atoms under appropriate assumptions. Next, we considered the nonlinear regime by explaining the contribution of multipolar modes to nonlinear emission. We also presented methods for modelling nonlinear current density and calculating the nonlinear far-field signal, including the hydrodynamic model and nonlinear scattering theory. The optical response of multilayer complementary structures exhibiting antireflection and bandpass-filtering responses was then studied. Finally, we introduced the computational methods used to implement these models. This theoretical and numerical background was applied to the design and simulation of the metasurfaces studied in the following chapters.

Chapter 3 is dedicated to the modelling and design of broadband transmissive bandpass meta-filters with central wavelengths of 30, 50, and 80 μm. We used multilayer complementary structures composed of gold and silicon, whose physical principles were discussed in Chapter 2. By following a detailed step-by-step design procedure, we obtained broadband filters at the target wavelengths with sharp spectral edges, high transmission within the passband, and low transmission within the stopbands.

The following three chapters focus on resolving subwavelength features of nanoparticles using SHG imaging and spectroscopy. In Chapter 4, we designed meta-atoms that mimic the optical response of polar biomolecules, whose polarity originates from geometrical asymmetry. We demonstrated

that near-field SHG images can be used to identify the polarity of these structures within random arrays. The numerical analysis was also supported by experimental results.

Chapter 5 investigates methods for enhancing SHG imaging of meta-atoms with geometries similar to those studied in Chapter 4. By introducing an external linear metasurface supporting a surface-lattice resonance, we enhanced the forward nonlinear emission while preserving the local near-field distribution. Using a stacked resonant platform, an enhancement of approximately 200-fold was achieved. This approach therefore improves the detectable SHG signal without sacrificing the spatial information carried by the near field.

In the chapter 6, we extended the analysis to more complex geometries that can represent different types of biomolecular structures. We estimated their second-order hyperpolarizability tensors from the far-field SHG emission, which can be obtained experimentally or numerically. A remaining step is to establish a direct connection between the extracted tensor components and the geometrical properties of structures whose SHG response originates from surface asymmetry.

Future work on the THz and mid-infrared filters should focus on the fabrication and characterization of the proposed structures. The designs could also be extended to other types of filters, such as high-efficiency narrowband bandpass and band-stop filters, for applications in telecommunications, medicine, and astronomy. As a simpler alternative to multilayer structures composed of complementary metallic and dielectric layers, all-dielectric metamaterials could be investigated because they may be easier to fabricate and more tolerant of variations in material properties and fabrication parameters. More complex physical mechanisms, such as electromagnetically induced transparency and Fano interference, could also be explored to achieve sharper spectral edges and higher transmission. However, these mechanisms introduce additional degrees of freedom, thereby increasing the complexity of the design and optimization processes.

For the nonlinear imaging and sensing projects, the next step is to establish a direct relationship between the extracted hyperpolarizability tensor and the geometrical symmetry of the corresponding particle. The experimental measurements should also be completed to validate the numerical results. However, the present analysis remains limited to the electric-dipole approximation. Future studies should therefore extend the same techniques to particles with significant higher-order multipolar contributions, providing a more general approach for extracting the geometrical features of unknown structures from their SHG signals. Beyond SHG, other nonlinear processes, such as third-harmonic generation, four-wave mixing, and stimulated Raman scattering, could also be investigated for imaging and sensing applications. In addition, structures supporting BICs or Fano resonances, as well as layers containing multi-quantum well, could be employed to enhance nonlinear signal generation and improve subwavelength-particle imaging using compact, label-free platforms. Such improvements could make these platforms particularly useful for biomedical applications, where they could facilitate the detection of small structural changes in biological samples.

Beyond filtering and sensing, future research could extend the design of nonlinear metasurfaces to other applications, such as quantum-light generation through spontaneous parametric down-conversion (SPDC). By relaxing conventional bulk phase-matching requirements and enabling resonant, modal, and symmetry-based control of nonlinear interactions, metasurfaces can selectively enhance desired processes and suppress competing ones. These capabilities could facilitate the development of compact and efficient quantum photonic devices with greater control over photon generation than conventional bulk platforms.

In general, our future studies will focus on the design, fabrication, and experimental characterization of metasurfaces with improved efficiency and robustness. We will focus on developing structures with high tolerance to fabrication imperfections, variations in material properties, and changes in the angle and polarization of the incident light. For nonlinear metasurfaces, we aim to increase the conversion efficiency while reducing optical losses and preventing material damage. Future studies could also investigate the

integration of the proposed metasurfaces with light sources, detectors, and photonic circuits to develop compact and multifunctional optical systems.

Overall, this thesis presents metasurface platforms with diverse linear and nonlinear optical functionalities that can be applied to a wide range of areas, including sensing, optical filtering, and high-resolution microscopy. The step-by-step design procedures, together with the numerical and experimental techniques presented throughout this thesis, provide a foundation for further developing these platforms and expanding their range of applications.

Bibliography

[1] N. Yu and F. Capasso, "Flat optics with designer metasurfaces," *Nature Materials*, vol. 13, no. 2, pp. 139–150, 2014. DOI: 10.1038/nmat3839

[2] G. Yoon, J. Jang, J. Mun, K. T. Nam, and J. Rho, "Metasurface zone plate for light manipulation in vectorial regime," *Communications Physics*, vol. 2, no. 1, p. 156, 2019. DOI: 10.1038/s42005-019-0258-x

[3] M. Kim and J. Rho, "Metamaterials and imaging," *Nano Convergence*, vol. 2, no. 1, p. 22, 2015. DOI: 10.1186/s40580-015-0053-7

[4] Y. Liu and X. Zhang, "Metamaterials: A new frontier of science and technology," *Chemical Society Reviews*, vol. 40, no. 5, pp. 2494–2507, 2011. DOI: 10.1039/C0CS00184H

[5] N. I. Zheludev and Y. S. Kivshar, "From metamaterials to metadevices," *Nature Materials*, vol. 11, no. 11, pp. 917–924, 2012. DOI: 10.1038/nmat3431

[6] V. G. Veselago, "The electrodynamics of substances with simultaneously negative values of ε and μ," *Soviet Physics Uspekhi*, vol. 10, no. 4, pp. 509–514, 1968. DOI: 10.1070/PU1968v010n04ABEH003699

[7] J. B. Pendry, A. J. Holden, W. J. Stewart, and I. Youngs, "Extremely low frequency plasmons in metallic mesostructures," *Physical Review Letters*, vol. 76, no. 25, pp. 4773–4776, 1996. DOI: 10.1103/PhysRevLett.76.4773

[8] J. B. Pendry, A. J. Holden, D. J. Robbins, and W. J. Stewart, "Magnetism from conductors and enhanced nonlinear phenomena," *IEEE Transactions on Microwave Theory and Techniques*, vol. 47, no. 11, pp. 2075–2084, 1999. DOI: 10.1109/22.798002

[9] D. R. Smith, W. J. Padilla, D. C. Vier, S. C. Nemat-Nasser, and S. Schultz, "Composite medium with simultaneously negative permeability and

permittivity," *Physical Review Letters*, vol. 84, no. 18, pp. 4184–4187, 2000. DOI: 10.1103/PhysRevLett.84.4184

[10] V. M. Shalaev, "Optical negative-index metamaterials," *Nature Photonics*, vol. 1, no. 1, pp. 41–48, 2007. DOI: 10.1038/nphoton.2006.49

[11] X. Huang, Y. Lai, Z. H. Hang, H. Zheng, and C. T. Chan, "Dirac cones induced by accidental degeneracy in photonic crystals and zero-refractive-index materials," *Nature Materials*, vol. 10, no. 8, pp. 582–586, 2011. DOI: 10.1038/nmat3030

[12] X. Fu and T. J. Cui, "Recent progress on metamaterials: From effective medium model to real-time information processing system," *Progress in Quantum Electronics*, vol. 67, p. 100 223, 2019. DOI: 10.1016/j.pquantelec.2019.05.001

[13] A. D. Boardman et al., "Active and tunable metamaterials," *Laser & Photonics Reviews*, vol. 5, no. 2, pp. 287–307, 2011. DOI: 10.1002/lpor.201000012

[14] W. L. Barnes, A. Dereux, and T. W. Ebbesen, "Surface plasmon subwavelength optics," *Nature*, vol. 424, no. 6950, pp. 824–830, 2003. DOI: 10.1038/nature01937

[15] J. N. Anker, W. P. Hall, O. Lyandres, N. C. Shah, J. Zhao, and R. P. Van Duyne, "Biosensing with plasmonic nanosensors," *Nature Materials*, vol. 7, no. 6, pp. 442–453, 2008. DOI: 10.1038/nmat2162

[16] J. B. Pendry, L. Martín-Moreno, and F. J. García-Vidal, "Mimicking surface plasmons with structured surfaces," *Science*, vol. 305, no. 5685, pp. 847–848, 2004. DOI: 10.1126/science.1098999

[17] F. J. García-Vidal et al., "Spoof surface plasmon photonics," *Reviews of Modern Physics*, vol. 94, no. 2, p. 025 004, 2022. DOI: 10.1103/RevModPhys.94.025004

[18] A. V. Kildishev, A. Boltasseva, and V. M. Shalaev, "Planar photonics with metasurfaces," *Science*, vol. 339, no. 6125, p. 1 232 009, 2013. DOI: 10.1126/science.1232009

[19] N. Yu et al., "Light propagation with phase discontinuities: Generalized laws of reflection and refraction," *Science*, vol. 334, no. 6054, pp. 333–337, 2011. DOI: 10.1126/science.1210713

[20] H.-T. Chen, A. J. Taylor, and N. Yu, "A review of metasurfaces: Physics and applications," *Reports on Progress in Physics*, vol. 79, no. 7, p. 076 401, 2016. DOI: 10.1088/0034-4885/79/7/076401

[21] T. J. Cui, M. Q. Qi, X. Wan, J. Zhao, and Q. Cheng, "Coding metamaterials, digital metamaterials and programmable metamaterials," *Light: Science & Applications*, vol. 3, no. 10, e218, 2014. DOI: 10.1038/lsa.2014.99

[22] C. Della Giovampaola and N. Engheta, "Digital metamaterials," *Nature Materials*, vol. 13, no. 12, pp. 1115–1121, 2014. DOI: 10.1038/nmat4082

[23] G. Li, S. Zhang, and T. Zentgraf, "Nonlinear photonic metasurfaces," *Nature Reviews Materials*, vol. 2, no. 5, p. 17 010, 2017. DOI: 10.1038/natrevmats.2017.10

[24] C. Anceau, S. Brasselet, J. Zyss, and P. Gadenne, "Local second-harmonic generation enhancement on gold nanostructures probed by two-photon microscopy," *Optics Letters*, vol. 28, no. 9, pp. 713–715, 2003. DOI: 10.1364/OL.28.000713

[25] M. Airola, Y. Liu, and S. Blair, "Second-harmonic generation from an array of sub-wavelength metal apertures," *Journal of Optics A: Pure and Applied Optics*, vol. 7, no. 2, S118–S123, 2005. DOI: 10.1088/1464-4258/7/2/016

[26] S. Linden, F. B. P. Niesler, J. Förstner, Y. Grynko, T. Meier, and M. Wegener, "Collective effects in second-harmonic generation from split-ring-resonator arrays," *Physical Review Letters*, vol. 109, no. 1, p. 015 502, 2012. DOI: 10.1103/PhysRevLett.109.015502

[27] A. Salomon, M. Zielinski, R. Kolkowski, J. Zyss, and Y. Prior, "Shape and size resonances in second harmonic generation from plasmonic nano-cavities," *The Journal of Physical Chemistry C*, vol. 117, no. 42, pp. 22 377–22 382, 2013. DOI: 10.1021/jp406135v

[28] Y. Zhang, F. Wen, Y.-R. Zhen, P. Nordlander, and N. J. Halas, "Coherent fano resonances in a plasmonic nanocluster enhance optical four-wave mixing," *Proceedings of the National Academy of Sciences*, vol. 110, no. 23, pp. 9215–9219, 2013. DOI: 10.1073/pnas.1220304110

[29] L. Luo et al., "Broadband terahertz generation from metamaterials," *Nature Communications*, vol. 5, no. 1, p. 3055, 2014. DOI: 10.1038/ncomms4055

[30] M. Celebrano et al., "Mode matching in multiresonant plasmonic nanoantennas for enhanced second harmonic generation," *Nature nanotechnology*, vol. 10, no. 5, pp. 412–417, 2015.

[31] E. Almeida, G. Shalem, and Y. Prior, "Subwavelength nonlinear phase control and anomalous phase matching in plasmonic metasurfaces," *Nature Communications*, vol. 7, no. 1, p. 10367, 2016. DOI: 10.1038/ncomms10367

[32] V. K. Valev et al., "Asymmetric optical second-harmonic generation from chiral g-shaped gold nanostructures," *Physical Review Letters*, vol. 104, no. 12, p. 127401, 2010. DOI: 10.1103/PhysRevLett.104.127401

[33] M. J. Huttunen, G. Bautista, M. Decker, S. Linden, M. Wegener, and M. Kauranen, "Nonlinear chiral imaging of subwavelength-sized twisted-cross gold nanodimers," *Optical Materials Express*, vol. 1, no. 1, pp. 46–56, 2011. DOI: 10.1364/OME.1.000046

[34] M. R. Shcherbakov et al., "Enhanced third-harmonic generation in silicon nanoparticles driven by magnetic response," *Nano Letters*, vol. 14, no. 11, pp. 6488–6492, 2014. DOI: 10.1021/nl503029j

[35] M. R. Shcherbakov et al., "Ultrafast all-optical switching with magnetic resonances in nonlinear dielectric nanostructures," *Nano Letters*, vol. 15, no. 10, pp. 6985–6990, 2015. DOI: 10.1021/acs.nanolett.5b02989

[36] L. Wang, S. Kruk, K. Koshelev, I. Kravchenko, B. Luther-Davies, and Y. Kivshar, "Nonlinear wavefront control with all-dielectric metasurfaces," *Nano Letters*, vol. 18, no. 6, pp. 3978–3984, 2018. DOI: 10.1021/acs.nanolett.8b01460

[37] S. Liu et al., "An all-dielectric metasurface as a broadband optical frequency mixer," *Nature Communications*, vol. 9, no. 1, p. 2507, 2018. DOI: 10.1038/s41467-018-04944-9

[38] L. Carletti, K. Koshelev, C. De Angelis, and Y. Kivshar, "Giant nonlinear response at the nanoscale driven by bound states in the continuum," *Physical Review Letters*, vol. 121, no. 3, p. 033 903, 2018. DOI: 10.1103/PhysRevLett.121.033903

[39] M. Cotrufo, L. Carletti, A. Overvig, and A. Alù, "Nonlinear nonlocal metasurfaces," *eLight*, vol. 6, no. 1, p. 5, 2026. DOI: 10.1186/s43593-025-00116-7

[40] C. M. Soukoulis and M. Wegener, "Past achievements and future challenges in the development of three-dimensional photonic metamaterials," *Nature Photonics*, vol. 5, no. 9, pp. 523–530, 2011. DOI: 10.1038/nphoton.2011.154

[41] J. Valentine et al., "Three-dimensional optical metamaterial with a negative refractive index," *Nature*, vol. 455, no. 7211, pp. 376–379, 2008. DOI: 10.1038/nature07247

[42] V. Khoshdel and M. Shokooh-Saremi, "Multilayered l-shaped nanoantenna arrays with an increased electric field enhancement," *Journal of the Optical Society of America B*, vol. 38, no. 5, pp. 1604–1612, 2021. DOI: 10.1364/JOSAB.417129

[43] L. Novotny and N. van Hulst, "Antennas for light," *Nature Photonics*, vol. 5, no. 2, pp. 83–90, 2011. DOI: 10.1038/nphoton.2010.237

[44] N. Meinzer, W. L. Barnes, and I. R. Hooper, "Plasmonic meta-atoms and metasurfaces," *Nature Photonics*, vol. 8, no. 12, pp. 889–898, 2014. DOI: 10.1038/nphoton.2014.247

[45] S. A. Maier, *Plasmonics: Fundamentals and Applications*. New York: Springer, 2007. DOI: 10.1007/0-387-37825-1

[46] L. Novotny and B. Hecht, *Principles of Nano-Optics*, 2nd ed. Cambridge: Cambridge University Press, 2012. DOI: 10.1017/CBO9780511794193

[47] J. Homola, "Surface plasmon resonance sensors for detection of chemical and biological species," *Chemical Reviews*, vol. 108, no. 2, pp. 462–493, 2008. DOI: 10.1021/cr068107d

[48] S. Aghili, "Engineered photonic structures for enhanced light–matter interaction and telecom-band DFB lasers," PhD thesis, University of Ottawa, Ottawa, Canada, 2026.

[49] G. Baffou and R. Quidant, "Thermo-plasmonics: Using metallic nanostructures as nano-sources of heat," *Laser & Photonics Reviews*, vol. 7, no. 2, pp. 171–187, 2013. DOI: 10.1002/lpor.201200003

[50] A. I. Kuznetsov, A. E. Miroshnichenko, M. L. Brongersma, Y. S. Kivshar, and B. Luk'yanchuk, "Optically resonant dielectric nanostructures," *Science*, vol. 354, no. 6314, aag2472, 2016. DOI: 10.1126/science.aag2472

[51] G. Mie, "Beiträge zur optik trüber medien, speziell kolloidaler metallösungen," *Annalen der Physik*, vol. 330, no. 3, pp. 377–445, 1908. DOI: 10.1002/andp.19083300302

[52] M. Kerker, D.-S. Wang, and C. L. Giles, "Electromagnetic scattering by magnetic spheres," *Journal of the Optical Society of America*, vol. 73, no. 6, pp. 765–767, 1983. DOI: 10.1364/JOSA.73.000765

[53] A. B. Evlyukhin, C. Reinhardt, A. Seidel, B. S. Luk'yanchuk, and B. N. Chichkov, "Optical response features of Si-nanoparticle arrays," *Physical Review B*, vol. 82, no. 4, p. 045 404, 2010. DOI: 10.1103/PhysRevB.82.045404

[54] A. García-Etxarri et al., "Strong magnetic response of submicron silicon particles in the infrared," *Optics Express*, vol. 19, no. 6, pp. 4815–4826, 2011. DOI: 10.1364/OE.19.004815

[55] A. B. Evlyukhin et al., "Demonstration of magnetic dipole resonances of dielectric nanospheres in the visible region," *Nano Letters*, vol. 12, no. 7, pp. 3749–3755, 2012. DOI: 10.1021/nl301594s

[56] A. I. Kuznetsov, A. E. Miroshnichenko, Y. H. Fu, J. B. Zhang, and B. Luk'yanchuk, "Magnetic light," *Scientific Reports*, vol. 2, p. 492, 2012. DOI: 10.1038/srep00492

[57] Y. H. Fu, A. I. Kuznetsov, A. E. Miroshnichenko, Y. F. Yu, and B. Luk'yanchuk, "Directional visible light scattering by silicon nanoparticles," *Nature communications*, vol. 4, no. 1, p. 1527, 2013.

[58] I. Staude et al., "Tailoring directional scattering through magnetic and electric resonances in subwavelength silicon nanodisks," *ACS Nano*, vol. 7, no. 9, pp. 7824–7832, 2013. DOI: 10.1021/nn402736f

[59] M. Decker et al., "High-efficiency dielectric huygens' surfaces," *Advanced Optical Materials*, vol. 3, no. 6, pp. 813–820, 2015. DOI: 10.1002/adom.201400584

[60] P. Moitra, B. A. Slovick, Z. G. Yu, S. Krishnamurthy, and J. Valentine, "Experimental demonstration of a broadband all-dielectric metamaterial perfect reflector," *Applied Physics Letters*, vol. 104, no. 17, p. 171 102, 2014. DOI: 10.1063/1.4873521

[61] A. E. Miroshnichenko and Y. S. Kivshar, "Fano resonances in all-dielectric oligomers," *Nano Letters*, vol. 12, no. 12, pp. 6459–6463, 2012. DOI: 10.1021/nl303927q

[62] A. E. Miroshnichenko et al., "Nonradiating anapole modes in dielectric nanoparticles," *Nature Communications*, vol. 6, p. 8069, 2015. DOI: 10.1038/ncomms9069

[63] D. Smirnova and Y. S. Kivshar, "Multipolar nonlinear nanophotonics," *Optica*, vol. 3, no. 11, pp. 1241–1255, 2016. DOI: 10.1364/OPTICA.3.001241

[64] L. Carletti, A. Locatelli, O. Stepanenko, G. Leo, and C. De Angelis, "Enhanced second-harmonic generation from magnetic resonance in AlGaAs nanoantennas," *Optics Express*, vol. 23, no. 20, pp. 26 544–26 550, 2015. DOI: 10.1364/OE.23.026544

[65] S. Liu et al., "Resonantly enhanced second-harmonic generation using III–V semiconductor all-dielectric metasurfaces," *Nano Letters*, vol. 16, no. 9, pp. 5426–5432, 2016. DOI: 10.1021/acs.nanolett.6b01816

[66] V. F. Gili et al., "Monolithic AlGaAs second-harmonic nanoantennas," *Optics Express*, vol. 24, no. 14, pp. 15 965–15 971, 2016. DOI: 10.1364/OE.24.015965

[67] G. Grinblat, Y. Li, M. P. Nielsen, R. F. Oulton, and S. A. Maier, "Enhanced third harmonic generation in single germanium nanodisks excited at the anapole mode," *Nano Letters*, vol. 16, no. 7, pp. 4635–4640, 2016. DOI: 10.1021/acs.nanolett.6b01958

[68] I. Vurgaftman, J. R. Meyer, and L. R. Ram-Mohan, "Band parameters for III–V compound semiconductors and their alloys," *Journal of Applied Physics*, vol. 89, no. 11, pp. 5815–5875, 2001. DOI: 10.1063/1.1368156

[69] R. Soref, "The past, present, and future of silicon photonics," *IEEE Journal of Selected Topics in Quantum Electronics*, vol. 12, no. 6, pp. 1678–1687, 2006. DOI: 10.1109/JSTQE.2006.883151

[70] R. W. Boyd, *Nonlinear Optics*, 4th ed. London: Academic Press, 2020.

[71] C. F. Bohren and D. R. Huffman, *Absorption and Scattering of Light by Small Particles*. New York: John Wiley & Sons, 1983.

[72] B. Auguié and W. L. Barnes, "Collective resonances in gold nanoparticle arrays," *Physical Review Letters*, vol. 101, no. 14, p. 143 902, 2008. DOI: 10.1103/PhysRevLett.101.143902

[73] V. G. Kravets, A. V. Kabashin, W. L. Barnes, and A. N. Grigorenko, "Plasmonic surface lattice resonances: A review of properties and applications," *Chemical Reviews*, vol. 118, no. 12, pp. 5912–5951, 2018. DOI: 10.1021/acs.chemrev.8b00243

[74] R. W. Wood, "On a remarkable case of uneven distribution of light in a diffraction grating spectrum," *The London, Edinburgh, and Dublin Philosophical Magazine and Journal of Science*, vol. 4, no. 21, pp. 396–402, 1902. DOI: 10.1080/14786440209462857

[75] L. Rayleigh, "On the dynamical theory of gratings," *Proceedings of the Royal Society of London. Series A*, vol. 79, no. 532, pp. 399–416, 1907. DOI: 10.1098/rspa.1907.0051

[76] R. Magnusson and S.-S. Wang, "New principle for optical filters," *Applied Physics Letters*, vol. 61, no. 9, pp. 1022–1024, 1992. DOI: 10.1063/1.107703

[77] S.-S. Wang and R. Magnusson, "Theory and applications of guided-mode resonance filters," *Applied Optics*, vol. 32, no. 14, pp. 2606–2613, 1993. DOI: 10.1364/AO.32.002606

[78] T. W. Ebbesen, H. J. Lezec, H. F. Ghaemi, T. Thio, and P. A. Wolff, "Extraordinary optical transmission through sub-wavelength hole arrays," *Nature*, vol. 391, no. 6668, pp. 667–669, 1998. DOI: 10.1038/35570

[79] S. Zou, N. Janel, and G. C. Schatz, "Silver nanoparticle array structures that produce remarkably narrow plasmon lineshapes," *The Journal of Chemical Physics*, vol. 120, no. 23, pp. 10 871–10 875, 2004. DOI: 10.1063/1.1760740

[80] V. G. Kravets, F. Schedin, and A. N. Grigorenko, "Extremely narrow plasmon resonances based on diffraction coupling of localized plasmons in arrays of metallic nanoparticles," *Physical Review Letters*, vol. 101, no. 8, p. 087 403, 2008. DOI: 10.1103/PhysRevLett.101.087403

[81] G. Vecchi, V. Giannini, and J. Gómez Rivas, "Shaping the fluorescent emission by lattice resonances in plasmonic crystals of nanoantennas," *Physical Review Letters*, vol. 102, no. 14, p. 146 807, 2009. DOI: 10.1103/PhysRevLett.102.146807

[82] S. R. K. Rodriguez, A. Abass, B. Maes, O. T. A. Janssen, G. Vecchi, and J. Gómez Rivas, "Coupling bright and dark plasmonic lattice resonances," *Physical Review X*, vol. 1, no. 2, p. 021 019, 2011. DOI: 10.1103/PhysRevX.1.021019

[83] V. A. Fedotov, M. Rose, S. L. Prosvirnin, N. Papasimakis, and N. I. Zheludev, "Sharp trapped-mode resonances in planar metamaterials with a broken structural symmetry," *Physical Review Letters*, vol. 99, no. 14, p. 147 401, 2007. DOI: 10.1103/PhysRevLett.99.147401

[84] D. C. Marinica, A. G. Borisov, and S. V. Shabanov, "Bound states in the continuum in photonics," *Physical Review Letters*, vol. 100, no. 18, p. 183 902, 2008. DOI: 10.1103/PhysRevLett.100.183902

[85] K. Koshelev, S. Lepeshov, M. Liu, A. Bogdanov, and Y. Kivshar, "Asymmetric metasurfaces with high-Q resonances governed by bound states in the continuum," *Physical Review Letters*, vol. 121, no. 19, p. 193 903, 2018. DOI: 10.1103/PhysRevLett.121.193903

[86] J.-N. Liu, Q. Huang, K.-K. Liu, S. Singamaneni, and B. T. Cunningham, "Nanoantenna–microcavity hybrids with highly cooperative plasmonic–photonic coupling," *Nano letters*, vol. 17, no. 12, pp. 7569–7577, 2017.

[87] A. Krasnok, M. Tymchenko, and A. Alù, "Nonlinear metasurfaces: A paradigm shift in nonlinear optics," *Materials Today*, vol. 21, no. 1, pp. 8–21, 2018. DOI: 10.1016/j.mattod.2017.06.007

[88] M. Kauranen and A. V. Zayats, "Nonlinear plasmonics," *Nature Photonics*, vol. 6, no. 11, pp. 737–748, 2012. DOI: 10.1038/nphoton.2012.244

[89] H. Liu et al., "Enhanced high-harmonic generation from an all-dielectric metasurface," *Nature Physics*, vol. 14, no. 10, pp. 1006–1009, 2018. DOI: 10.1038/s41567-018-0233-6

[90] G. Li et al., "Continuous control of the nonlinearity phase for harmonic generations," *Nature Materials*, vol. 14, no. 6, pp. 607–612, 2015. DOI: 10.1038/nmat4267

[91] B. Reineke et al., "Silicon metasurfaces for third harmonic geometric phase manipulation and multiplexed holography," *Nano Letters*, vol. 19, no. 9, pp. 6585–6591, 2019. DOI: 10.1021/acs.nanolett.9b02844

[92] A. G. G. M. Tielens, "The mid- and far-infrared range: Radiation emission processes from interstellar dust and gas," in *Observing Photons in Space: A Guide to Experimental Space Astronomy*, M. C. E. Huber, A. Pauluhn, J. L. Culhane, J. G. Timothy, K. Wilhelm, and A. Zehnder, Eds., 2nd ed., New York: Springer, 2013, pp. 139–163. DOI: 10.1007/978-1-4614-7804-1_7

[93] I. S. Glass, *Handbook of Infrared Astronomy*. Cambridge: Cambridge University Press, 1999. DOI: 10.1017/CBO9780511564949

[94] T. Nakagawa, H. Matsuhara, and Y. Kawakatsu, "The next-generation infrared space telescope SPICA," in *Space Telescopes and Instrumentation 2012: Optical, Infrared, and Millimeter Wave*, vol. 8442, SPIE, 2012, 84420O. DOI: 10.1117/12.927243

[95] C. N. Banwell, *Fundamentals of Molecular Spectroscopy*, 2nd ed. London: McGraw-Hill, 1972, ISBN: 9780070840072.

[96] K. Miyata et al., "Terahertz bandpass filter with babinet complementary metamaterial mirrors and silicon subwavelength structure," *Optics Express*, vol. 31, no. 14, pp. 23 507–23 517, 2023. DOI: 10.1364/OE.495232

[97] A. Beheshti Asl, A. Rostami, and I. S. Amiri, "Terahertz band pass filter design using multilayer metamaterials," *Optical and Quantum Electronics*, vol. 52, no. 3, p. 155, 2020. DOI: 10.1007/s11082-020-02268-x

[98] Nielson Scientific, *Single-layer metal mesh bandpass filter spec sheet*, Manufacturer's datasheet, Accessed November 10, 2026. [Online]. Available: https://nielsonscientific.com/band-pass-filters

[99] K. Simonyan, H. Gharagulyan, H. Parsamyan, A. Khachatryan, and M. Yeranosyan, "Broadband THz metasurface bandpass filter/antireflection coating based on metalized Si cylindrical rings," *Semiconductor Science and Technology*, vol. 39, no. 9, p. 095 012, 2024. DOI: 10.1088/1361-6641/ad6d86

[100] R. Ulrich, "Far-infrared properties of metallic mesh and its complementary structure," *Infrared Physics*, vol. 7, no. 1, pp. 37–55, 1967. DOI: 10.1016/0020-0891(67)90028-0

[101] Y. A. Akimov, "Mie scattering theory: A review of physical features and limitations," *arXiv preprint arXiv:2401.04146*, 2024. DOI: 10.48550/arXiv.2401.04146 arXiv: 2401.04146 [physics.optics].

[102] D. Tzarouchis and A. Sihvola, "Light scattering by a dielectric sphere: Perspectives on the Mie resonances," *Applied Sciences*, vol. 8, no. 2, p. 184, 2018. DOI: 10.3390/app8020184

[103] A. B. Evlyukhin and B. N. Chichkov, "Multipole decompositions for directional light scattering," *Physical Review B*, vol. 100, no. 12, p. 125 415, 2019. DOI: 10.1103/PhysRevB.100.125415

[104] M. F. Limonov, M. V. Rybin, A. N. Poddubny, and Y. S. Kivshar, "Fano resonances in photonics," *Nature Photonics*, vol. 11, no. 9, pp. 543–554, 2017. DOI: 10.1038/nphoton.2017.142

[105] D. A. Smirnova, A. I. Smirnov, and Y. S. Kivshar, "Multipolar second-harmonic generation by mie-resonant dielectric nanoparticles," *Physical Review A*, vol. 97, no. 1, p. 013 807, 2017. DOI: 10.1103/PhysRevA.97.013807

[106] F. Hache, H. Mesnil, and M.-C. Schanne-Klein, "Application of classical models of chirality to surface second harmonic generation," *The Journal of Chemical Physics*, vol. 115, no. 14, pp. 6707–6715, 2001. DOI: 10.1063/1.1404983

[107] M. Kauranen, T. Verbiest, J. J. Maki, and A. Persoons, "Second-harmonic generation from chiral surfaces," *The Journal of Chemical Physics*, vol. 101, no. 9, pp. 8193–8199, 1994.

[108] F. Hache, H. Mesnil, and M.-C. Schanne-Klein, "Application of classical models of chirality to surface second harmonic generation," *The Journal of Chemical Physics*, vol. 115, no. 14, pp. 6707–6715, 2001. DOI: 10.1063/1.1404983

[109] J. Butet and O. J. F. Martin, "Evaluation of the nonlinear response of plasmonic metasurfaces: Miller's rule, nonlinear effective susceptibility method, and full-wave computation," *Journal of the Optical Society of America B*, vol. 33, no. 2, A8–A15, 2016. DOI: 10.1364/JOSAB.33.0000A8

[110] C. Ciracì, E. Poutrina, M. Scalora, and D. R. Smith, "Second-harmonic generation in metallic nanoparticles: Clarification of the role of the surface," *Physical Review B*, vol. 86, no. 11, p. 115 451, 2012. DOI: 10.1103/PhysRevB.86.115451

[111] E. Rahimi and R. Gordon, "Nonlinear plasmonic metasurfaces," *Advanced Optical Materials*, vol. 6, no. 18, p. 1 800 274, 2018. DOI: 10.1002/adom.201800274

[112] R. C. Miller, "Optical second harmonic generation in piezoelectric crystals," *Applied Physics Letters*, vol. 5, no. 1, pp. 17–19, 1964. DOI: 10.1063/1.1754022

[113] C. G. B. Garrett and F. N. H. Robinson, "Miller's phenomenological rule for computing nonlinear susceptibilities," *IEEE Journal of Quantum Electronics*, vol. 2, no. 8, pp. 328–329, 1966. DOI: 10.1109/JQE.1966.1074073

[114] A. V. Krasavin, P. Ginzburg, and A. V. Zayats, "Free-electron optical nonlinearities in plasmonic nanostructures: A review of the hydrodynamic description," *Laser & Photonics Reviews*, vol. 12, no. 1, p. 1 700 082, 2018. DOI: 10.1002/lpor.201700082

[115] E. Rahimi and R. Gordon, "Nonlinear plasmonic metasurfaces," *Advanced Optical Materials*, vol. 6, no. 18, p. 1 800 274, 2018.

[116] K. O'Brien et al., "Predicting nonlinear properties of metamaterials from the linear response," *Nature Materials*, vol. 14, no. 4, pp. 379–383, 2015. DOI: 10.1038/nmat4214

[117] M. Born and E. Wolf, *Principles of Optics: Electromagnetic Theory of Propagation, Interference and Diffraction of Light*, 7th ed. Cambridge: Cambridge University Press, 1999.

[118] L. Huang et al., "Bilayer metasurfaces for dual- and broadband optical antireflection," *ACS Photonics*, vol. 4, no. 9, pp. 2111–2116, 2017. DOI: 10.1021/acsphotonics.7b00471

[119] L. Huang, Y. Yu, and L. Cao, "General modal properties of optical resonances in subwavelength nonspherical dielectric structures," *Nano Letters*, vol. 13, no. 8, pp. 3559–3565, 2013. DOI: 10.1021/nl4013834

[120] M Saad-Bin-Alam et al., "Hyperpolarizability of plasmonic meta-atoms in metasurfaces," *Nano Letters*, vol. 21, no. 1, pp. 51–59, 2021.

[121] M. A. Ordal, R. J. Bell, R. W. Alexander Jr., L. L. Long, and M. R. Querry, "Optical properties of Au, Ni, and Pb at submillimeter wavelengths," *Applied Optics*, vol. 26, no. 4, pp. 744–752, 1987. DOI: 10.1364/AO.26.000744

[122] H. Deng, M. Chan, and S. Zhou, "Terahertz broadband band-stop filter based on metasurface," in *2019 IEEE International Conference on Electron Devices and Solid-State Circuits (EDSSC)*, IEEE, 2019, pp. 1–3. DOI: 10.1109/EDSSC.2019.8754263

[123] S. Aghili, M. Mohammadpour, A. Thulaseedharan, L. Fujii dos Santos, L. Ramunno, and K. Dolgaleva, "Bi-layered stack plasmonic metasurface for high-resolution near-field second-harmonic generation microscopy applications," *Journal of the Optical Society of America B*, vol. 43, no. 5, pp. 1024–1033, 2026.

[124] M. R. Mohammadpour et al., "Random plasmonic metasurface for enhanced second harmonic generation," in *2026 Photonics North (PN)*, IEEE, 2026, pp. 1–2. [Online]. Available: https://ieeexplore.ieee.org/document/11657697

[125] A. Thulaseedharan, L. F. dos Santos, S. Aghili, M. R. Mohammadpour, O. W. Oner, and K. Dolgaleva, "Tuning proximity effect correction for plasmonic metasurfaces," *Journal of the Optical Society of America B*, vol. 43, no. 3, A132–A136, 2026.

[126] N. Hirokawa, S. Niwa, and Y. Tanaka, "Molecular motors in neurons: Transport mechanisms and roles in brain function, development, and disease," *Neuron*, vol. 68, no. 4, pp. 610–638, 2010.

[127] D. A. Dombeck, K. A. Kasischke, H. D. Vishwasrao, M. Ingelsson, B. T. Hyman, and W. W. Webb, "Uniform polarity microtubule assemblies imaged in native brain tissue by second-harmonic generation microscopy," *Proceedings of the National Academy of Sciences*, vol. 100, no. 12, pp. 7081–7086, 2003.

[128] P. W. Baas, J. S. Deitch, M. M. Black, and G. A. Banker, "Polarity orientation of microtubules in hippocampal neurons: Uniformity in the axon and nonuniformity in the dendrite," *Proceedings of the National Academy of Sciences*, vol. 85, no. 21, pp. 8335–8339, 1988.

[129] P. Pantazis, J. Maloney, D. Wu, and S. E. Fraser, "Second harmonic generating (shg) nanoprobes for in vivo imaging," *Proceedings of the National Academy of Sciences*, vol. 107, no. 33, pp. 14 535–14 540, 2010.

[130] S. Zhang et al., "Recent advances in nonlinear optics for bio-imaging applications," *Opto-Electronic Advances*, vol. 3, no. 10, p. 200 003, 2020.

[131] A. Aghigh, S. Bancelin, M. Rivard, M. Pinsard, H. Ibrahim, and F. Légaré, "Second harmonic generation microscopy: A powerful tool for bio-imaging," *Biophysical Reviews*, vol. 15, no. 1, pp. 43–70, 2023.

[132] K. M. Mayer and J. H. Hafner, "Localized surface plasmon resonance sensors," *Chemical Reviews*, vol. 111, no. 6, pp. 3828–3857, 2011.

[133] C. Rosman, J. Prasad, A. Neiser, A. Henkel, J. Edgar, and C. Sönnichsen, "Multiplexed plasmon sensor for rapid label-free analyte detection," *Nano Letters*, vol. 12, no. 11, pp. 5637–5643, 2012.

[134] I. Ament, J. Prasad, A. Henkel, S. Schmachtel, and C. Sönnichsen, "Single unlabeled protein detection on individual plasmonic nanoparticles," *Nano Letters*, vol. 12, no. 2, pp. 1092–1095, 2012.

[135] A. Krasnok, M. Tymchenko, and A. Alù, "Nonlinear metasurfaces: A paradigm shift in nonlinear optics," *Materials Today*, vol. 21, no. 1, pp. 8–21, 2018.

[136] Y. Cao, J. Li, M. Sun, H. Liu, and L. Xia, "Nonlinear optical microscopy and plasmon enhancement," *Nanomaterials*, vol. 12, no. 8, p. 1273, 2022.

[137] J. E. Sipe, V. C. Y. So, M. Fukui, and G. I. Stegeman, "Analysis of second-harmonic generation at metal surfaces," *Physical Review B*, vol. 21, no. 10, pp. 4389–4402, 1980.

[138] R. W. Boyd, A. L. Gaeta, and E. Giese, "Nonlinear optics," in *Springer Handbook of Atomic, Molecular, and Optical Physics*, Springer, 2008, pp. 1097–1110.

[139] M Saad Bin-Alam et al., "Cross-polarized surface lattice resonances in a rectangular lattice plasmonic metasurface," *Optics Letters*, vol. 47, no. 8, pp. 2105–2108, 2022.

[140] S. He et al., "Modulating polarization in second harmonic generation through symmetry evolution in plasmonic lattices," *ACS Nano*, vol. 18, no. 12, pp. 8745–8753, 2024.

[141] L. Ghirardini et al., "Plasmon-enhanced second harmonic sensing," *The Journal of Physical Chemistry C*, vol. 122, no. 21, pp. 11 475–11 481, 2018. DOI: 10.1021/acs.jpcc.8b03148

[142] J. Schust et al., "Spatially resolved nonlinear plasmonics," *Nano Letters*, vol. 23, no. 11, pp. 5141–5147, 2023.

[143] S. A. Jalil et al., "Spectroscopic signatures of plasmonic near-fields on high-harmonic emission," *Laser & Photonics Reviews*, vol. 17, no. 12, p. 2 300 448, 2023.

[144] S. Keren-Zur, O. Avayu, L. Michaeli, and T. Ellenbogen, "Nonlinear beam shaping with plasmonic metasurfaces," *ACS Photonics*, vol. 3, no. 10, pp. 1777–1783, 2016.

[145] Y.-M. Lee, S.-E. Kim, and J.-E. Park, "Strong coupling in plasmonic metal nanoparticles," *Nano Convergence*, vol. 10, no. 34, 2023.

[146] Y. Chen, Z. Lu, Y. Cao, M. Sun, and J. Dong, "Polarization and incident angle-dependent plasmonic coupling of au@ag nanoalloys," *Chinese Journal of Physics*, vol. 78, pp. 132–140, 2022.

[147] R. Czaplicki et al., "Less is more: Enhancement of second-harmonic generation from metasurfaces by reduced nanoparticle density," *Nano Letters*, vol. 18, no. 12, pp. 7709–7714, 2018.

[148] Z.-J. Yang, "Coherent energy transfers between orthogonal radiant and weakly radiant plasmonic nanorod resonators," *The Journal of Physical Chemistry C*, vol. 119, pp. 26 079–26 085, 2015.

[149] S. Zhang et al., "Recent advances in nonlinear optics for bio-imaging applications," *Opto-Electronic Advances*, vol. 3, no. 10, pp. 200 003–1, 2020.

[150] P. Pantazis, J. Maloney, D. Wu, and S. E. Fraser, "Second harmonic generating (SHG) nanoprobes for in vivo imaging," *Proceedings of the National Academy of Sciences*, vol. 107, no. 33, pp. 14 535–14 540, 2010.

[151] J. Butet, P.-F. Brevet, and O. J. F. Martin, "Optical second harmonic generation in plasmonic nanostructures: From fundamental principles to advanced applications," *ACS Nano*, vol. 9, no. 11, pp. 10 545–10 562, 2015.

[152] A. Bouhelier, M. Beversluis, A. Hartschuh, and L. Novotny, "Near-field second-harmonic generation induced by local field enhancement," *Physical Review Letters*, vol. 90, no. 1, p. 013 903, 2003.

[153] R. Czaplicki et al., "Less is more: Enhancement of second-harmonic generation from metasurfaces by reduced nanoparticle density," *Nano Letters*, vol. 18, no. 12, pp. 7709–7714, 2018.

[154] B. Shen et al., "Nonlinear spectral-imaging study of second- and third-harmonic enhancements by surface-lattice resonances," *Advanced Optical Materials*, vol. 8, no. 8, p. 1 901 981, 2020.

[155] C. Schlickriede et al., "Imaging through nonlinear metalens using second harmonic generation," *Advanced Materials*, vol. 30, no. 8, p. 1 703 843, 2018.

[156] B. K. Canfield et al., "Local field asymmetry drives second-harmonic generation in noncentrosymmetric nanodimers," *Nano Letters*, vol. 7, no. 5, pp. 1251–1255, 2007.

[157] M. J. Huttunen, P. Rasekh, R. W. Boyd, and K. Dolgaleva, "Using surface lattice resonances to engineer nonlinear optical processes in metal nanoparticle arrays," *Physical Review A*, vol. 97, no. 5, p. 053 817, 2018.

[158] M. J. Huttunen, O. Reshef, T. Stolt, K. Dolgaleva, R. W. Boyd, and M. Kauranen, "Efficient nonlinear metasurfaces by using multiresonant high-Q plasmonic arrays," *Journal of the Optical Society of America B*, vol. 36, no. 7, E30–E35, 2019.

[159] D. C. Hooper et al., "Second harmonic spectroscopy of surface lattice resonances," *Nano Letters*, vol. 19, no. 1, pp. 165–172, 2019.

[160] K. Thyagarajan, S. Rivier, A. Lovera, and O. J. F. Martin, "Enhanced second-harmonic generation from double resonant plasmonic antennae," *Optics Express*, vol. 20, no. 12, pp. 12 860–12 865, 2012.

[161] K.-Y. Yang, J. Butet, C. Yan, G. D. Bernasconi, and O. J. F. Martin, "Enhancement mechanisms of the second harmonic generation from double resonant aluminum nanostructures," *ACS Photonics*, vol. 4, no. 6, pp. 1522–1530, 2017.

[162] R. Czaplicki et al., "Enhancement of second-harmonic generation from metal nanoparticles by passive elements," *Physical Review Letters*, vol. 110, no. 9, p. 093 902, 2013.

[163] A. Verneuil et al., "Far-field mapping and efficient beaming of second harmonic by a plasmonic metagrating," *Nanophotonics*, vol. 13, no. 18, pp. 3609–3614, 2024.

[164] A. Movsesyan, L. V. Besteiro, X.-T. Kong, Z. Wang, and A. O. Govorov, "Engineering strongly chiral plasmonic lattices with achiral unit cells for sensing and photodetection," *Advanced Optical Materials*, vol. 10, no. 14, p. 2 101 943, 2022.

[165] S. Aghili, A. Amini, L. S. Dizaj, and K. Dolgaleva, "THz plasmonic metasurface based on a periodic array of InSb metamolecules with narrow resonances," *Optics Communications*, vol. 508, p. 127 805, 2022.

[166] M. S. Bin-Alam et al., "Ultra-high-q resonances in plasmonic metasurfaces," *Nature Communications*, vol. 12, no. 1, p. 974, 2021.

[167] I. S. Martinez and A. M. S. Lee, "Probing interfaces and non-centrosymmetry using SHG: A short study guide," *Science and Engineering Journal*, vol. 17, no. 1, pp. 104–127, 2024. [Online]. Available: https://scienggj.org/2024-104/

[168] J. F. Nye, *Physical Properties of Crystals: Their Representation by Tensors and Matrices*. Oxford: Oxford University Press, 1985.

[169] J. D. Jackson, *Classical Electrodynamics*, 3rd ed. New York: John Wiley & Sons, 1999.